CHARACTERIZATION OF THE STRUCTURAL, OPTICAL AND ELECTRICAL PROPERTIES OF ZnO:RE^{3+}/FWCNT/P3HT NANOCOMPOSITE FOR POSSIBLE APPLICATION IN ORGANIC SOLAR CELLS

by

ANGELINA SEITHATI QOTSO

Submitted in accordance with the requirements for

the degree of

DOCTOR OF PHILOSOPHY

in the subject

PHYSICS

at the

UNIVERSITY OF SOUTH AFRICA

SUPERVISOR: PROF B.M MOTHUDI

CO-SUPERVISOR: PROF P.S MBULE

JANUARY 2023

Declaration

Name: Angelina Seithati Qotso

Student number: 60944676

Degree: Doctor of Philosophy

Exact wording of the title of the thesis as appearing on the electronic copy submitted for examination:

Characterization of the structural, optical and electrical properties of ZnO:RE^{3+}/FWCNT/ P3HT nanocomposites for possible application in organic solar cells.

I declare that the above thesis is my own work and that all the sources that I have used or quoted have been indicated and acknowledged by means of complete references.

I further declare that I submitted the thesis to originality checking software and that it falls within the accepted requirements for originality.

I further declare that I have not previously submitted this work, or part of it, for examination at Unisa for another qualification or at any other higher education institution.

(The thesis will not be examined unless this statement has been submitted.)

SIGNATURE

January 2023

DATE

“A person who never made a mistake never tried anything new”.

– Albert Einstein

"I will thank you, Lord with all my heart; I will talk about your wonderful acts".

-PSALM 9:1

This thesis is dedicated to my family and mostly to my lovely daughters Kearatwa and Keabetswe

"*Only a life lived for others is a life worthwhile".*

– Albert Einstein

Acknowledgements

- ✓ First and foremost, I would like to thank God for giving me the strength to pursue this research. I thank him for being with me and by also giving me the strength even in difficult times when there was no hope of finishing this study, I thank you.

- ✓ I would like to express my deepest gratitude to both my promoters *Prof. B.M. Mothudi* and *Prof. P.S Mbule* for their valuable knowledge, guidance, patience, helpful suggestions, support and valuable comments which were essential to helping me finish degree.

- ✓ I would like to thank *Prof. M.S Dhlamini* and *Prof. L.L Noto* for their assistance, recommendations, and encouragement.

- ✓ Special thanks to my fellow researchers and Department of Physics staff members for their help and support.

- ✓ I would like to thank the electrical and smart systems engineering department (UNISA) for giving me the opportunity to present the courses I am presenting, thank you, everybody in this department is appreciated.

- ✓ I would like to express my gratitude to the South African National Research Foundation (NRF) and the University of South Africa for their support of this study (grant no. 108360))

- ✓ To the university of South Africa (Florida Campus) for encouraging and supporting its staff members to obtain at least PhD degree.

- ✓ Special thanks to my family and friends for their moral support, motivation, and everlasting love.

- ✓ Lastly, but not least, I would like to thank my dearest husband, *Sipho* for his trust, encouragement, and support throughout this journey and to our beautiful daughters *Kearatwa and Keabetswe,* I owe you playtime.

Abstract

The structure, morphology, optical, and electrical characteristics of rare earth (RE) metal ions, few-walled carbon nanotubes (FWCNT) and zinc oxide (ZnO) nanocomposite for possible applications such as electron acceptor in the active layer of organic solar cells are described in this study. ZnO nanotubes were created utilizing a microwave-assisted sol-gel technique with 1-Thioglycerol (TG) as a capping agent. To explore the effect of dopants in ZnO nanorods, the amounts of impurities or dopants were changed and integrated into a conjugated virgin poly(3-hexylthiophene) polymer (P3HT).

The surface morphology, crystal structure, optical absorption, photoluminescence (PL) and current-voltage (I-V) properties were influenced by dopants, ZnO/FWCNT nanocomposite and the incorporation of P3HT. The Field emission scanning electron microscopy (FE-SEM) showed the homogeneous nanorods morphology of ZnO, and the inclusion of P3HT dispersed the morphology into mixed structures of nanorods. X-ray diffraction (XRD) results showed that ZnO despite being doped or incorporated with P3HT, the nanorods have hexagonal wurtzite structure. X-ray photoelectron spectroscopy (XPS) revealed a strong interaction between P3HT and ZnO. All of the functional groups in the materials were visible using Fourier-transform infrared (FTIR). P3HT-ZnO doped with rare earth ions and P3HT/ZnO/FWCNT have a good property of the interaction that leads to a good mixing of ligands. The UV/VIS/NIR absorption findings demonstrated a significant improvement in absorption, providing additional chances for improved efficiency in organic solar cells. This is due to an increase in doping concentration and the integration of P3HT-ZnO at various ratios. The photoluminescence quenching effect of PL was considerable, suggesting that it might be used as an electron acceptor in the active layer of an organic photovoltaic (OPV) system. The I-V curve demonstrated an increase in electrical conductivity, indicating that these materials (P3HT-ZnO) at different ratios, an increase in rare earth doping concentration, and FWCNT) are prime candidates for accelerating electron transport, lowering electron-hole recombination, and improving the efficiency of organic solar cells (OSCs).

In this work, rare earth ions and FWCNT doped ZnO were combined with P3HT, and the introduction of P3HT considerably reduces the PL intensity, indicating a charge transfer between donor and acceptor materials. This combination serves to specifically amplify and enhance electron transfer and electrical conductivity for possible use in OSCs. Moreover, this

combination of materials has a strong photoluminescence quenching effect indicating a good charge separation in the photoactive layer of the organic solar cell device.

Keywords: Organic solar cell; P3HT; PL quenching, microwave-assisted sol-gel method, zinc oxide, carbon nanotubes.

Acronyms

CO_2	–	Carbon dioxide
NIR	–	Near Infra-Red
Er	–	Erbium
Tm	–	Thulium
Yb	–	Ytterbium
Sm	–	Samarium
ZnO	–	Zinc Oxide
CdSe	–	Cadmium Selenide
PbS	–	Lead Sulphide
PbSe	–	Lead Selenide
CNT	–	Carbon nanotubes
SWCNT	–	Single-walled carbon nanotubes
MWCNT	–	Multi-walled carbon nanotubes
FWCNT	–	Few-walled carbon nanotubes
TG	–	1-Thioglycerol
EDTA	–	Ethylene diamine tetra acetic acid
TEA	–	Triethanolamine
TEABr	–	Tetraethylammonium bromide
OLED	–	Organic light emitting diodes
OGS	–	Organic gas sensors
P3HT	–	poly(3 – hexylthiophene)
PCBM	–	[6,6]-phenyl C61-butyric acid methyl ester
OSCs	–	Organic Solar Cells
HSC	–	Hybrid solar cells
DSSC	–	Dye sensitized solar cells

QDSC	–	Quantum dot solar cells
PCE	–	Power conversion efficiency
XRD	–	X – ray diffraction
XPS	–	X – ray Photoelectron Spectroscopy
TEM	–	Transmission Electron Microscopy
FE-SEM	–	Field Emission Scanning Electron Microscopy
PL	–	Photoluminescence Spectroscopy
PV	–	Photovoltaic
UV – Vis – NIR	–	Ultraviolet Visible Near Infra – Red Spectroscopy
FTIR	–	Fourier Transform Infra-Red Spectroscopy
I-V	–	Current-Voltage

Table of Contents

List of Figures

List of Tables

Chapter 1

Introduction

1.1. Background

The growing energy demand and shortage of fossil fuels have forced people to look for highly efficient and renewable energy sources in recent years. Solar energy is the world's cleanest and most plentiful renewable energy source; it is inexpensive and CO_2-free, and it is more promising than fossil fuels which are non-renewable, unsustainable, and polluting the environment. However, solar energy is weather dependent while fossil fuels can generate a large amount of electricity at single location [1]. The earth receives an incredible amount of solar energy that can be utilized. The amount of solar radiation that reaches the earth in three days corresponds to the energy stored in all fossil fuels [1].

Solar energy creates a new way of life for mankind and leads society and human into an era of energy saving to reduce pollution. New initiatives are needed to use solar energy more efficiently to meet our clean energy needs [2]. As an inexhaustible source of environmentally friendly energy, solar energy has become an important topic of energy research worldwide [3]. As a result, the conversion of solar energy to electrical energy can be fulfilled by solar cell devices based on the process of the photovoltaic effect that is the generation of voltage or electric current in a material under the influence of light and is a physical and chemical phenomenon [4]

1.2. Problem Statement

The world suffers from a shortage of fossil fuel resources to meet human electricity needs, leading to an increase in electricity costs. Fig. 1.1 shows the global fossil fuels consumption which were formed millions of years ago. Global energy consumption is increasing year after year, and so the usage of fossil fuels is increasing. However, fossil fuels continue to dominate the worldwide energy system, when burned, they emit CO_2, a major contributor to global climate change and air pollution, both of which are connected to millions of premature deaths

each year [5]. The world requires a low-carbon energy source. Renewable energy has become widely available, and the world needs a swift shift away from fossil fuels [5].

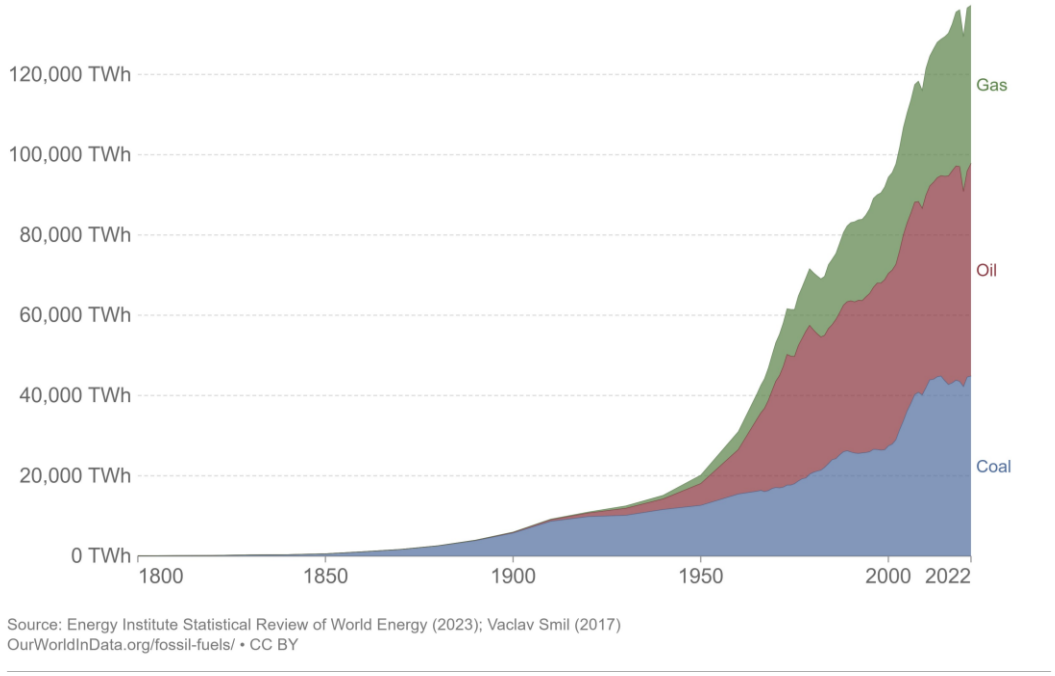

Figure 1. 1: Global fossil fuel consumption [5]

It is extremely important to develop an affordable and clean source of energy. Solar energy is an ideal form of energy because it is free, unlimited, renewable and clean (eco-friendly). In addition, this type of energy can also be used in very remote locations where power generation and distribution are limited. Organic solar cells (OSC) have gotten a lot of interest from academia and industry during the last three decades because they have substantial benefits over silicon-based devices, such as being lighter, more flexible, having cheaper processing costs, and having a smaller environmental effect. [1, 2].

Organic solar cells, which are made up of a combination of electron donor and acceptor materials, are emerging as viable new energy sources due to their low cost, versatility, simplicity of manufacturing, and low toxicity. High bandgap polymer materials have poor absorption, making it difficult to collect and minimize sunlight electron-hole recombination. However, the use of narrow bandgap polymers has enabled a wide range of absorption for solar spectrum capture and demonstrated efficiencies more than 5% [6-9]. In addition, these low bandgap polymeric materials have a low absorption within their absorption range, so they need to be improved. Combining these narrow bandgap polymer materials with a semiconductor

material such as zinc oxide (ZnO) and titanium dioxide (TiO_2) can improve the low absorption of the polymer and decrease the electron-hole recombination rate in the active layer [7]. In this case, the ZnO serves as the electron acceptor while P3HT as electron donor. Upon light irradiation, electron−hole pairs are generated within the donor material, and then dissociated into free charge at the donor/acceptor interface [10]. The aim of this study is to make contribution in addressing the challenges related to absorbing more sunlight in the solar spectrum by doping the P3HT-ZnO with rare earth (RE) ions and incorporating carbon nanotubes (CNT) with P3HT to improve the absorption of the polymer.

1.3. Research Aim

The goal of this research is to develop semiconductor materials and combine them with poly(3-hexylthiophene) (P3HT) to increase absorption and conductivity efficiency for use in organic solar cells.

1.3.1 Research objectives

- To synthesize ZnO nanorods using the microwave-assisted sol-gel synthesis
- To dope ZnO with rare earth ions (Er^{3+}, Ho^{3+}, Tm^{3+}, Sm^{3+}, Yb^{3+}) and CNT
- To enhance absorption of P3HT by incorporating ZnO: RE and ZnO: CNT

1.4. Thesis Layout

This thesis is divided into 8 chapters:

- ✓ **Chapter 1** presented a general introduction on renewable energy, solar cells, problem statement, goals, and objectives of the study.

- ✓ **Chapter 2** provides the literature review on renewable energy, photovoltaic effect, solar cell classification, organic photovoltaic charge transfer mechanism and the donor-acceptor pair in the active layer.

- ✓ **Chapter 3** gives a brief description on wet-chemistry synthesis methods, and characterization techniques that were used.

- ✓ **Chapter 4,** effects of ZnO nanorods singly doped with Er^{3+}, Ho^{3+}, and Tm^{3+} on P3HT for possible application in organic solar cell are discussed.

- ✓ In **Chapter 5** discusses microwave-assisted sol-gel synthesis of P3HT-ZnO: Sm^{3+}, Yb^{3+}: Study of structure, morphology, optical and electrical conductivity for possible application in organic solar cells. *(Article published in the Materials Chemistry and Physics Journal)*

- ✓ **Chapter 6** presents microwave-assisted sol-gel synthesis of P3HT-ZnO: FWCNT for organic solar cell applications. *(Article published in Physica B: Condensed Matter).*

- ✓ **Chapter 7** discusses the characterization of P3HT-FWCNT thin films for photovoltaic solar cell applications. *(SAIP2021 proceedings article)*

- ✓ **Chapter 8** gives summary of this study, conclusion and suggestions for possible future work.

References

[1] M. B. Askari, M. A. V. Mirzaei, M. Mirhabibi, *AJOP*, **3** (2015) 94 – 113.

[2] P. V. Kamat, *J. Phys. Chem. C*, **112** (2008) 18737 – 18753.

[3] B. V. Mathiesen, H. Lund, K. Karlsoon, *Appl energ*, **88** (2011) 488 –501.

[4] http://www.chemistryexplained.com/Ru-Sp/Solar-Cells.html [accessed 02/12/2022]

[5] https://ourworldindata.org/fossil-fuels (accessed 20/09/2023)

[6] Y. Liang, Y. Wu, D. Feng, S. Tsai, H. Son, G. Li, and L. Yu., *J. Am. Chem. Soc*., **56** (2009) 131.

[7] J. Peet, J. Y. Kim, N. E. Coates, W. L. Ma, D. Moses, A. J. Heeger, and G. C. Bazan, *Nature Mater.*, **6** (2007) 497.

[8] H. Chen, J. Hou, S. Zhang, Y. Liang, G. Yang, Y. Yang, L. Yu, Y. Wu, and G. Li, *Nature Phot.*, **3** (2009) 649.

[9] S. Park, A. Roy, S. Beaupré, S. Cho, N. Coates, J. Moon, D. Moses, M. Leclerc, K. Lee, and A.J. Heeger, *Nature Phot.,* **3** (2009) 297.

[10] H. Qiu, J. H. Shim, J. Cho, and J. M. Mativetsky, *ACS Applied Energy Materials* **1** (**2018**) 6172-6180.

Chapter 2

Literature review

This chapter provides the literature review on renewable energy, photovoltaic effect, solar cell classification, organic photovoltaic charge transfer mechanism and the donor-acceptor pair in the active layer.

2.1 Renewable energy

Energy plays a key role in socioeconomic growth and energy security around the world. The main energy sources are fossil fuels such as coal, oil and natural gas which are non-renewable. These fuels come from the remains of dead plants and animals that decomposed on earth over millions of years [1]. The non-renewable energy sources will deplete in our lifetime [2]. Carbon is the primary component of fossil fuels [2]. Coal is a reliable energy source, but when burned, it emits a large amount of hazardous chemicals and pollutants into the environment [2]. Although oil is very cheap to obtain and is the world's major transportation fuel, using gasoline is damaging to the environment [3]. Natural gas is also less expensive to extract and more environmentally friendly than oil and coal. The natural gases are locked underground, removing them can result in environmental issues such as mini earthquakes caused by splitting rocks and polluting drinking water caused by leaking other sources of water and chemicals [2]. Nuclear energy is a common source of electricity all around the world [3]. Nuclear energy also generates radioactive material, which may be exceedingly harmful, inflicting burns and raising the risk of cancer, blood disorders, and bone disintegration in those exposed to it [2].

Renewable energies are an alternative to traditional fossil fuel-based energies and appear to be significantly less harmful to the environment and can be used to produce energy again and again [4,5]. Solar energy, biomass fuels, wind energy, hydrothermal energy, geothermal power, and tidal energy are examples of renewable energy sources [6, 7]. Renewable energy sources are those resources which can be used to produce energy again and again [5]. Renewable energy sources that satisfy household energy needs have the ability to deliver energy services with zero or almost zero emissions of both air pollutants and greenhouse gases [8]. The development of renewable energy systems will enable the resolution of the current most critical tasks, such as improving energy supply reliability and organic fuel economy; resolving problems of local

energy and water supply; raising the standard of living and level of employment of the local population; ensuring sustainable development of remote regions in desert and mountain zones; and implementing the countries obligations in terms of fulfilling the international agreements relating to environmental protection [9]. Development and executions of renewable energy project in rural regions might create job opportunities and thus reducing migration towards urban areas [10,11]. Harvesting renewable energy in a decentralized manner is one alternative for meeting rural and small-scale energy demands in a dependable, economical, and ecologically friendly manner [10-12]. Renewable energy sources will play an essential part in the world's future. Fig. 2.1 shows some renewable and non-renewable energy sources.

Photovoltaic devices are known to use the photoelectric effect to transform photon energy into electrical energy. The increased need for sustainable energy sources has resulted in a significant growth in solar cell research in recent years [7]. In the near future, solar energy is expected to occupy a special place among other energy sources serving mankind. In fact, mankind's energy needs are increasing exponentially, and conventional fossil energy resources cannot meet these needs.

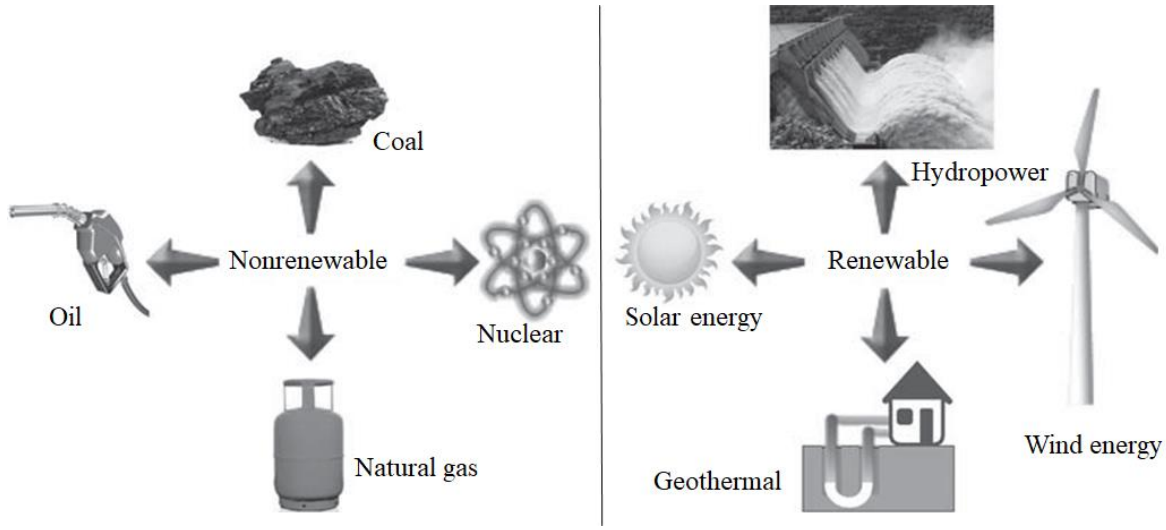

Figure 2. 1: Some of the non-renewable and renewable energy sources [1].

2.2 The Photovoltaic effect

The photovoltaic (PV) effect was first discovered in 1839 by French scientist Edmond Becquerel experimenting with wet cells, who found that the cell's voltage increased when its silver plates were exposed to sunlight [13]. Willoughby Smith (1873), an English engineer discovered that selenium has high photoconductivity, as well as a capacity to produce solar energy [14]. Albert Einstein (1904) described this phenomenon of the photovoltaic effect in

silicon and created the first silicon solar cells [14]. In addition, other solar cells such as germanium were made and produced with an efficiency of up to 4.5% [14]. The schematic diagram in Fig. 2.2 illustrates the photovoltaic effect in solar cells, i.e.; When sun photons strike a cell, their energy is transferred to charge carriers.

The electric field across the junction separates the photo-generated positive charge carriers (holes) from their negative counterpart (electrons) [15]. The p-n junction (where the photovoltaic effect occurs) in a solar cell is composed of two types of semiconductors connected. The p-type silicon has been doped positively with electron acceptors, while the n-type silicon has been doped negatively with electron donors [16]. This process is used for the direct conversion of sunlight into electrical current and electrical voltage and usually takes place in a solar cell. These cells are manufactured semiconductor devices made from pure silicon with the addition of impurities/dopants of some elements. The more energetic electrons in the valence band move to the conduction band, leaving a hole and thus forming electron-hole pairs (carriers). Also, at the end of the cell, the electrons pass through the external circuit, generate a current, lose energy, and return to the p-region gaps [13].

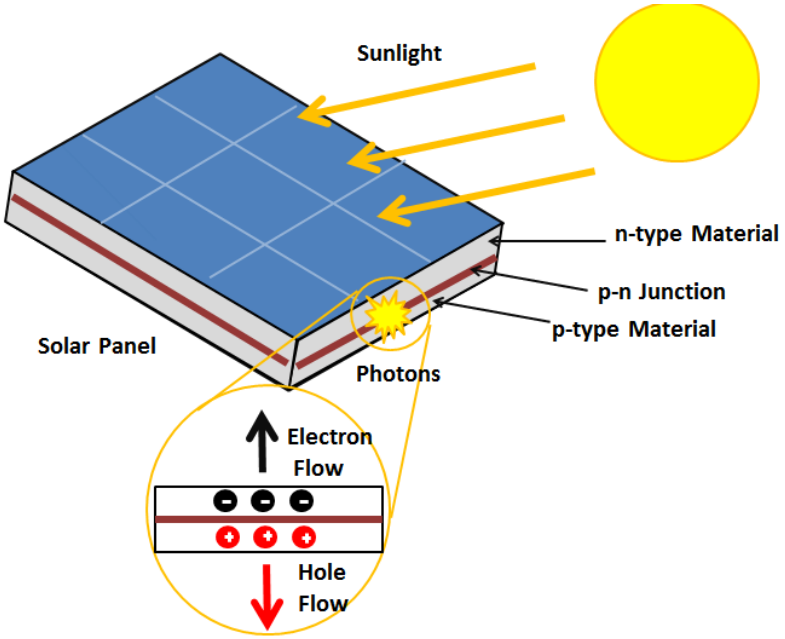

Figure 2. 2: Schematic diagram of Photovoltaic effect in solar cell [15].

2.3. Solar cells

Energy generated from these solar cells is called solar energy [17]. Among the various photovoltaic devices, thin film devices are promising devices to achieve low-cost production and do not require sophisticated manufacturing equipment [18]. Renewable energy has been extensively studied as it contains possible answers to the difficulty of preserving our energy supply [19]. Currently, there are many solar cell technologies in various stages of development, these solar cell technologies are divided into three generations: first, second and third generation solar cells as illustrated in Fig. 2.3.

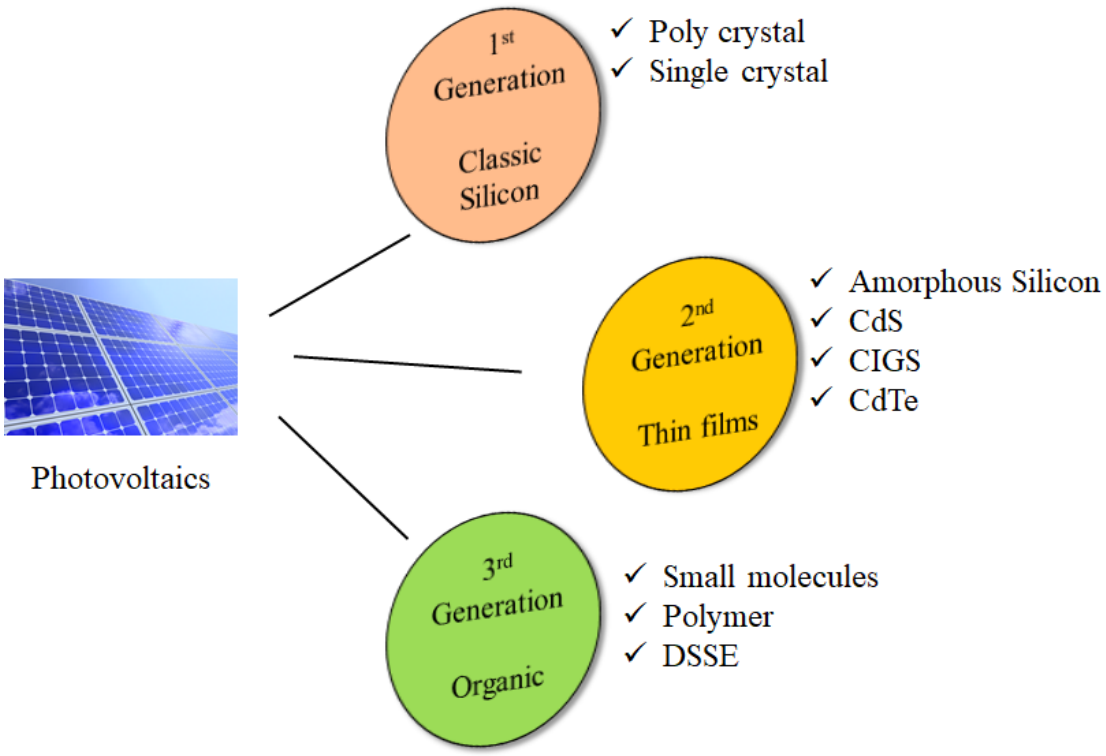

Figure 2. 3: Classification of solar cell generations [17].

2.2.1. The first generation of solar cells

The first generation includes the dominant silicon solar cells, as shown in the Fig. 2.4. These types of solar cells include monocrystalline and polycrystalline silicon solar cells [20]. This first generation dominated the technology in commercial solar cell manufacturing and accounted for more than 86% of the solar cell market [17]. This is due to their high efficiency and advanced technology, thanks to the development of the last 50 years [17]. The main disadvantage is that they are expensive because of the requirement for high purity silicon and solid structures. They consist of a large area of a single p-n junction diode, however, this

remains expensive generation and much of the energy at the blue and violet ends of the spectrum is wasted as heat [17]. Materials used in type of solar cells has limitations in terms of their capacity to absorb and convert short-wavelength (UV and blue) light; for example, silicon is a typical material for this generation, and it is not very efficient absorbing at these wavelengths.

Figure 2. 4: A monocrystalline silicon wafer-based solar cell [20].

2.2.2. The second generation of solar cells

Second-generation solar cells, as illustrated in Fig. 2.5, are also known as thin-film solar cells because they are composed of layers of semiconductor materials [21]. Thin-film solar cells have a lower efficiency compared to silicon solar cells and cheaper production costs. Cadmium telluride (CdTe), copper indium gallium selenide (CIGS), and amorphous silicon (a-Si-based solar cells) are the most effective second-generation materials [22]. The devices are flexible to a certain extent, but production costs remain high [21].

Figure 2. 5: Copper indium gallium diselenide thin film solar cells [21].

2.2.3. The third generation of solar cells

Fig. 2.6 shows third generation solar cells, commonly known to as new solar cell technology, based on latest chemistry techniques. Quantum dots [23], dye sensitized solar cells (DSSC) [24], perovskite solar cells [25], organic solar cells (OSC) [26], and hybrid solar cells [27] are among the technologies covered. This generation of semiconductor devices differs significantly from the earlier generations in such a way that it does not rely on the usual p-n junction to segregate the charge created by light average [22]. The goal is to improve the poor electrical performance of second-generation technology while keeping production costs extremely low [17].

Figure 2. 6: Organic solar cell cast on a flexible substrate. It can be stretched, rolled or even curved in any direction [26].

2.3. Progress in OSC Technology

2.3.1. Dye-sensitized solar cells (DSSC)

Dye-sensitized solar cells (DSSC) are the third generation of solar cells. Therefore, they are expected to significantly increase their share of global energy production in the coming years. This is due to the low production costs and attractive properties such as transparency and flexibility [28]. They are also a promising replacement for traditional silicon solar cells because they can generate electricity even in low light conditions or overcast weather [29]. However, the problem with DSSC is that not all electrons generated by light can reach the collecting electrode as the transport of electrons in the nanoparticle lattice occurs via a number of stages to neighbouring particles, and the energy damage that happens during charge transport operations leads in conversion efficiency [30]. Conversion efficiency varies between 6 to 10% pending on module size and the technology is currently at pilot plant scale. The fundamental issue is that a monolayer of dye particles on a flat surface can absorb only about 1% of the incoming light [28]. In this instance, a dye captures the sunlight in a manner similar to how sunlight captured in natural photosynthesis, producing an electron injection into the conduction band of a metal oxide, giving rise to charge separation [31]. The schematic assembly of a monolayer DSSC is reported in Fig. 2.7. Also, researchers started to think about the fabrication of a new solar cell, they decided to build a double-layer solar cell from organic materials as shown in Fig. 2.8. [32].

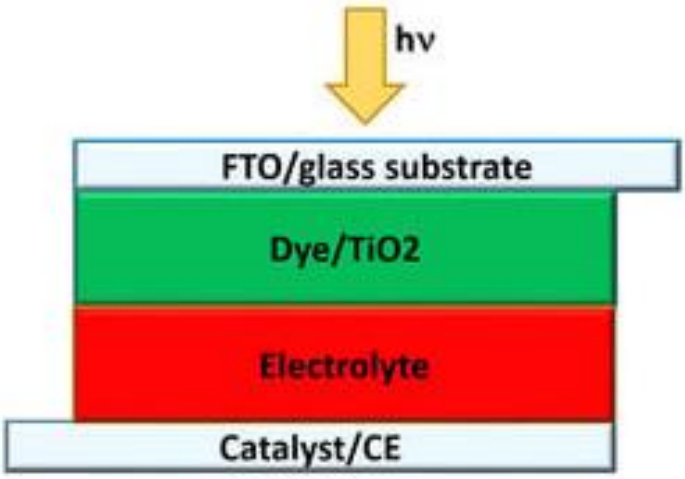

Figure 2. 7: The schematic of a monolayer DSSC [31].

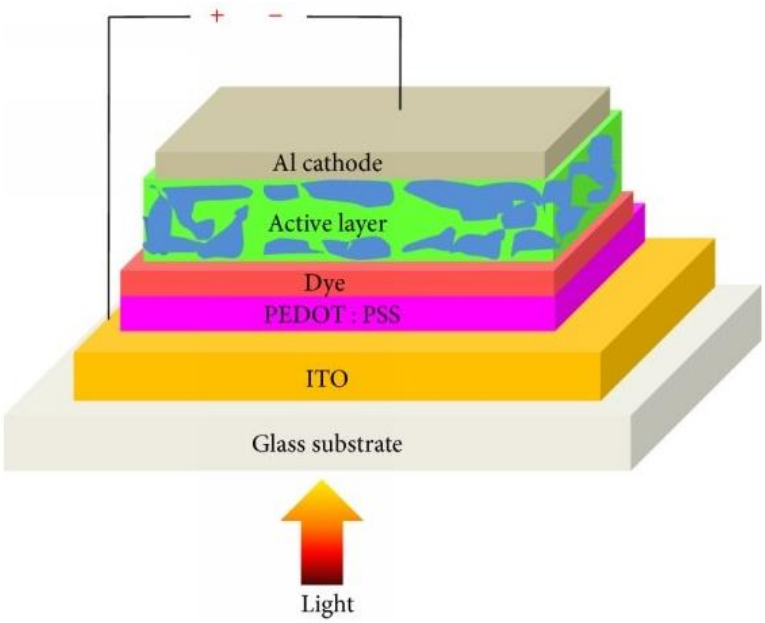

Figure 2. 8: solid-state dye-sensitized solar cell [32].

2.3.2. Organic solar cells (OSCs)

Organic Solar Cells (OSC) have become a new competitor to traditional solar cells due to their advantages of flexible solar modules, low cost, light weight, easy production and low-cost mass production for industrial photovoltaic [33-37]. An organic solar cell (OSC) consists of an organic layer of an active photovoltaic layer sandwiched between a transparent electrode and a metal electrode [35] as shown in Fig. 2.9. The exciton is generated by sunlight in a mixture of (P3HT) and fullerenes (PCBM), with the PCBM acting as an electron acceptor and providing interfacial energy and work function for charge separation. These produced carriers are subsequently transferred via the donor and acceptor components, mixed, and selectively collected by the electrodes. Electron donor and acceptor materials with optimal characteristics are required to attain high PCE. OSC has shown a high efficiency of 13.1%, and this efficiency can only be achieved with Thickness of 100 - 200 nm [38].

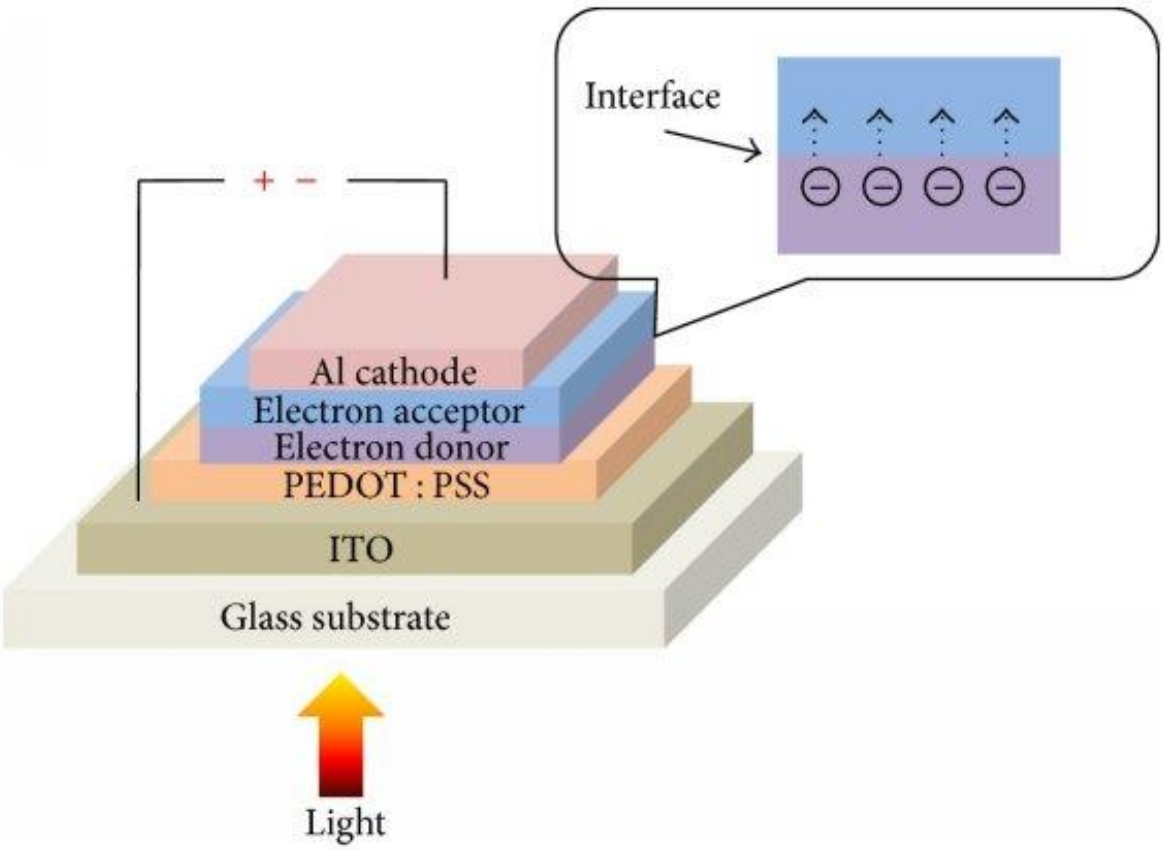

Figure 2. 9: Typical device structure of bilayer solar cell [32].

2.3.3. Hybrid solar cells (HSCs)

Hybrid solar cells were developed to overcome the problems of conventional silicon-based solar cells [39]. Silicon solar cells have an efficiency limit of about 27-29% for single-junction cells and become less efficient as their operating temperatures increase, and they are more efficient at converting sunlight within a narrow range of wavelengths [20]. They can also experience efficiency decline due to overcast conditions [20]. Tunable absorption spectra from an inorganic component are among the benefits of hybrid solar cells, which blend organic and inorganic materials. These solar cells are comparable to the OSC (see Fig. 2.10). They have the potential for high power conversion efficiency (PCE), although their existing efficiencies are rather modest [40]. A PCE of 11.46% was reported with an optimal Al_2O_3 thickness of 2.3 nm [41]. These results were due to enhanced built-in potential and better charge collection via the electron blocking action of Al_2O_3 [41]. HSCs use a mix of amorphous and crystalline silicon layers to increase the efficiency of silicon-based solar cells [41]. Because of the heterojunction between these layers, recombination losses are reduced, and conversion efficiencies are increased [39]. HSCs with their unique structure have demonstrated enhanced performance at

high temperatures, making them more ideal for hot and sunny climates, and they can even generate electricity when sunlight levels are low [40]. Furthermore, they have a greater spectral response, which means they can capture a broader range of the sun spectrum, including longer and shorter wavelengths of light [41].

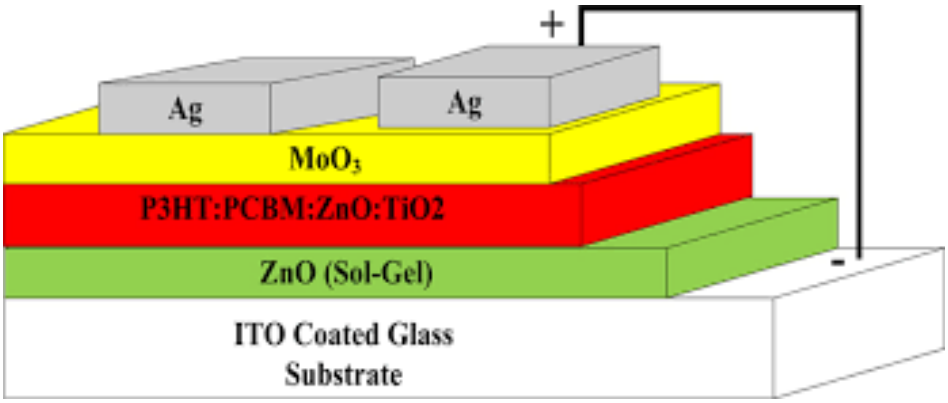

Figure 2. 10: Schematic diagram of inverted bulk heterojunction (BHJ) hybrid solar cell [42].

2.3.4. Quantum dot solar cells (QDSCs)

Quantum dot solar cells (QDSCs) were developed to use quantum dots as absorbing photovoltaic materials. These quantum dots are semiconductors with very small particles and their bandgap values can be easily customized by changing the particle size. The bandgap of the semiconductor nanocrystal increases as the size of the QD decreases due to quantum confinement, while discrete energy levels arise at the band-edges and the energy separation between the band-edge levels increases with decreasing size [43] as shown in Fig. 2. 11. Quantum confinement restricts the movement of electrons and holes within the QD, making it possible to tune the optical spectra of the semiconductor through a wide spectral window by simply changing their size, while keeping their composition constant [44,45]. QDSCs have been proposed to achieve high energy conversion efficiency [46]. The use of quantum dots (QD) in the production of solar cells not only promises a lot of power conversion efficiency, but also offers spectrum tuning [47]. PCE values of 10% and more were reported by Ruhle et al. [48], where QD semiconductor was used as the light absorbing material for efficient light harvesting across the solar spectrum. Fig. 2.12 shows a diagram of $CsPbBr_3$ [49] quantum dot solar cells.

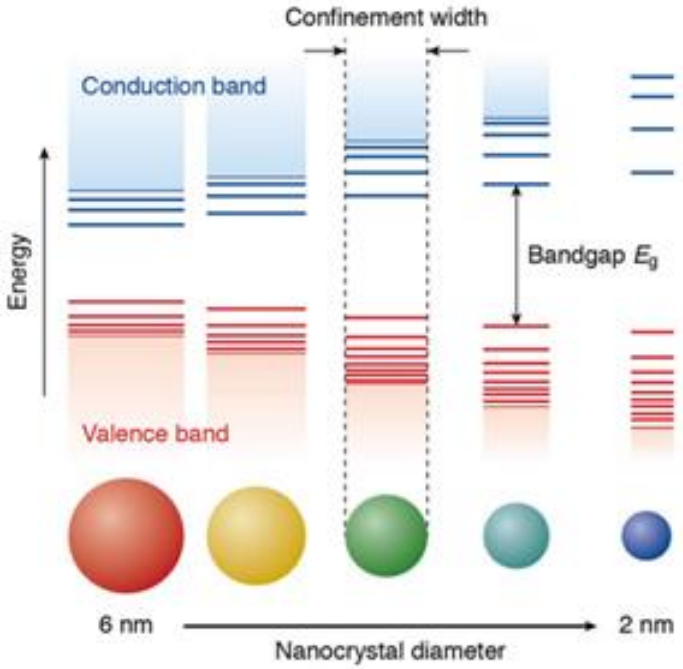

Figure 2. 11: Schematic representation of the quantum confinement effects [45].

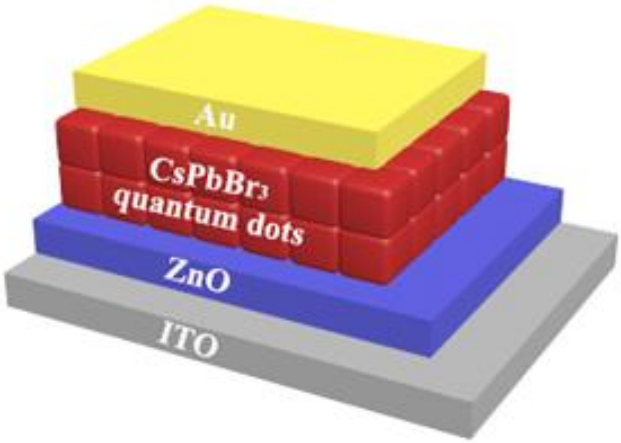

Figure 2. 12: Schematic of cross-sectional $CsPbBr_3$ quantum dot solar cells [49].

2.4. The photoactive layer

The photoactive layer consists of two heterojunction semiconductor materials: the donor and the acceptor. This layer is located between two electrodes (anode and cathode) and is responsible for light absorption, charging separation and production of load carriers. The anode in the active layer is mainly deposited on top, mostly made of aluminium, gold, silver and calcium. In most cases, poly-(phenylene vinylene) derivatives and poly-(alkyl thiophenes) are regular donors; usual acceptors are fullerenes and their derivatives [50]. To improve light

absorption, the bandgap of the polymer material must be reduced to allow current flow to increase. ZnO has been considered as one of the potential materials in solar cell applications due to their stability, high conductivity, high electron affinity and excellent electron mobility [51]. In this study, P3HT and ZnO are used as donor and acceptor. Schematic diagram in Fig. 2.13 shows a photovoltaic solar cell.

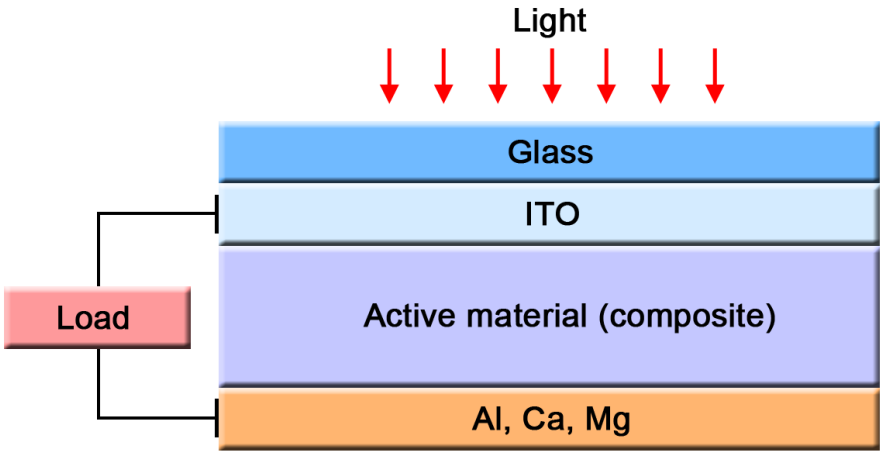

Figure 2. 13: Photovoltaic solar cell [52].

2.5. Organic photovoltaic charge transfer mechanism

An electron is stimulated from the highest occupied molecular orbital (HOMO) to the lowest unoccupied molecular orbital (LUMO) in organic semiconductors, resulting in an electron-hole known as an exciton [53]. Fig. 2.14 illustrates the band structure of a device with a donor-acceptor mix. This design underlines when the donor molecule is excited, an electron is transferred from the HOMO to the LUMO, leaving a hole. When the electron-hole pair recombines, photoluminescence is generated. Furthermore, this also highlights how exciton dissociation occurs free charge carriers on the electrode or on the heterojunction (which contains a donor-acceptor pair) [50]. An electric field is necessary to achieve charge separation, which is given by the way the electrodes function.

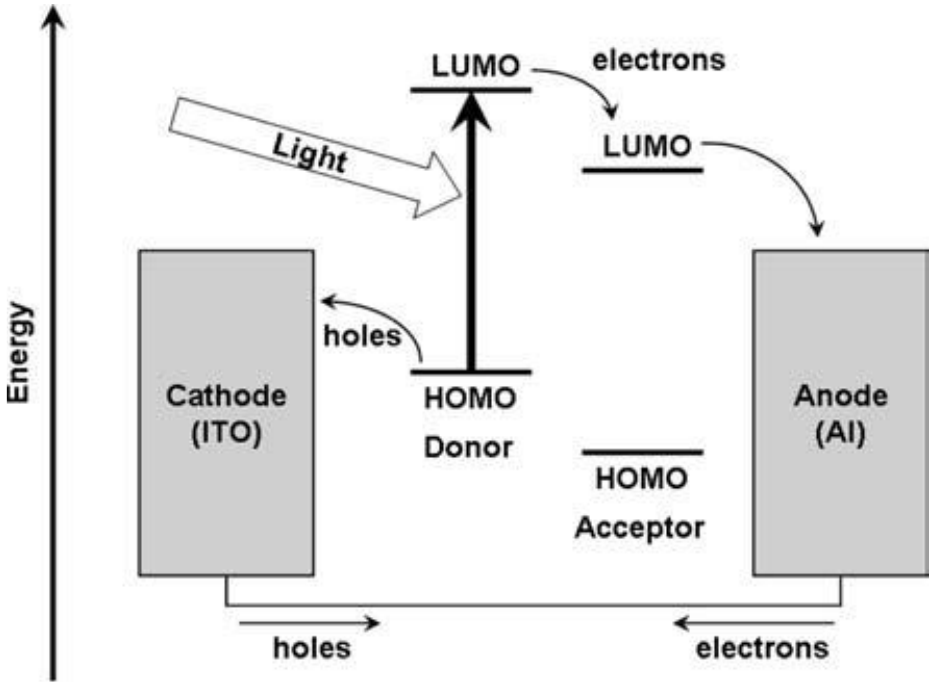

Figure 2. 14: The donor-acceptor interface [50].

2.6. Efficiency of Solar cells

Solar energy is one of the most demanding sources of renewable electricity. Photovoltaic power generation is helping to meet growing energy demand by reducing dependence on fossil fuels and helping limit global climate change. Researchers and scientists have increased competition in solar cell generations by developing new materials in nanotechnology and nanomaterials. Monocrystalline silicon solar cells are known to dominate the market due to their high efficiency. On a laboratory scale, the efficiency of crystalline silicon solar cells has reached 27.6% [54]. As the efficiency of crystalline silicon solar cells approaches saturation, scientists around the world are researching alternative materials to increase solar cell efficiency. However, their disadvantage is their disordered nature, which leads to low efficiency [54]. Fig 2.15. shows the recent solar cell efficiencies.

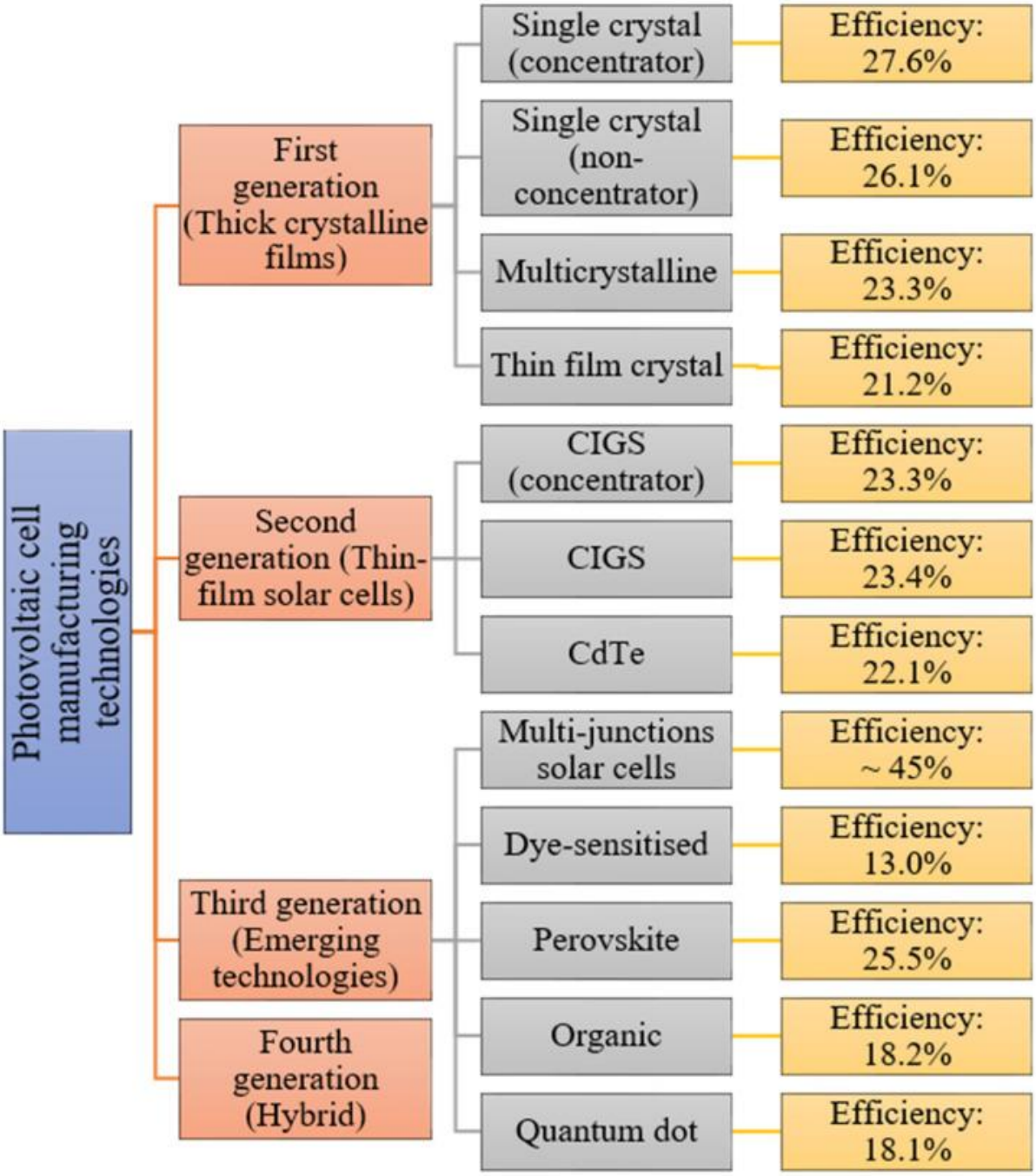

Figure 2. 15: The photovoltaic cell efficiencies [54].

2.7. Materials Properties

2.7.1. Zinc Oxide (ZnO)

ZnO is one of the most attractive semiconductor materials with a 3.37 eV broad band gap [55]. It is not only an excellent wide gap semiconductor, but it is also a suitable host for the successful integration of RE ions with 4f energy levels [56]. Unlike many of its rivals, ZnO is cheap, plentiful, chemically stable, simple to manufacture, and non-toxic [57]. Un-doped and

doped ZnO nanocrystal optical materials with various activators are known [57]. These nanoparticles have a wide range of applications including photodetectors, sensors, solar cells, light emitting diodes and p-n heterojunctions [58]. The crystal structures of ZnO are known; hexagonal wurtzite, the ultimate environmentally stable zinc blende, which can only be stabilized by growing on a cubic substrate, and rock salt, which can be obtained at relatively high temperatures. These crystalline structures are shown schematically in Fig. 2.16.

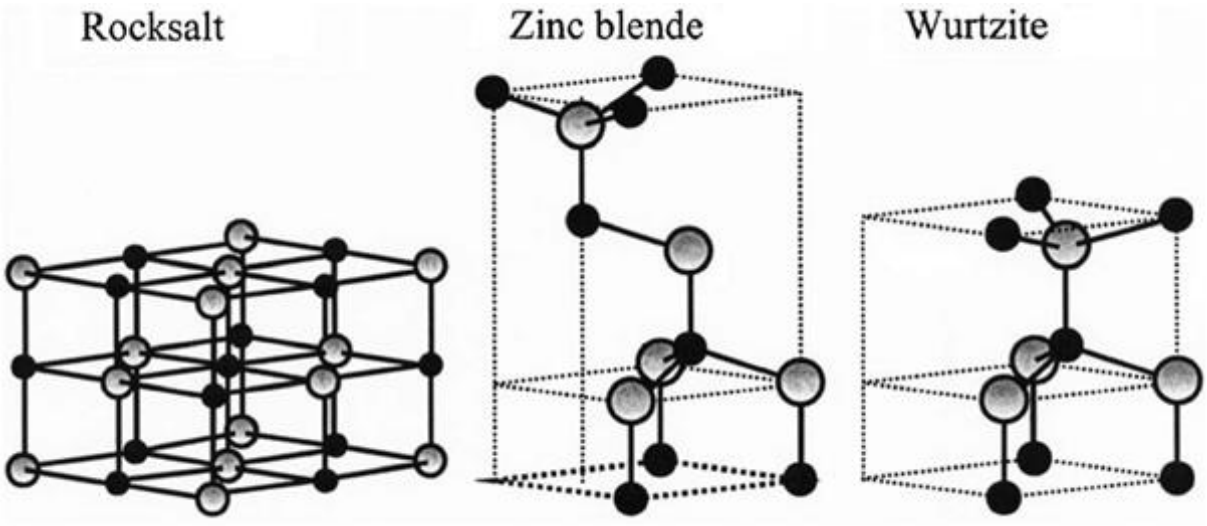

Figure 2. 16: Stick and ball representation of cubic rocksalt, cubic zinc blende and hexagonal wurtzite ZnO crystal formations. Zn and O atoms are represented by grey and black shading, respectively. [59].

2.7.2. Carbon Nanotubes (CNT)

Because of their unique structure and good electron transport capabilities, carbon nanotubes (CNT) have emerged as one of the main additions for improving the thermoelectric properties of organic materials [60]. Among several fillers, carbon nanotubes are the most widely utilized and effective. Because CNT have great electrical conductivity and rapid charge mobility, they can create conductive pathways when integrated into a polymer matrix [60]. Single-walled carbon nanotubes (SWCNT), few-walled carbon nanotubes (FWCNT), and multi-walled carbon nanotubes (MWCNT) are the three (3) forms of CNT [62]. CNT have a high conductivity due to the availability of free electrons due to the sp2-hybridized carbon atoms on the hexagonal plane of graphite [62]. SWCNT are classified as metallic or semiconducting based on their chirality [63], whereas MWCNT are classified as metallic if at least one layer displays metallic chirality [64]. FWCNT are renowned for having superior electronic characteristics than other CNT [65], as well as higher conductivity and field emission [66]. According to Javier et al [67], the addition of carbon nanotubes (CNT) to the polymer increases

the power conversion efficiency by three orders of magnitude compared with the device without CNT, but there is no clear connection with the number of walls or diameter of the nanotubes.

2.7.3. Poly(3-hexylthiophene) P3HT Polymer

Poly(3-hexylthiophene) (P3HT) is a versatile polymer that has been extensively researched as a material for electrical devices and organic solar cells [68]. P3HT is a conjugated electron-donor polymer that is widely used in solar cells due to its strong electro-optical characteristics and ease of process and manufacture [69-73]. P3HT is widely used in many of the most recent high-efficiency OPV devices and is regarded as a cornerstone in the development of future nanostructured polymer solar cells [73,74]. Therefore, it has a band gap of 1.9 eV and HOMO and LUMO energies of -4.8 and -2.9 eV, respectively. Figure 2.16 depicts the chemical structure of P3HT.

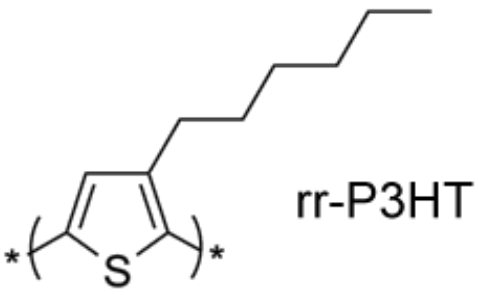

Figure 2. 17: The chemical structure of regio regular P3HT (rr-P3HT) [72].

2.8. Rare earth ions

Rare earths are generally found in the RE^{3+} trivalent state. Geijer found them in 1788 as a massive black stone named Ytteria in Ytterby, a Swedish town [75]. The first RE^{3+} element was discovered and named Yttrium with atomic number 36 from a hefty black stone, and after a comprehensive investigation of the stone, more RE^{3+} elements with atomic numbers Z = 57 to 71 were identified [76]. The optical properties of RE^{3+} ions are due to the internal f-electrons from cerium (Ce) to ytterbium (Yb). The basic electronic configuration of trivalent RE^{3+} ions is written $[Xe]4f^{n}\,5d^{0\text{-}1}6s^{2}$. Table 2.1 provides more details on the $4f^{n}$ configuration and shows the electronic configuration of trivalent RE^{3+} ions. RE^{3+} ions can act as dopants or impurities in some matrix matrices, enhancing their absorption, conductivity and magnetic properties among others.

Table 2. 1: Trivalent RE^{3+} ions electrical configuration [77].

Rare earth element	Symbol	Atomic number	Electronic configuration	Ionic radius (Å)
Lanthanum	La	57	[Xe] $5d^1\ 6s^2$	1.045
Cerium	Ce	58	[Xe] $4f^1\ 5d^1\ 6s^2$	1.010
Praseodymium	Pr	59	[Xe] $4f^3\ 6s^2$	0.997
Neodymium	Nd	60	[Xe] $4f^4\ 6s^2$	0.983
Promethium	Pm	61	[Xe] $4f^5\ 6s^2$	0.970
Samarium	Sm	62	[Xe] $4f^6\ 6s^2$	0.958
Europium	Eu	63	[Xe] $4f^7\ 6s^2$	0.947
Gadolinium	Gd	64	[Xe] $4f^7\ 5d^1\ 6s^2$	0.938
Terbium	Tb	65	[Xe] $4f^9\ 6s^2$	0.923
Dysprosium	Dy	66	[Xe] $4f^{10}\ 6s^2$	0.912
Holmium	Ho	67	[Xe] $4f^{11}\ 6s^2$	0.901
Erbium	Er	68	[Xe] $4f^{12}\ 6s^2$	0.890
Thulium	Tm	69	[Xe] $4f^{13}\ 6s^2$	0.880
Ytterbium	Yb	70	[Xe] $4f^{14}\ 6s^2$	0.868
Lutetium	Lu	71	[Xe] $4f^{14}\ 5d^1\ 6s^2$	0.861

2.9. Rare-earth ions dopants

Scientists encounter several obstacles in improving the efficiency, stability, and longevity of organic heterojunction solar cells (BHJ-OSCs). The proper design and manufacturing of BHJ-OSCs is critical for their development and commercialization. As a result, the primary issue is to manufacture BHJ-OSCs, with free-charge carrier creation being a vital stage [78]. Attempts are being undertaken, on the other hand, to manufacture and develop novel narrow bandgap polymers capable of capturing most of the solar energy spectrum [78,79,80]. Rare earth metal ions are widely utilized as dopants in a variety of applications due to their excellent electrical, optical, and luminescent capabilities, which are dependent on electron transition trends in 4f energy layers [81,82]. Among other rare earth elements Erbium (Er^{3+}), holmium (Ho^{3+}), thulium (Tm^{3+}), and samarium (Sm^{3+}) ions are of interest because they emit in the visible and near-infrared in this study. Senol [83] synthesized ZnO, Er-doped ZnO and Yb-doped ZnO by hydrothermal methods and observed reduced bandgap compared to undoped ZnO. Fabita et al. [84] synthesized Ho-doped ZnO using the sol–gel method and observed an increase in the bandgap with a change in the dopant concentration. Colak et al. [85] also observed a decreased optical bandgap of Tm-doped ZnO with increasing dopant concentration. Faraz et al. [86]

discovered the optical characteristics of Sm-doped ZnO and reported an improvement in the optical range in their absorption data, showing that rare earth doping is advantageous for efficient photocatalysts and/or photovoltaics to convert solar energy into electricity. Doping ZnO with rare earth ions should result in a shift to the lower XRD angle, indicating that the doping was effective. P3HT integration into ZnO:RE ions has been intensively researched to increase charge mobility and optical conductivity in OSCs. There are many reports of P3HT-ZnO focusing on various aspects such as improving power conversion efficiency (PCE) [87,88]. Incorporation of ZnO-doped P3HT can enhance electron transport and improve OPV efficiency.

References

[1] P. Kumar, Solar Cells Device Physics, Processing, Degradation, and Prevention, Taylor & Francis Group (2017) 1 – 2.

[2] https://education.nationalgeographic.org/resource/non-renewable-energy/ (accessed 20/09/2023).

[3] www.nonrewableenergy.com (accessed 20/09/2023)

[4]https://justenergy.com/blog/7-types-renewable-energy-future-of-energy/#:~:text=Renewable%20energy%20is%20energy%20that,less%20harmful%20to%20the%20environment. [Accessed 02/12/2022]

[5] A. Demirbas. Energy Sources, Part A: Recovery, Utilization, and Environmental Effects **28** (2006) 779 – 92.

[6] A. Inayata and M. Raza. A review. *Renew. Sust. Energ. Rev*. **107** (2019) 360 –373.

[7] A.M. Bagher, M.M.A. Vahid, B.M. Reza, M. Mohsen and G. Mahshi. *Bull. J. Adv. Sci. Res.* **01** (2015) 129 – 131.

[8] S. Farhad, M. Saffar-Avval, S. Younessi, *International Journal of Energy Research,* **32** (2008) 1 – 11.

[9] I. Kralova, J. Sjöblom, *Journal of Dispersion Science and Technology* 31 (2010) 409 – 25.

[10] I. Dincer, Energy Sources, Part A: Recovery, Utilization, and Environmental Effects **23** (2001) 69–81.

[11] R. E. H, Sims. Mitigation and Adaptation Strategies for Global Change, **8** (2003) 349 – 70.

[12] N. L. Panwar, S.C. Kaushik, Surendra Kothari, *Renewable and Sustainable Energy Reviews,* **15** (2011) 1513 – 1524.

[13] G. Boyle. Renewable Energy: Power for a Sustainable Future, 2nd ed. Oxford, UK: Oxford University Press, 2004.

[14] https://scienterrificgroup.com/2019/01/19/a-brief-history-of-photovoltaics/

[15]Mr.Solar, (August 13, 2015). Photovoltaic Effect [Online]. Available: http://www.mrsolar.com/photovoltaic-effect/

[16] N.F. Voudoukis, *EJECE,* **2** (2018) 1 – 7.

[17] R. Swami, *IJSRP*, **2** (2012) 1 – 5.

[18] http://www.chemistryexplained.com/Ru-Sp/Solar-Cells.html. [Accessed 02/12/2022]

[19]. M. Hiramoto, Springler International Publishing AG 2017, S. Kasap, P. Capper (Eds), Springler Handbook of Electronics and Photonic Materials.

[20] P. A. Basore, Defining terms for crystalline silicon solar cells. Progress in Photovoltaics: Research and Applications **2** (1994) 177-179.

[21] K. Marianna, R. Mikko, L. Markku, *BSMS*, **30** (2005) 1-31.

[22] D. A Jenny, R. H Bube, *Phys. Rev*, **96** (1954) 1190.

[23] M. C. Chia-Hao, R. B. Patrick, B. Vladimir, G. B. Moungi, *Nat. Mater,* **13** (2014) 796–801.

[24] S. Mathew, A. Yella, P. Gao, B. R. Humphry, B. F. E. Curchod, A. N. Ashari, I. Tavernelli, U. Rothlisberger, M. D. K Nazeeruddin, M. Grätzel, *Nat. Chem*, **6** (2014) 242–247.

[25] C. Qi, H. Zhou, Z. Hong, S. Luo, D. H. Sheng, H. H Wang, Y. Liu, G. Li, Y. Yang, *JACS*, **136** (2014) 622-25.

[26] D. G. McGehee, M. A. Topinka, *Nat. Mater,* **5** (2006) 675–676.

[27] J. M. Delia, G. Ilan, A. A. Paul, *MRS Bulletin,* **30** (2005) 41–44.

[28] B. O'Regan, M. Gratzel, *Nature,* **353** (1991) 737 – 740.

[29] A. Yella, H. W. Lee, H. N. Tsao, C. Yi, A. K. Chandiran, M. K. Nazeeruddin, W. G. E Diau, C. Y. Yeh, S. M. Zakeeruddin and M. Grätzel, *Science,* 334 (2011) 629 – 634.

[30] F. I. Lai, J. F. Yang, S. Y. Kuo, *Materials,* **8** (2015) 8860 – 8867.

[31] E. Gatto, R. Lettieri, L. Vesce, M. Venanzi, *Energies* 15 (2022) 5632.

[32] S. N. F. Mohd-Nasir, M. Y. Sulaiman, N. Ahmad-Ludin, M. A. Ibrahim, K. Sopian, and M. A. Mat-Teridi, *International Journal of Photoenergy*, (2014) 1 – 12.

[33] K. Kalyanasundaram, M. Gratzel, *J. Mater. Chem.* **22 (**2012) 24190 – 24194.

[34] J. Nozik, J. Miller, *Chem. Rev.* **110** (2010) 6443 – 6445.

[35] R. Luna-Rubio, M. Trejo-Peria, D. Vargas-Vázquez, G. Ríos-Moreno. *J, Sol. Energy*, **86 (**2012) 1077 – 1088.

[36] G. Muller-Furstenberger, M. Wagner, *Ecol. Econ.* **62** (2007**)** 648 – 660.

[37] M. R. Simmons, In The Coming Saudi Oil Shock and the World Economy; John Wiley & Sons: Hoboken, NJ, USA, 2005.

[38] W. Zhao, S. Li, H. Yao, J. Hou, *JACS* **139** (2017) 7148 – 7151.

[39] M. Deshpande, R. Seyezhai., *IJIRCCE*, **2** (2014) 3387 – 3392.

[40] M. Wright, A. Uddin, *Sol. Energy Mater. Sol. Cells*, **107** (2012) 87 – 111

[41] Y. H. Nam, J. W. Song, M. J. Park, A. Sami, J. H. Lee, *Nanotechnology* **28** (2017) 155402.

[42] M. Ikram, M. Imran, J. M. Nunzi, S. R. Bobbara, S. Ali, Islah-u-din, *J. Renewable Sustainable Energy*, **7** (2015) 043148.

[43] E. Groeneveld, C. Delerue, G. Allan, Y. Niquet, C. de Mello Donega, *J Phys Chem C,* 116 (2012) 23160 – 23167.

[44] R. Koole, E. Groeneveld, D. Vanmaekelbergh, A. Meijerink, C. Donega (2014) In: Donega CdM (ed) Nanoparticles: workhorses of Nanoscience, Ch. 2. Springer,

[45] F. T. Rabouw, C. de Mello Donega, *Top Curr Chem* (Z) **374** (2016) 58.

[46] P. Yua, J. Wub, L. Gaoc, H. Liub, Z. Wanga, *Sol. Energy Mater. Sol. Cells*, **161** (2017) 377 – 381.

[47] The magazine for the Photonics and Optoelectronics, **42** (2006).

[48] S. Ruhle, M. Shalom, A. Zaban, ChemPhysChem, **11** (2010) 2290 – 2304.

[49] T. Yang, Z. Zhang, Y. Ding, N. Yin, X. Liu, J Nanopart Res, **21** (2019) 101.

[50] T. L. Benanti & D. Venkataraman, *Photosynthesis Research,* **87** (2006) 73 – 81

[51] A. Wibowo, M. A. Marsudi, M. I. Amal, M. B. Ananda, R. Stephanie, H. Ardy and L. J. Diguna. *RSC Adv.,* **10** (2020) 42838.

[52] https://www.intechopen.com/chapters/42482. [Accessed 29/09/2022)

[53] H. Spanggaard, F. C. Krebs, Sol. Energy Mater. & Sol. Cells **83** (2004) 125

[54] R. A. M. Lameirinhas, J. P. N Torres, J. P. de Melo Cunha. A Photovoltaic Technology Review: History, Fundamentals and Applications. *Energies.* **15** (2022) 1823.

[55] C. Gumus, O. M. Ozkendir, H. Kavak, Y. Ufuktepe, *J. optoelect. Adv. Mat.* **8** (2006) 299.

[56] N. Rawal, A.G. Vaishaly, H. Sharma, B.B. Mathew, *EPES*, **2** (2015) 46 – 52.

[57] L. Znaidi, T. Touam, D. Vrel, N. Souded, S. B. Yahia, O. Brinza, A. Fischer, A. Boudrioua, *Proc. ICAAPMS* (2011).

[58] N. Babayevska, B. Peplinska, M. Jarek, L. Yate, K. Tadyszak, J. Gapinski, I. Iatsinskyi, S. Jurga, *RSC Adv.* **6** (2016) 89305.

[59] *Zinc Oxide: Fundamentals, Materials and Device Technology*. Edited by Hadis Morkoç and Ümit Özgür Copyright 2009 WILEY-VCH Verlag GmbH & Co. KGaA, Weinheim, ISBN: 978-3-527-40813-9

[60] Qu S, M. Wang, Y. Chen, Q. Yao, L. Chen, RSC.Adv. **8** (2018) 33855–33863.

[61] P.L. McEuen, M. S. Fuhrer, H. Park, IEEE Trans. Nanotechnol, **1** (2002) 78–85.

[62] Inmuddin, N. Shakeel, M. I. Ahamed, S. Kanchi, H. A. Kashmery, Nature research, **10** (2020) 5052.

[63] C. Dekker, Phys Today, 52 (1999) 22 – 28.

[64] L. Stavarache, A. Lepadatu, V. S. Teodorescu, M. L. Ciurea, V. Lancu, M. Dragoman, G. Kostantinidis, R. Buiculescu, *Nanoscale Research Letters,* **6** (2011) 88

[65] Y. Feng, H. Zhang, Y. Hou, T. P. McNicholas, D. Yuan, S. Yang, L. Ding, W. Feng, J. Liu, *ASC Nano*, **2** (2008) 1634–1638

[66] M. Ma, Z. Miao, D. Zhang, X. Du, Y. Zhang, C. Zhang, J. Lin, Q. Chen, *Biosensors and Bioelectronics* **64** (2015) 477–484.

[67] J. Arranz-Andrés, W. J. Blau, *Carbon*, **46** (2008) 2067-2075.

[68] J. J. R. Arias, M. F. V. Marques, *React. Funct. Polym*, **113** (2017) 58 – 69.

[69] J. A. Haucha, P. Schilinskya, S. A. Choulisa, R. Childersb, M. Bielea, C. J. Brabec, *Sol. Energy Mater. Sol. Cells* **92** (2008) 727 – 731

[70] N. D. Treat, et al., *Adv. Energy Mater.* **1** (2011) 82 – 89.

[71] C. Liu, Z. C. Holman, U. R. Kortshagen, *Nano Lett*. (2009) 3 – 6.

[72] L. E. Greene, M. Law, B. D. Yuhas, P. Yang, *J. Phys. Chem. C Lett.* (2007) 18.

[73] D. Chen, A. Nakahara, D. Wei, D. Nordlund, T. P. Russell, *Nano Lett.* (2011) 561 – 567.

[74] D. Dennler, M. C. Scharber, C. J. Brabec, *Adv mater* **21** (2009) 1323 – 1338.

[75] V. M. Bachmann, Studies on Luminescence and Quenching Mechanisms in Phosphors for Light Emitting Diodes, ISBN: 978-90-3934600-6 (2007).

[76] Y. Dwivedi and S. C. Zilio. *J. Nanosci. Nanotechnol.* **14** (2014) 1– 20.

[77] J. Chen and J.X. Zhao. *Sensors* **12** (2012) 2414 – 2435.

[78] L. M. Chen, Z. Hong, G. Li, Y. Yang, *Adv. Mater*, **21** (2009) 1434 – 1449.

[79] J. Peet, C. Soci, R. C. Coffin, T. Nguyen, Q. A. D. Moses, G. C. Bazan, *Appl. Phys. Lett*, **89** (2006) 2521051 – 2521053.

[80] C. Soci, I. W. Hwang, D. Moses, Z. Zhu, D. Waller, R. Gaudiana, C. J. Brabec, A. Heeger. J, *Adv. Funct. Mater*, **17** (2007) 632 – 636.

[81] X. H. Zhang, J. Chen, Y. Wu, Z. Xie, J. Kang, L. Zheng, *Physicochem. Eng. Aspects*, **384** (2011) 580–584.

[82] V. Kumar, O. M. Ntwaeaborwa, J. Holsa, D. E. Motaung, H. C. Swart, *Opt. Mater.*, **46** (2015) 510–516.

[83] S. D. Senol, *J Mater Sci: Mater Electron*, **27** (2016) 7767–7775.

[84] K. Fabitha, M. S. Ramachandra Rao, *J.Opt. Soc. Am. B*, **34** (2017) 2485–2492.

[85] H. Çolak, E. Karakose, *J.Rare Earths*, **36** (2018) 1067–1073.

[86] M. Faraz, F. K. Naqui, M. Shakir, N. Khare, *New J. Chem.* **42** (2018) 2295 – 2305, DOI: 10.1039/C7NJ03927A

[87] X. Chen, L. Chen, Y. Chen, *RSC Adv*, **4** (2014) 3627–3632.

[88] D. C. Olson, J. Piris, R. T. Collins et al, *Thin Solid Films*, **496** (2006) 26–29

Chapter 3

Experimental Methods

This chapter gives a brief description on wet-chemistry synthesis methods, and characterization techniques that were used in this study.

3.1 Sample preparation

3.1.1. Hydrothermal Synthesis

Hydrothermal method is the most widely used because the shape, size, and dimensions can be easily controlled by this synthesis. It is an easy and safe method that can gives a good yield of nanoparticles and free growth of catalyst at lower temperature [1]. Crystal growth occurs in an autoclave, which is a steel pressure vessel in which a medium of water is provided [1]. Hydrothermal method has the advantages in processing nanocrystalline materials for a wide range of technological applications such as electronics, optoelectronics, catalysis, ceramics, magnetic data storage, biomedicine, biophotonics, and solar cells, this technique has become one of the most important tools for advanced material editing [2]. Among the various methods for producing ZnO nanocrystals, the hydrothermal method is particularly interesting because of its low cost, ecological synthesis process at low temperature (about 90°C) [3]. This technique allows the materials synthesis with a high homogeneity and purity and also acts as one of the most attractive techniques for processing nanohybrid and nanocomposite materials [4,5].

3.1.2. Microwave Synthesis

The microwave synthesis approach is an easier and powerful manner to comprehend a chemical response for the guidance of nanomaterial compounds at quite low temperature [6-9]. The microwave radiation used in the synthesis reaction is to provide the energy required for the reaction, enabling particle size controlling features and also to accelerate the reaction [10]. The microwave radiation promotes the growth of the nanoparticles leading to the growth of crystalline nanoparticles [7]. This technique allows for precise temperature control. The temperature is maintained below the boiling point of the solvent to prevent rapid evaporation and can be controlled by adjusting the microwave power and irradiation time [7,10]. Microwave synthesis strategies have extensively attracted many researchers because of their

specific capabilities which include easier apparatus, tremendously localized heating and power green with quicker manner time [11]. Because of the direct heating of the response mixture, studies have shown that the microwave strategy is an enticing desire to stimulate responses and is powerful heating in comparison to typical warmth conduction tactics [12]. Furthermore, a number of the benefits is that the morphology of nanoparticles may be managed with the use of this approach. Ahmed et al [13] synthesized ZnO nanostructures using microwave heating approach. In their findings they used excessive decision TEM, and which indicates that debris are developing and are crystalline as XRD confirmed.

3.1.3. Sol-gel Synthesis

Sol-gel approach is a conventional wet chemical method that is considered powerful to alter the surface of the substrates. The most important advantage of sol-gel is to obtain high surface area and stable surfaces. Sol-gel method gives different benefits along with impressive control over the stoichiometry, homogeneous particle distribution, proper reactivity among components, nano-sized particles and permits lower processing temperatures [14]. These benefits make sol-gel method a completely appealing approach, especially in the case of photocatalytically active ZnO powders [15]. Chi et al [16] suggested that the size control of nanoparticles stays important for a success utility within the nanotechnology. Their research created a notion about the relationship between nanoparticle size and capping agent properties. As a result, they conclude that the capping agent job is to control the size of nanoparticles during synthesis process. Sol-gel synthesis using a capping agent such as ethylene diamine tetra acetic acid (EDTA), triethanolamine (TEA), tetraethylammonium bromide, oleic acid, and thioglycerol (TG) is therefore a potent, easy, and effective technique for controlling production of ZnO nanoparticles [17].

3.2. Techniques for characterization

3.2.1. X – Ray Diffractometer (XRD) spectroscopy

XRD is a rapid analytical technique primarily used for phase identification of a crystalline material and can provide information on unit cell dimensions [18]. It is also a very effective non-destructive analytical method for identifying the crystalline structure of solid materials such as ceramics, metals, electronic materials, organics, and polymers [19]. XRD is a handy technique for estimating the mean size of nano-crystallites in nano-crystalline bulk material. The sample is finely ground and homogenized, and the average bulk composition is computed

[20]. As a result, the constructive interference of a monochromatic X-ray beam diffracted at specified angles by each set of lattice planes in the sample produces X-ray diffraction peaks. The distribution of the atoms inside the lattice determines the strength of the peaks [19].

Bragg's law was used to explain the interference pattern of X-rays scattered by crystals, and diffraction has been developed to study the structure of all states of matter with any beam, e.g., ions, electrons, neutrons, and protons, with a wavelength similar to the distance between the atomic or molecular structures of interest [21]. The explanation of the observed angles of the diffracted x-ray beams was presented by William Lawrance Bragg and formulated the equation which relates wavelength to the angle of incident and d-spacing [22]. The Bragg equation is given by:

$$n\lambda = 2d \sin\theta \tag{3.1}$$

Where d is the spacing between diffraction planes, θ is the incident angle, n is any integer and λ is the wavelength of the beam. Fig. 3.1 shows the schematic diagram of Bragg's law [23]. A diffraction pattern is obtained by measuring the intensity of scattered waves as a function of scattering angle. The strong intensities known as Bragg peaks are obtained in the diffraction pattern when scattered waves satisfy the Bragg condition. The crystallographic planes that are used to define direction and distances in a crystal are identified by miller indices [21].

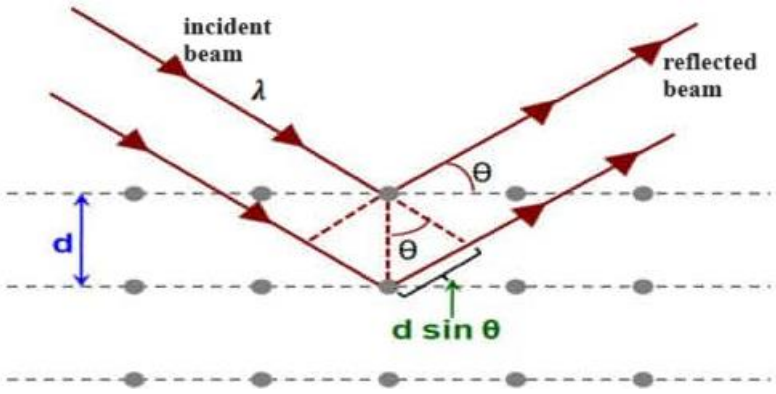

Figure 3. 1: The schematic diagram of Bragg's law [23].

The Rigaku SmartLab diffractometer system shown in Fig. 3.2 is outfitted with a high-powered 9kW Cu rotating anode generator. X-ray diffraction systems consist of three basic components: the X-ray tube, the sample holder and the X-ray detector. The XRD measurements were carried out using the SmartLab diffractometer, which was outfitted with a high-power 9 kW Cu rotating anode generator. The sample is manipulated with three-circles that is rotating via ω,

in-plane rotation ϕ and axis χ, and the detector moves with two-circles for in-plane measurements (2θ and 2θχ). The X-rays are generated in a cathode ray tube by heating a filament to create electrons. When the voltage is applied, the electrons will accelerate towards the target material, normally Cu, Fe, Mo and Cr. When electrons have enough energy to dislodge electrons from the inner shell of the target material, distinctive X-ray spectra are formed. [24]. The spectra generated by the x-ray diffractometer provide a structural fingerprint which can be distinguished by comparing data with electronic databases such as International Centre for Diffraction Data (ICDD) [25]. The crystallinity of the material can be identified by examining the diffraction pattern, that is; the widths of the peaks are related size, size distribution, defects and strain in nanocrystals. The average crystalline size, D can be estimated from the broadened peaks by using the Scherrer equation [20]:

$$D = \frac{k\lambda}{\beta Cos\theta} \tag{3.1}$$

Where *D* is the crystallite size (nm), *k* is the Scherrer constant (0.9), λ is the x-ray source's wavelength (0.15406 nm), β (radians) is the full width at half maximum (FWHM) and θ is the peak position in radians.

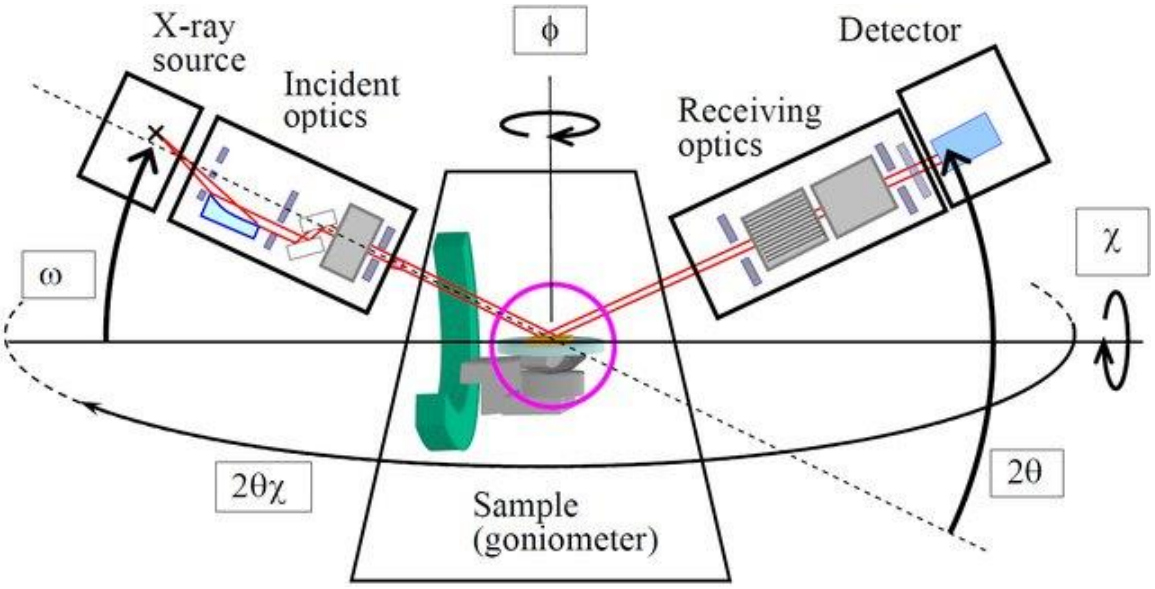

Figure 3. 2: The Rigaku SmartLab 9 kW X-ray diffraction system [26].

3.2.2. X – Ray Photoelectron Spectroscopy (XPS)

XPS is a non-destructive technique that enables chemical analysis of the outermost 5-10 nm of any vacuum-compatible solid. XPS determines the elemental makeup, empirical formula, chemical state, and electronic state of elements in a material [27]. Only electrons generated in the first XPS atomic layers are detected. XPS is used to analyze surfaces and investigate the characteristics of atoms in a material. It is used to calculate the binding energy of electrons in atoms and molecules on a material surface. XPS is a valuable technology not just for showing what materials are within a film, but also for showing additional elements that are attached to it. Each element generates a distinct collection of XPS peaks with distinct binding energies, allowing each element present within or on the surface of the studied material to be identified. These spectrum peaks relate to the electron configuration of the electrons within the atoms, for example, 1s, 2s, 2p, 3s, and so on. However, the equipment will often only probe 12nm into a material. XPS spectra are created by exposing a material to an X-ray beam while simultaneously measuring the kinetic energy and quantity of electrons that escape from the top 1 to 12 nm of the substance to be examined. Ultra-high vacuum (UHV) conditions are required for XPS to avoid collision between photoelectrons and gas molecules in the spectrometer and minimize surface contamination from residual gases [28]. XPS identifies photoelectrons generated by a sample as a result of being exposed to single-energy X-ray photons (Fig. 3.3). The photoelectric effect discovered by Hertz in 1887 [29, 30] is the fundamental concept of XPS, which was extended to surface analysis by K. Siegbahn and his research group at Uppsala University, Sweden, in the mid-1960s.

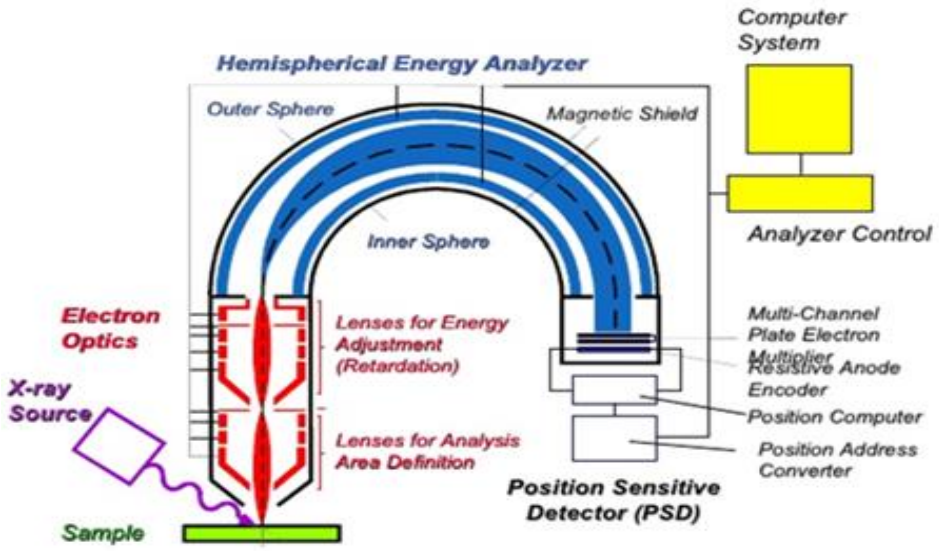

Figure 3. 3: The schematic diagram of x-ray photoelectron spectroscopy hemispherical analyser [26].

3.2.3. Scanning Electron Microscopy (SEM)

The SEM is an electron microscope that uses a beam of reflected electrons to scan the surface of a sample to create an image. A sample examination can provide information about a material's topography, morphology, composition, and crystallography [31]. SEM offers several benefits over traditional microscopes, including a high depth of field that allows numerous samples to be focused at the same time [32]. It also has a significantly greater resolution, allowing samples to be zoomed in much farther [32]. Because SEM employs electromagnets rather than lenses, the researcher has far more control over the degree of magnification [31]. All of these benefits, along with extremely remarkable picture sharpness, make SEM one of the most helpful research tools available today [31] (see Fig. 3.4). This tool allows you to study the surface morphology of a nanomaterial by generating high-resolution images of shapes.

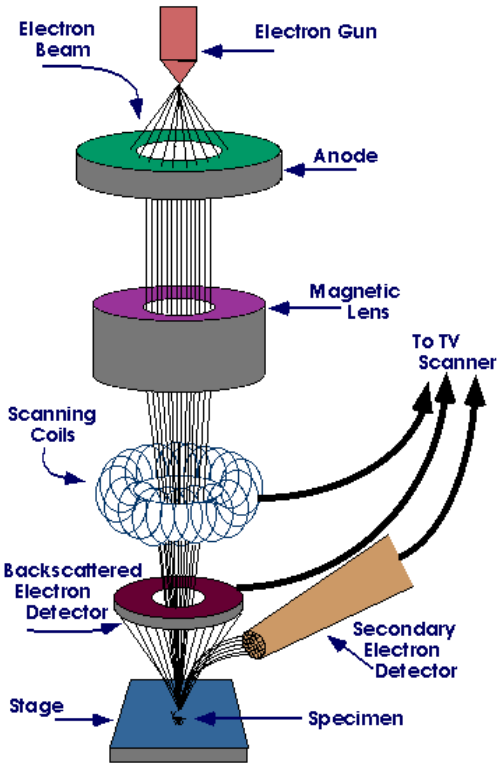

Figure 3. 4: The schematic diagram of SEM [31].

3.2.4. Ultraviolet – Visible -Near Infrared absorption Spectroscopy (UV/VIS/NIR)

Ultraviolet-visible (UV/VIS/NIR spectroscopy refers to absorption or reflectance spectroscopy in the UV/VIS/NIR spectral region [33]. This means that both visible and near-infrared light (near-UV and near-infrared [NIR]) are utilised. The absorption or reflectance of the substances involved in the visible spectrum has a direct effect on their perceived color [34]. Light reflectance can also be measured using the UV/VIS/NIR spectrophotometer. UV/VIS/NIR spectroscopy is used to investigate the band gap energy and size distribution of nanoparticles, as well as optical features such as absorption bands. The Tauc's plot may be used to estimate the bandgap energy and size distribution of nanoparticles. Tauc's plot is a graphical approach for calculating the optical bandgap of an amorphous or semiconductor material [35]. It is very beneficial for semiconductors, insulators, and thin films. The bandgap energy is an important characteristic because it represents the smallest amount of energy necessary to excite an electron from the valence band to the conduction band, allowing the material to conduct electricity [36]. The optical bandgap is calculated using the linear part of the Tauc's plot [36] by using the equation 3.1.

$$\alpha hv = A(hv\text{-}Eg)^{1/2} \quad (3.1)$$

The light source comprises of a Xenon lamp for UV, visible (Vis), and near infrared wavelengths. To measure the solution samples cuvette has to be used. The lamp flashes to concentrate on a glass, which directs the light beam onto a cuvette containing the sample solution; the beam then travels through the sample, absorbing certain wavelengths by the sample components (Fig. 3.5).

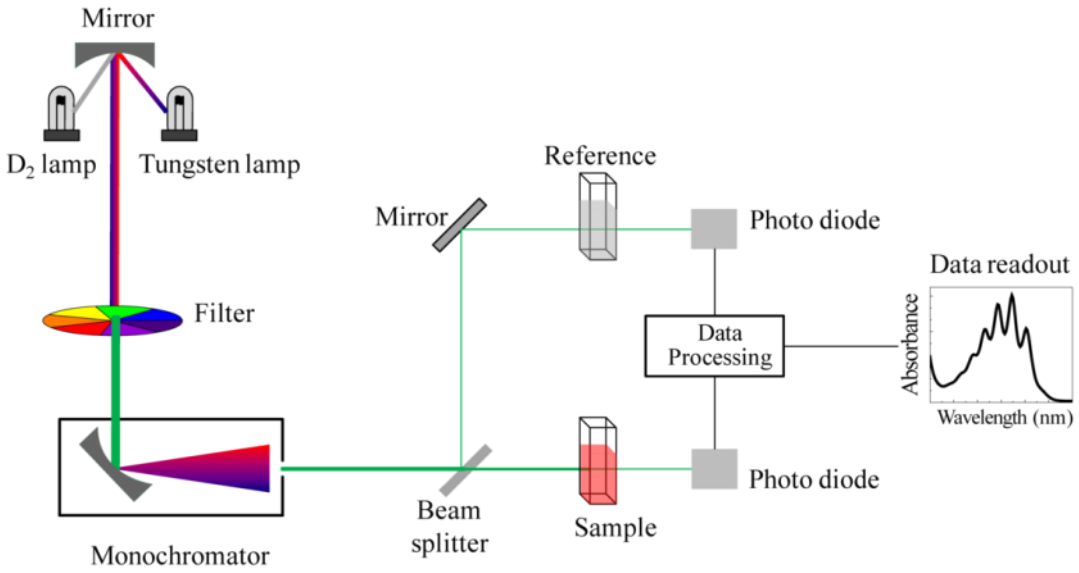

Figure 3.5: The schematic diagram of UV/VIS/NIR spectroscopy optical pathway [34].

3.2.5. Photoluminescence Spectroscopy (PL)

Photoluminescence spectroscopy is contactless non-destructive technique for studying the optical response of a material under the influence of optical excitation. This technique is used to provide the detailed information about discrete electronic states, including intrinsic and extrinsic defects. Photoluminescence (PL) is the emission of light from any form of matter after the absorption of photons (electromagnetic radiation). It is one of many forms of luminescence (light emission) and is triggered by photoexcitation (excitation by photons), hence the prefix photo [37]. The photoexcitation forces the material to a higher electronic state, then it relaxes and returns to a lower energy level, releasing energy (photons) [38]. Therefore, it is used to measure various important material properties such as semiconductors which includes impurity levels, defects and recombination of mechanisms.

The recombination of electrons and holes results in the emission of photons with energy equal to the material bandgap. This can include both radiative and nonradiative processes, where nonradiative is associated with localized defect levels [39]. In direct recombination as illustrated in Fig. 3.6, an electron from the conduction band falls into a hole in the valence band

while preserving energy by producing a photon. The excess carriers reach thermal equilibrium before recombination; therefore, most emitted photons have energy equal to the bandgap energy [38]. The materials bandgap thus influences the colour of the emitted light, which may be changed by changing the semiconductor material [39].

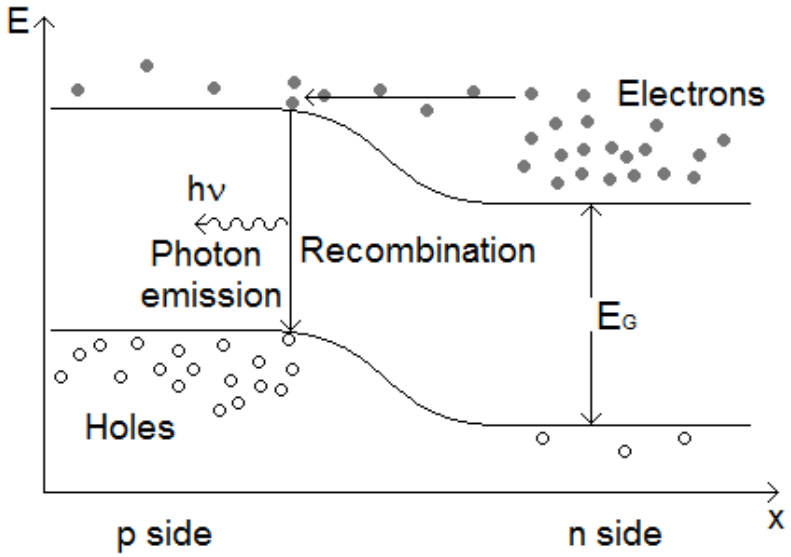

Figure 3. 6: Schematic diagram to show the recombination process in a p-n type material [39].

3.2.6. Fourier transform Infrared Spectroscopy (FTIR)

The most popular approach for infrared spectroscopy is Fourier transform infrared spectroscopy (FTIR). An infrared absorption, emission, photoconductivity, or Raman scattering spectrum of a solid, liquid, or gas is obtained using this approach [40]. It is used to determine qualitative and quantitative properties of organic or inorganic molecules active in the infrared [41]. The FTIR spectrometer simultaneously collects data with high spectral resolution over a wide spectral range [40]. Infrared spectroscopy is a technique that analyses the vibrations of atoms in a molecule and is unquestionably one of the most significant analytical techniques accessible to scientists today [42]. It is also a mathematical technique that can be used to convert a function from one real variable to another [43]. It is a unique powerful tool for spectroscopists as various spectroscopic studies deal with electromagnetic waves covering a wide range of frequency [44]. Fourier transform spectroscopy is a less obvious method of obtaining the same information. [40]. Rather of projecting a monochromatic light beam onto the sample, the approach concurrently emits a beam comprising many light frequencies and assesses the quantity of this beam absorbed by the sample [40]. The beams were subsequently changed to incorporate a new frequency combination, providing a second

data point [40]. This procedure is carried out multiple times. The computer then compiles all of this information and works backwards to determine the absorbance multiplied by the wavelength. The schematic diagram for FTIR is shown in Fig. 3.7.

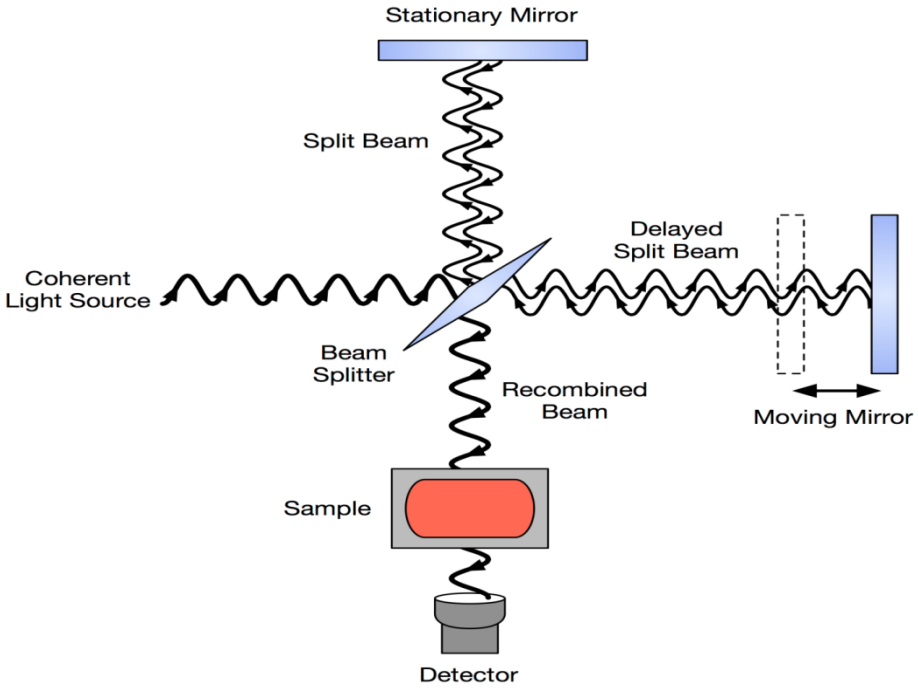

Figure 3. 7: The schematic diagram of FTIR [40].

3.2.7. Current-Voltage Characterization (I-V)

Current-voltage (I-V) characteristics describe the relationship between the current flowing through a component and the voltage across it [45] (see Fig. 3.8). This means that the resistance is constant, and the voltage is directly proportional to the current flowing through the element at a constant temperature. The I-V curve shows the linear relationship between the applied voltage and the electric current [45] (see Fig 3.9. Measurements are made by applying a range of voltages to the device. Thus, at any voltage, the current flowing through the device is measured with high accuracy.

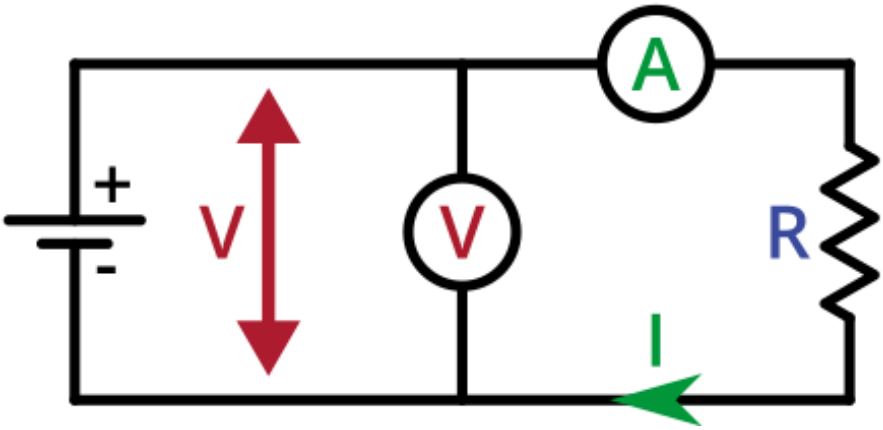

Figure 3. 8: The circuit diagram for I-V measurements of a resistor [45].

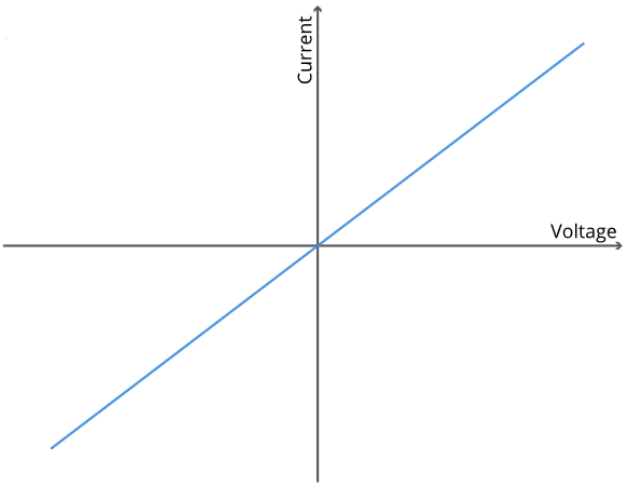

Figure 3. 9: The I-V curve of an ideal resistor [45].

References

[1] H. Hayashi, Y. Hakuta, *Materials* **3** (2010) 3794-3817.

[2] K. Byrappa, T. Adschiri, *PCGCM*, **53** (2007) 117-166.

[3] K. H. Tam, C. K. Cheung, Y. H. Leung, A. B. Djuris, C. C. Ling, C. D. Beling, S. Fung, W. M. Kwok, W. K. Chan, D. L. Phillips, L. Ding, W. K. Ge, *J. Phys. Chem. B,* **110** (2006) 20865-20871.

[4] S. Alshehri, S. Al-Shehri, H. Ali, A. A. Hassaneen, M. S. Aida, *Inorganic Chemistry Communications*, **156** (2023) 111201.

[5] K. Byrappa, T. Adschiri, *Progress in Crystal Growth and Characterization of Materials*, **53** (2007) 117 – 166.

[6] A. K. Singh, S. B. Patil, S. S. Multani, *IJPAP*, **49** (2011) 270-276.

[7] A. K. Singh, V. S. Raykar, *Colloid & Polymer Science*, **286** (2008)1667-1673.

[8] R. S. Varma, *COCE*, **1** (2011) 1-6.

[9] C. M. Sarah, S. K. Pillai, S. S. Ray, K. Jalama, R. W. M. Krause, *J. Nanomater*, 2012, Article ID: 691503.

[10] Kazi Rakib Ahammed, Md. Ashaduzzaman, Shujit Chandra Paul, Mithun Rani Nath, Snahasish Bhowmik, Otun Saha, Md. Mizanur Rahaman, Shukanta Bhowmik, Tutun Das Aka, *SN Applied Sciences*, **2** (2020) 955.

[11] M. Hasanpoor, M. Aliofkhazraeia, H. Delavaria. Proc. Mater. Sci, **11** (2015) 320 – 325.

[12] M. Nüchter, B. Ondruschka, W. Bonrath, A. Gum, Green Chem, (2004) 128- 141.

[13] F. Ahmed, S. Kumar, N. Arshi, M. S. Anwar, R. Prakash, *Adv. Mat. Lett*, **2** (2011) 183-187.

[14] A. Zelati, A. Amirabadizadeh, A. Kompany, *IJCEA* (2011) 02.

[15] Z. Liu, J. Deng, F. Li, *Mater. Sci. Eng. B,* **150** (2008) 99 – 104.

[16] Chi M. P, Hoang M. N, *J. Phys. Chem. A*, **121** (2017) 3213−3219

[17] P. Chandrasekaran, G. Viruthagiri, N. Srinivasan, J Alloys Comp, **540** (2012) 89–93.

[18] A. Maqsood, K. Iqbal, *J. Pak. Mater. Soc.* **1** (2010) 4.

[19] J. Melorose, R. Perroy, S. Careas, *Statew. Agric. L. Use Baseline* **1** (2015).

[20] B. D. Cullity, Stock S. R, Elements of X-ray diffraction, 3rd Ed. Upper Saddle River, N.J. Pearson/Prentice Hall, ISBN 0-13-178818-3 2001.

[21] https://web.pdx.edu/~pmoeck/phy381/Topic5a-XRD.pdf. [Accessed 21/09/2023]

[22]http://www.lscollege.ac.in/sites/default/files/e-content/Bragg%27s%20law%20%282%29.pdf. [Accessed 21/09/2023]

[23] https://qsstudy.com/significance-braggs-equation/. [Accessed 21/09/2023]

[24] B. M. Mothudi, PhD thesis, University of the Free State, 2009.

[25] G. Gao, Nanostructures and Nanomaterials: Synthesis, Properties & Applications, 6th edition, London, 2004.

[26] K. Inaba, S. Kobayashi, K. Uehara, A. Okada, S.L. Reddy and T. Endo. *Advances in Materials Physics and Chemistry* **3** (2013) 72 – 89.

[27] J. F. Moulder, W. F. Stickle, P. E. Sobol, K. D. Bomben, Handbook of X-ray Photoelectron Spectroscopy, (1995) 255.

[28] H. Seyama, M. Soma, B.K.G. Theng, *Elsevier,* **5** (2013) 161 – 176.

[29] K. Siegbahn, *Phys. Rev.* **105** (1957) 1676.

[30] K. Larsson, E. Sokolowski, and K. Siegbahn, *Ark. Fys.* **13** (1958) 483.

[31] https://www.purdue.edu/ehps/rem/rs/sem.html. [Accessed 10/10/2022]

[32] B. Hafner, "Scanning Electron Microscopy Primer," *Characterization Facility, University of Minnesota, pp.1-29*, 2007.

[33] Weckhuysen B. M, Schoonheydt R. A, *Catal. Today*, **49** (1999) 441.

[34] https://en.wikipedia.org/wiki/Ultraviolet%E2%80%93visible_spectroscopy. [Accessed 10/10/2022].

[35] *R. A.* Street, *(1991). Hydrogenated amorphous silicon. Cambridge Univ. Press, Cambridge. ISBN 0-521-37156-2.*

[36] H. Oh, J. Krantz, I. Litzov, T. Stubhan, L. Pinna, C.J. Brabec, *Sol Energy Mater Sol Cells,* **95** (2011) 2194 – 2199.

[37] Y. Cong, J. Zhang, F. Chen, M. Anpo, *J. Phys. Chem. C,* **111** (2007) 6976–6982.

[38] Y. Povrozin and B. Barbieri. Fluorescence Spectroscopy **(2016)** John Wiley & Sons: Handbook of Measurement in Science and Engineering.

[39]https://warwick.ac.uk/fac/sci/physics/current/postgraduate/regs/mpagswarwick/ex5/devices/led/ [Accessed 10/10/2022]

[40] B. C. Smith, Fundamentals of Fourier Transform Infrared Spectroscopy, Taylor & Francis Group, LLC, New York, (2011).

[41] http://www.pitt.edu/~mramsey/papers/GAC2.pdf. [Accessed 10/10/2022]

[42] B. Stuart, Infrared Spectroscopy: Fundamentals and Applications, **(2004)** John Wiley & Sons, Ltd.

[43]http://www.kinetics.nsc.ru/chichinin/books/spectroscopy/Stuart04.pdf.[Accessed 10/10/2022]

[44]http://chemwiki.ucdavis.edu/Physical_Chemistry/Spectroscopy/Fundamentals/.
[Accessed 10/10/2022]
[45] https://www.bbc.co.uk/bitesize/guides/zgbwpbk/revision/3. [Accessed 10/10/2022]

Chapter 4

Effect of ZnO nanorods singly doped with Er^{3+}, Ho^{3+}, and Tm^{3+} on P3HT for organic solar cell application

The Chapter discusses the effect of ZnO nanorods singly doped with Er^{3+}, Ho^{3+}, and Tm^{3+} on P3HT for organic solar cell application were discussed.

4.1 Introduction

ZnO is a semiconductor material of tremendous relevance for optoelectronic applications because of its large band gap (3.37 eV) and strong exciton binding energy [1-2]. ZnO is recognized for three typical forms of unit cell structures: hexagonal wurtzite, zinc blende, and rock salt, with hexagonal wurtzite being the most popular because to its stability at ambient temperature and normal atmospheric pressure [1]. It is also non-toxic and can be produced in small or large scale using various synthesis methods. ZnO doped with different rare earth ions used for various applications such as optoelectronics, electronics, photocatalytic have been studied for different morphologies and preparation methods [4-6]. The main of ZnO doping is to modify its optical properties by improving the absorption [4]. Rare earth metal ions are widely utilized as dopants in a variety of applications due to their excellent electrical, optical, and luminescent capabilities, which are determined by the electron transition trends in the 4f energy layers [7,8]. Among others, various rare earth metal ions such as Er^{3+}, Ho^{3+} and Tm^{3+} are of interest because they emit in the visible and the near-infrared range. Senol [9] synthesized Er-doped ZnO and Yb-doped ZnO using hydrothermal method and observed a decrease in band gap compared to the one of ZnO, which might be due to the increased defects introduced by Er^{3+} and Yb doping. Fabitha et al. [10] synthesized Ho-doped ZnO by sol-gel method and observed band gap growth as the impurity concentration was varied,.The band gap increased with an increasing concentration of Ho^{3+} dopant in the ZnO crystal. Colak et al. [11] also observed a decrease in the optical band gap of Tm-doped ZnO with increasing dopant concentration. Our main aim in this study is to instigate these materials due to their potential application prospects in optoelectronic devices, organic-inorganic semiconductors. [12]. The

hybrid heterostructure based on pristine P3HT-conjugated polymer including inorganic ZnO:RE nanoparticles is intended to improve its optoelectronic capabilities by taking use of ZnO high electron mobility [13]. The electrical conductivity of organic semiconductors has been known for at least four decades and a proof of-concept was presented shortly after their discovery [14,15]. Recent active heterojunction organic solar cells have achieved laboratory-scale energy conversion efficiencies of up to 11.2% [16]. In contrast to many other technologies, these solar cells can be printed with a solution, even on film or flexible paper [17, 18].

In this study, rare-earth ions doped ZnO nanorods were synthesized using sol-gel microwave assisted. Optimization of Er^{3+}, Ho^{3+} and Tm^{3+} in ZnO nanorods was achieved and ZnO doped with 1.5% Er^{3+}, 0.5% Ho^{3+} and 1.0% Tm^{3+} were found to be the best samples. The materials were then integrated into P3HT with an aim of investigating its role on structural, optical, and electrical characteristics. P3HT-ZnO: 0.5% Ho^{3+} quenches P3HT intensity, reducing charge recombination and demonstrating full charge transfer between donor-acceptor materials. Kabongo et. al [19] demonstrated the surface effect and optoelectronic properties of Ho^{3+} doped ZnO in P3HT polymer nanocomposite. In their study they observed the PL quenching which is the results of enhanced charge transfer due to ZnO:Ho^{3+} nanostructures in the polymer. According to Kabongo et. al [19] the degree of quenching of the polymer photoluminescence is a good indication of efficient charge transfer induced by the ZnO:Ho^{3+} (acceptor) dispersed in the P3HT (donor) host matrix. To regulate particle size and decrease particle agglomeration, the capping agent 1-thioglycerol was utilized. The aim is to improve the conductivity of P3HT, which is known to improve the efficiency of organic solar cells. The nanorods act as direct carrier transport pathways to the electrode, reducing charge transfer. These heterostructures are intriguing because they act as electron transport layers in organic-inorganic heterojunction solar cells, bringing up possibilities for use in a variety of optoelectronic devices, including solar cells.

4.2 Experimental Procedure

4.2.1 Materials

The precursors used for the synthesis of ZnO doped with rare earth ions were zinc acetate dihydrate ($Zn(CH_3COO)_2 \cdot 2H_2O$; 99.5%), 1-thioglycerol (TG), sodium hydroxide (NaOH; 97%), $Er(NO_3)_3$, $Ho(NO_3)_3$, $Tm(NO_3)_3$, poly(3-hexylthiophene) (P3HT). All the precursors

were purchased from Sigma Aldrich without further purification. Deionized water (DIW) and chlorobenzene were used as solvents. Microwave processing was done using a SynthWAVE single reaction chamber microwave synthesis system.

4.2.2 Microwave-assisted sol-gel synthesis

The hexagonally shaped nanorods were synthesized by dissolving zinc acetate dihydrate ($Zn(CH_3COO)_2H_2O$; 99.5%) in deionized water, adding 1-thioglycerol (TG) as a capping agent, and stirring the solution for 15 minutes on a magnetic stirrer. Erbium(III) nitrate pentahydrate ($Er(NO_3)_3•5H_2O$ (99.9%), holmium(III) nitrate pentahydrate ($Ho(NO_3)_3•5H2O$ (99.9%), and thulium(III) nitrate pentahydrate ($Tm(NO_3)_3•5H_2O$ (99.9%) were used as dopants. The presence of TG in the solution was used to regulate particle size distribution. Kumari et. al [20] investigated the thermal stability of TiO_2 nanoparticles using 1-thioglycerol as a capping agent. The major role of 1-thioglycerol in their studies was to prevent the agglomeration of nanoparticles and to improve the thermal stability. On the other hand, sodium hydroxide (NaOH; 97%) was dissolved in deionized water for 15 minutes while agitating the mixture. The sodium hydroxide solution was then dropped into the zinc solution. The white solution was then swirled for 1 hour at room temperature on the magnetic stirrer. The solution was then transferred to the synthWAVE microwave for 5 minutes at 140 ^oC and 1000 W power. The mixture was then centrifuged at 4000 rpm for 5 minutes before being rinsed numerous times with deionized water and ethanol to remove acetates and nitrates. As a result, the finished product was disseminated in ethanol. P3HT was dissolved in chlorobenzene and stirred for 24 hours on a magnetic stirrer to combine it with un-doped and doped ZnO at varying ratios. The samples were sonicated for 30 minutes after integrating P3HT with un-doped and doped ZnO. To create the thin films, the pipette was used to drop-cast the sample solution onto the borosilicate glass substrate. The films were then allowed to dry at ambient temperature. All of the precursors were bought from Sigma Aldrich and were not further purified.

4.2.3 Characterization techniques

The structure and crystallinity of the produced materials were evaluated using a Rigaku SmartLab X-Ray diffractometer with a Cu-Kα radiation source (λ = 0.154059 nm). A PerkinElmer FTIR spectrometer was used to determine functional groups. The absorbance was measured using a PerkinElmer Lambda 1050 UV/VIS/NIR Spectrophotometer. FE-SEM pictures were captured using a JEOL JSM-7800F and a Thermo Scientific Ultradry EDS detector. PL measurements were taken using a Horiba Fluorolog-3 Jobin Yvon spectrometer at

excitation wavelengths of 370, 400, and 530 nm. Thermo ESCAlab 250 Xi spectrometer data was collected using Al K (1486.7 eV) monochromatic x-ray radiation source and was internally calibrated by carbon deposit C (1s) binding energy (BE) at 284.8 eV. Keithley 6487 picoammeter with a voltage source was used to measure current-voltage (I-V). The measurements were done in the dark and at room temperature using the thin film (303 K).

4.3. Results and discussion

4.3.1 X-ray diffraction analysis

Fig. 4.1 (a – c) shows diffraction patterns of ZnO doped with Er^{3+}, Ho^{3+} and Tm^{3+}. Clearly patterns shows that the peaks correspond to the hexagonal structure of wurtzite ZnO (PDF 01-074-9940) and that no secondary phase originating from $Zn(OH)_2$, Er_2O_3, Ho_2O_3 and Tm_2O_3 was observed, indicating the formation a single phase. The ZnO lattice is known to be open to doping, but due to difference in ionic radius, so it is difficult to stabilize impurities in the ZnO lattice without creating secondary order. However, with increasing impurity concentration (0.5 - 1.5 %) a slight shift of the peak towards the lower angle is to be expected indicating the replacement of Zn^{2+} ions in the main lattice with Zn^{2+} having a smaller ionic radius (0. 74 Å) than the radius of Er^{3+} (0,89, 0.90 and 0.87 Å for Er, Ho and Tm (see Fig. 4.1 (d)). The hexagonal wurtzite structure can still be seen in Fig. 4.1(e) diffraction patterns of doped materials with P3HT inclusion. The incorporation of P3HT with doped samples improved the crystallinity of ZnO, which was confirmed by highly crystalline peaks, especially in the case of Ho^{3+}. Charge recombination between donor-acceptor materials is expected to be reduced in photoluminescence (PL) analysis. The average crystal size was found to be approximately 35, 31, 34 and 29 nm for ZnO and ZnO doped with Er^{3+}, Ho^{3+} or Tm^{3+}. The mean crystallite size was calculated using the Scherrer equation [19].

$$D = \frac{k\lambda}{\beta Cos\theta} \tag{4.1}$$

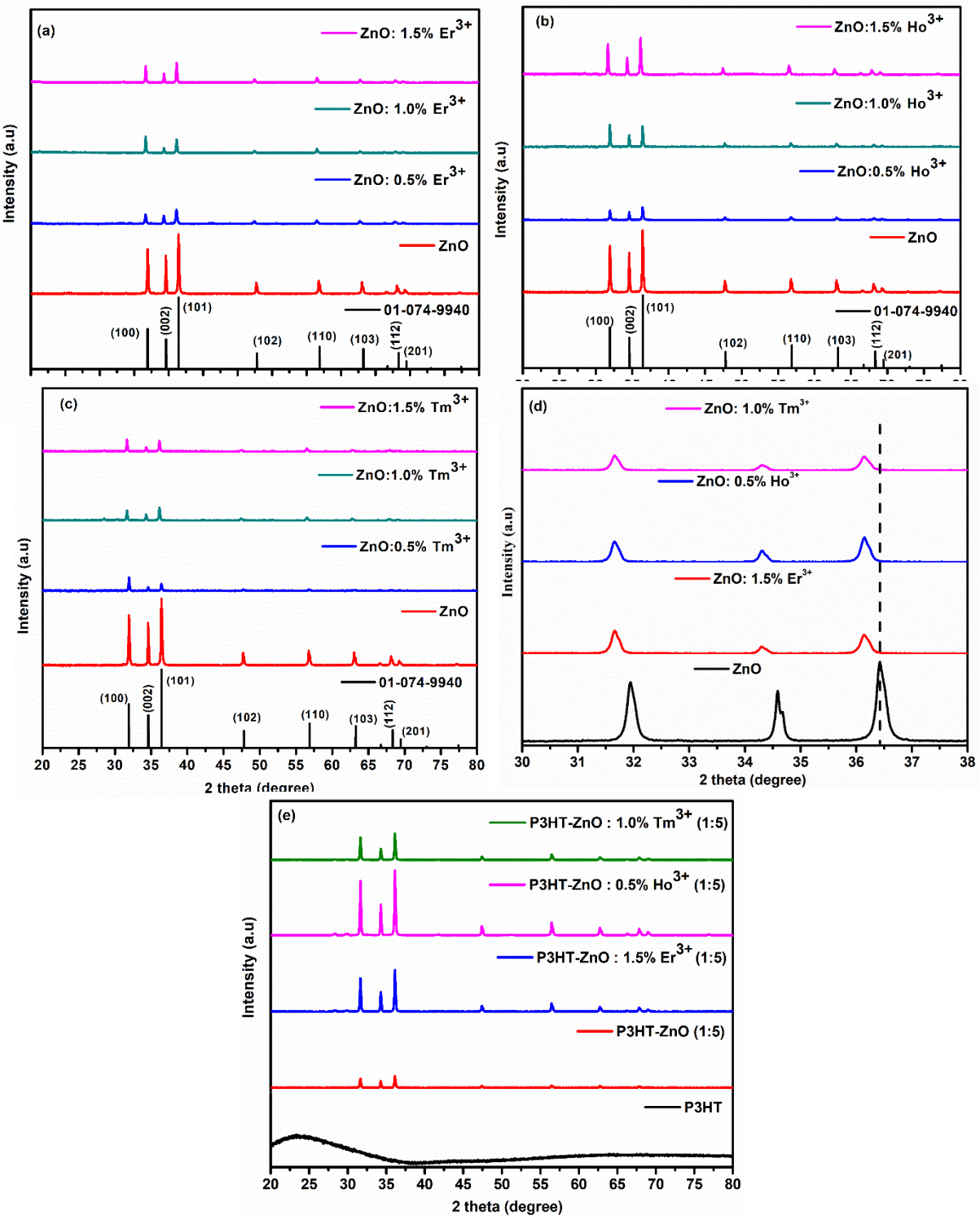

Figure 4. 1: XRD patterns of (a) Er-doped ZnO, (b) Ho-doped ZnO (c) Tm-doped ZnO (d) peak shift (e) incorporation of P3HT in doped samples.

4.3.2 Ultraviolet-visible-Near Infrared analysis

UV/VIS/NIR absorption spectra of ZnO doped with various rare earth ions are shown in Fig. 4.2. ZnO has a maximum normalized absorption peak at ~370 nm, with absorption mostly focused in the UV area and less visible light absorbed. Fig. 4.2 (a – c) shows the normalized

absorption spectra of ZnO doped with Er^{3+}, Ho^{3+} and Tm^{3+} ions. The figure shows that ZnO doped with 1.5% Er^{3+}, 0.5% Ho^{3+} and 1.0% Tm^{3+} have the highest absorption intensity. However, Er^{3+} and Ho^{3+} doped ZnO show a slight redshift from ~370 nm. The absorption spectrum shifts for Er^{3+} and Ho^{3+} doped ZnO is probably due to the development of defects in the ZnO host matrix, energy levels between the valence and conduction bands. The absorption band at ~370 nm is attributed to the transition of electrons from the valence band to the conduction band. The redshift is therefore attributed to the effective impurity band introduced by doping [21]. Similar results were reported by Yu et al. [22] where they observed a slight redshift showing the rate of electron-hole pairing exhibiting higher photocatalytic efficiency.

The normalized absorption spectra of P3HT and P3HT-ZnO in varied ratios (1:1-1:5) are shown in Fig. 4.2 (d), with P3HT-ZnO (1:5) having the maximum absorption. Fig. 4.2 (e) shows normalized absorption spectra of P3HT at different ratios, P3HT, P3HT-ZnO, P3HT-ZnO: 1.5% Er^{3+}, P3HT-ZnO: 0.5% Ho^{3+} and P3HT-ZnO: 1.0% Tm^{3+}. The findings demonstrate that P3HT-ZnO: 0.5% Ho^{3+} has the highest absorption intensity. It is well known that increased absorption leads to increased efficiency of solar cells [23]. The spectra demonstrate that all samples contain the identical vibronic modes of the excited state absorption peaks, which are ascribed to the π-π* P3HT transitions [24]. The optical band gap was calculated using the linear part of the Tauc's plot [25]:

$$\alpha h\nu = A(h\nu\text{-}Eg)^{1/2} \quad (1)$$

Where A is the constant, $h\nu$ is the photon energy (h=Plank's constant and ν is frequency of a photon) and α is the absorption coefficient. Extrapolating from the linear part of Tauc's plot ($(\alpha h\nu)^2$ vs $h\nu$) the anticipated bandgaps are shown in Fig. 4.2 (f). The predicted bandgaps were found to be ~3.09, 2.53, 2.61 and ~2.23 for ZnO, ZnO doped with 1.5% Er^{3+}, 0.5% Ho^{3+} and 1.0% Tm^{3+} respectively. The bandgaps exhibit a blue shift because TG and dopants generate a new electronic level within the ZnO host structure. The bandgap for P3HT, P3HT-ZnO and P3HT to doped samples range between 1.8 and 1.9 respectively.

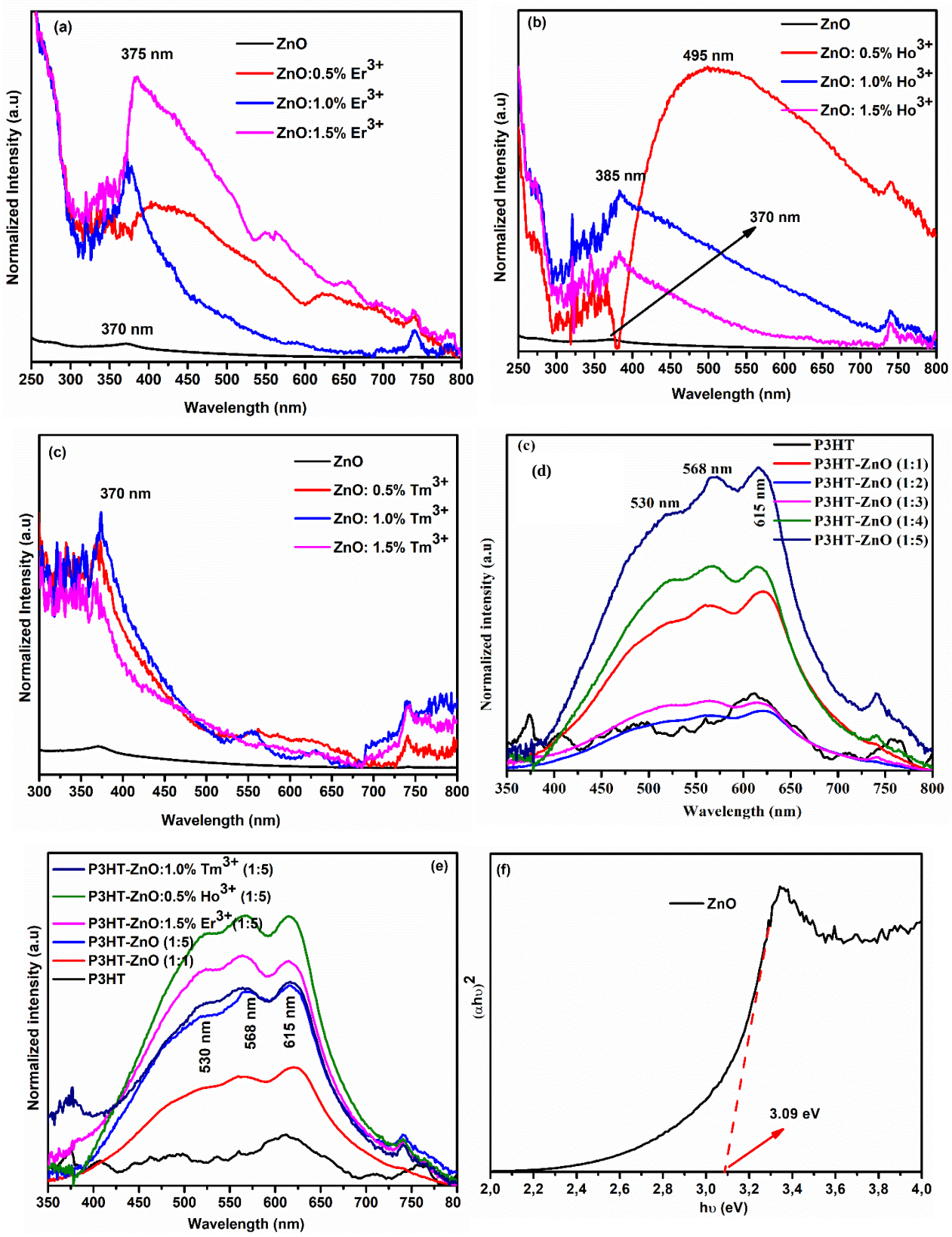

Figure 4. 2: Normalized absorption spectra of (a) Er-doped ZnO, (b) Ho-doped ZnO (c) Tm-doped ZnO (d) P3HT ratios (e) P3HT to doped ZnO at different ratios (f) Tauc's plot of ZnO.

4.3.3 Photoluminescence analysis

Figure 4.3 depicts the PL spectra of ZnO and ZnO doped with rare earth ions. In all spectra of doped ZnO (see Fig. 4. 3(a)-(c)) we observe similar peaks to those of ZnO despite excited with different excitation wavelength. However, an increase and a decrease in intensity is observed with an increase in dopant concentrations. The decrease in intensity is caused by low doping concentration, and thus Er-doping ZnO acts as a nonradiative recombination centre, resulting in a decrease in intensity, whereas the increase in intensity is caused by an increase in doping concentration in the ZnO lattice, which can lead to an increase in the number of luminescent centres, resulting in a higher PL intensity [26, 27]. For example, Er^{3+} doped ZnO exhibits emissions at 418, 441, and 500 nm that are attributable to oxygen (V_o) and Zn (Zn_i) interstitial vacancies, respectively [26]. There are no dopants emission peaks seen due to weak dopants ions emission peaks contained in the signal from a strong, deep-level ZnO emission. These findings are explained by the recombination of photogenerated holes with singly ionized holes charge states of inherent defects such as oxygen vacancies, Zn interstitials, or impurities. [27-30]. In addition, it is observed that the intensity of ZnO doped with rare earth ions increases significantly compared to undoped ZnO, indicating an increase in the oxygen vacancy defects [31] with increased concentration of impurities.

The PL measurements in Fig. 4.3 (d) were taken to observe the charge transfer between the donar-acceptor pair. The emission spectra were compared to the emission spectra of P3HT. Peaks at 636 and 690 nm are seen in P3HT and P3HT-ZnO (1:1), matching to pure electronic transmission in pure P3HT [32]. The emission intensity of P3HT-ZnO (1:1), (1:2), and (1:3) increases. P3HT-ZnO (1:1) and (1:2) ratios had the same spectrum as P3HT alone, indicating no charge transfer from P3HT to ZnO. P3HT-ZnO (1:5) was the best because it demonstrated considerable PL intensity quenching, suggesting charge transfer between donor-acceptor (P3HT-ZnO) materials. However, if the P3HT-ZnO ratio is 1:5, P3HT-ZnO: 1.5% Er^{3+}, P3HT-ZnO: 0.5% Ho^{3+}, and P3HT-ZnO:1.0% Tm^{3+}, the spectra indicate a blue shift from the primary P3HT emission, which is attributable to a change in P3HT crystallographic order [33]. P3HT-ZnO:0.5% Ho^{3+} (1:5) reduces P3HT emissions, which is advantageous for photovoltaic solar cells. P3HT-ZnO:0.5% Ho^{3+} (1:5) reduces P3HT emissions, which is advantageous for photovoltaic solar cells; this is possibly due to the occurrence of more quenching centers within the polymer resulting from holmium doping [34]. However more research needs to be done on this process. Furthermore, there are two types of PL quenching phenomena that may occur in polymers; the static and dynamic quenching [35, 36]. In the process of static quenching, a non-

fluorescent complex form between a fluorophore (P3HT) and a quencher (ZnO:0.5% Ho^{3+}). The reduction in PL intensity suggests full charge transfer between the donor-acceptor materials and, as a result, a reduction in charge recombination. Commission International de l'Eclairage (CIE) 1931 x-y chromaticity diagram of ZnO doped with Er^{3+}, Ho^{3+}, Tm^{3+} nanorods are presented in Fig. 4.3 (f). As shown in Fig. 4. 3 (f), the CIE coordinates lie in different regions with Er^{3+} and Tm^{3+} doped ZnO in the green area and ZnO: Ho^{3+} in the red area. These results show that ZnO can emit in different regions. It is well known that by altering factors like morphology and dopants, the visible luminescence of ZnO may be controlled in a wide range from red to blue [37]. The results agreed with that of PL where ZnO: Er^{3+} emits in the green region and ZnO: Ho^{3+} in the red region.

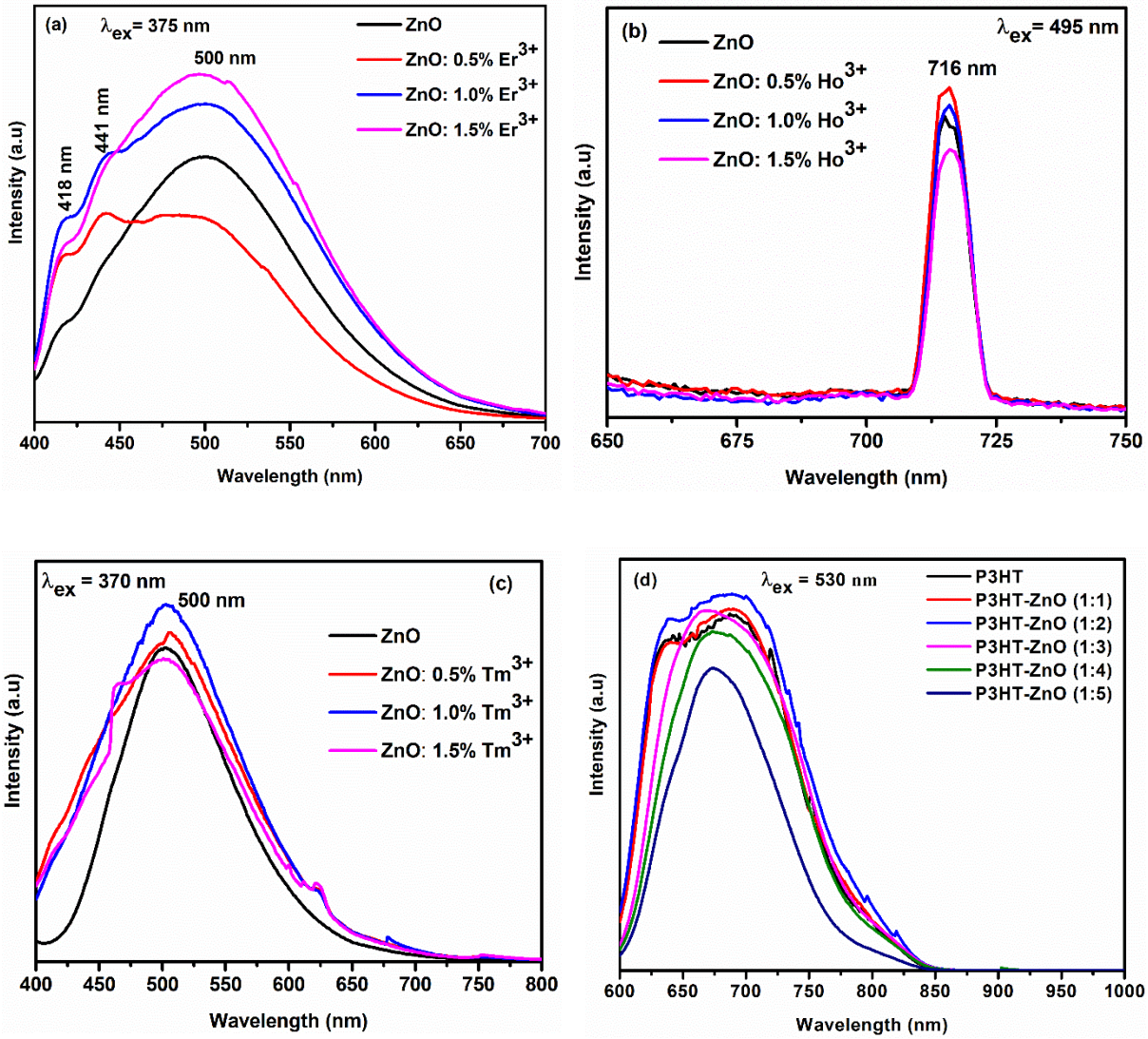

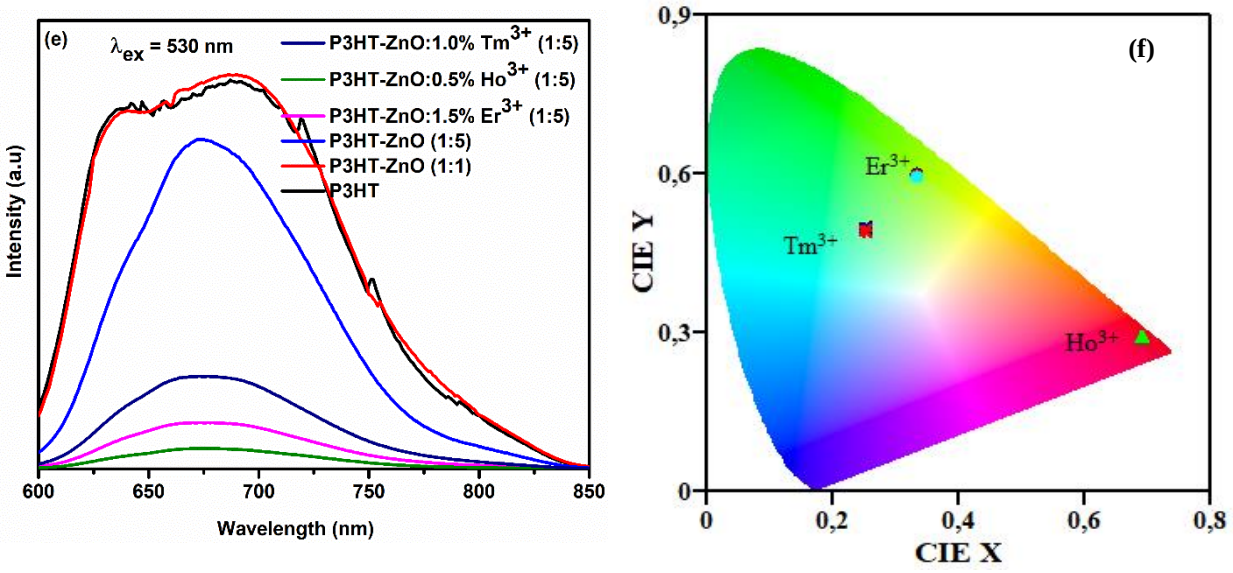

Figure 4. 3: Emission spectra (a) Er-doped ZnO, (b) Ho-doped ZnO (c) Tm-doped ZnO (d) P3HT ratios (e) P3HT to doped ZnO at different ratios (f) CIE chromaticity diagram.

4.3.4 Morphological properties

FE-SEM images of ZnO nanorods generated using the microwave-assisted sol-gel technique are shown in Fig. 4.4. Fig. 5.4 (a) shows agglomerated flower-like nanorods. Fig. 4. 4 (b)-(d) shows hexagonal nanorods with a sharp pencil-like tip. These results are consistent with the XRD results in which we formed a hexagonal wurtzite structure. ZnO: 0.5% Ho^{3+} has the longest nanorods which are possible for minimizing recombination, which could improve the organic solar cells efficiency.

Fig. 4.5 shows FE-SEM images of P3HT, P3HT-ZnO, P3HT-ZnO: 1.5% Er^{3+}, P3HT-ZnO: 0.5% Ho^{3+} and P3HT-ZnO: 1.0% Tm^{3+} in a ratio of 1: 5. Fig. 4.5 (a) shows an image of organic P3HT. Fig. 4.5 (b)-(d) shows a good mixing of composite that propose to improve the efficiency of photovoltaic devices. This might be due to nanorods capacity to minimize recombination, resulting in quicker electron transmission [38]. The role of the capping agent (TG) in the samples was to minimize agglomeration of the hexagonal nanorods. This finding is compatible with the UV/VIS/NIR results, where P3HT-ZnO: 0.5% Ho^{3+} increases absorbance, and the PL results, where P3HT-ZnO: 0.5% Ho^{3+} suppresses P3HT-PL intensity, resulting in complete charge transfer between the donors-acceptor materials and therefore minimizing charge recombination.

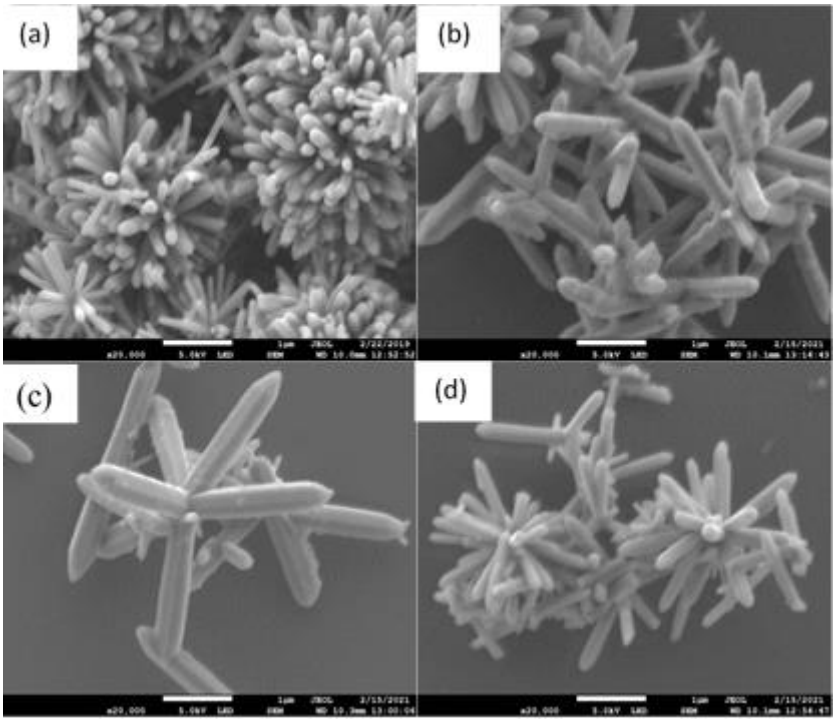

Figure 4. 4: FE-SEM images of (a) ZnO (b) ZnO:1.5% Er^{3+} (c) ZnO:0.5% Ho^{3+} (d) ZnO:1.0% Tm^{3+}.

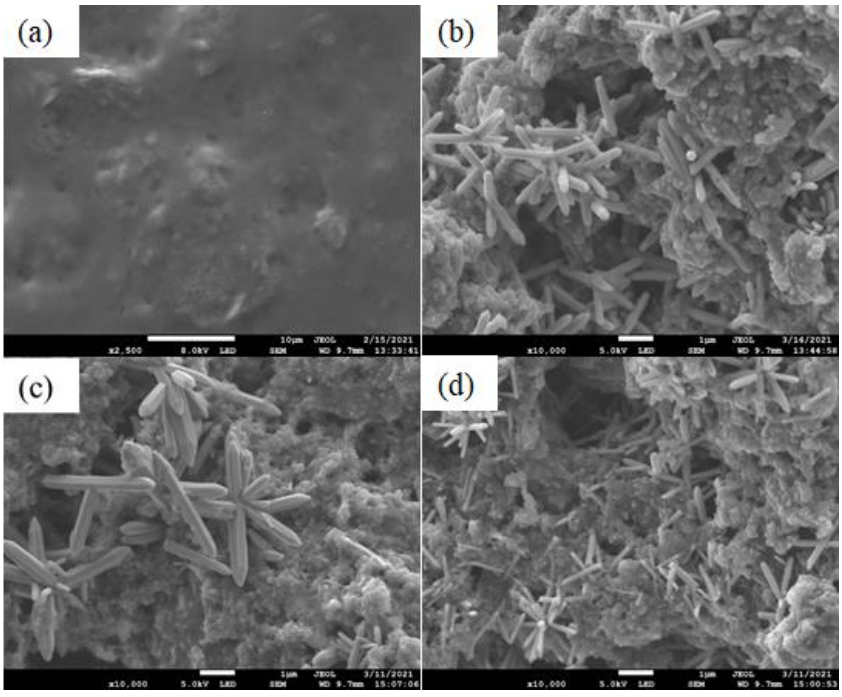

Figure 4. 5: FE-SEM images of (a) P3HT (b) P3HT-ZnO:1.5% Er^{3+} (c) P3HT-ZnO:0.5% Ho^{3+} (d) P3HT-ZnO:1.0% Tm^{3+}.

4.3.5 FTIR analysis

The FTIR spectra for ZnO, P3HT, P3HT-ZnO: 1.5% Er^{3+}, P3HT-ZnO: 0.5% Ho^{3+}, and P3HT-ZnO: 1.0% Tm^{3+} when the ratio is 1:5 are shown in Fig. 4.6. The large absorption peak at 3325

cm^{-1} is caused by O-H vibrations, whereas the bands at around 2971 and 2889 cm^{-1} are caused by C-H stretching. The band at 1380 cm^{-1} is caused by the presence of CO_2 in the air, whereas the bands at 1084 and 1043 cm^{-1} are caused by the asymmetric and symmetric C=O stretching modes, respectively. Inorganic ZnO is represented by the bands below 600 cm^{-1}. Furthermore, the P3HT peaks are still evident, and the variation in strength is attributable to the π-π interactions between P3HT and undoped and doped ZnO [39]. P3HT has strong interactions with doped ZnO, resulting in a nice combination of ligands, which is why we saw nanorods developing from P3HT in FE-SEM.

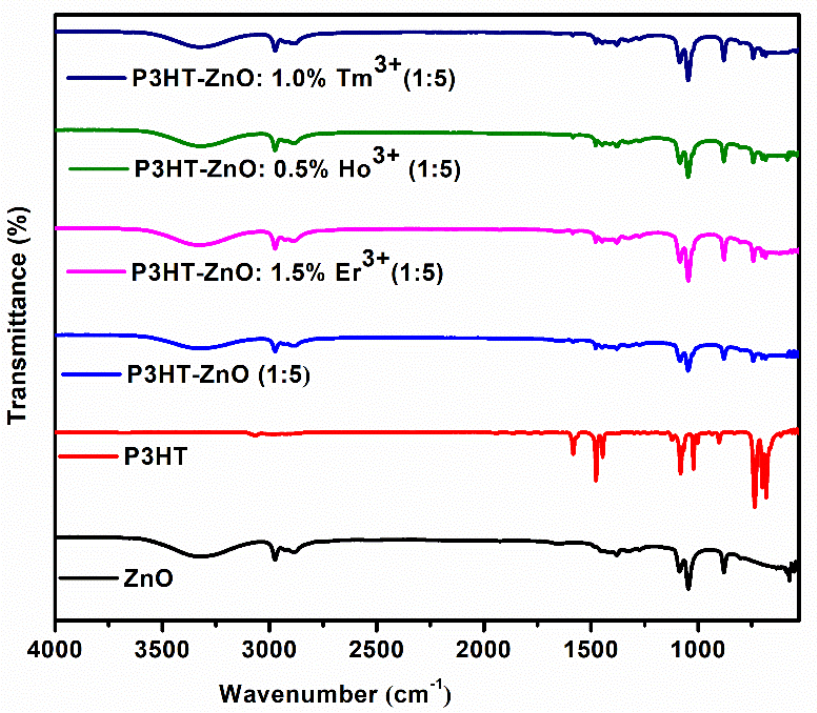

Figure 4. 6: FTIR spectra of ZnO, P3HT, P3HT-ZnO, P3HT-ZnO:1.5% Er^{3+}, P3HT-ZnO:0.5% Ho^{3+} and P3HT-ZnO:1.0% Tm^{3+}.

4.3.6 Electrical properties

The current-voltage (I-V) characterisation of P3HT combined with undoped and doped ZnO is presented in Fig. 4.7, which depicts the rectification behaviour. This behaviour improves when P3HT is added to the doped ZnO. When comparing P3HT to other samples, doping improves the conductivity of P3HT, with P3HT-ZnO: 0.5% Ho^{3+} being the best. This behaviour is known to improve electron transport properties, which can help improve photovoltaic efficiency. The rise in conductivity can be linked to an increase in dopant concentration. Colak et al. [40] synthesized Ho-doped ZnO by spin coating sol–gel and hydrothermal method. They observed an increase in conductivity with Ho^{3+} ion doping. According to Colak et al. [40] the reason for

the increased conductivity is that the dopants have the ionic radii that are larger than that of ZnO and therefore dopants act as a donor. With all the information it is now clear why P3HT-ZnO: 0.5% Ho^{3+} has the highest conductivity. It can be clearly seen that the increase in the conductivity range according to the ionic radii of the impurities being larger than of the ZnO lattice (0.74 Å) (0.88, 0,90 and 0.87 Å for Er, Ho and Tm). In addition, it was concluded that the impurities occupy the interstitial sites of Zn^{2+} and that the number of free electrons in ZnO increases with the amount of impurities.

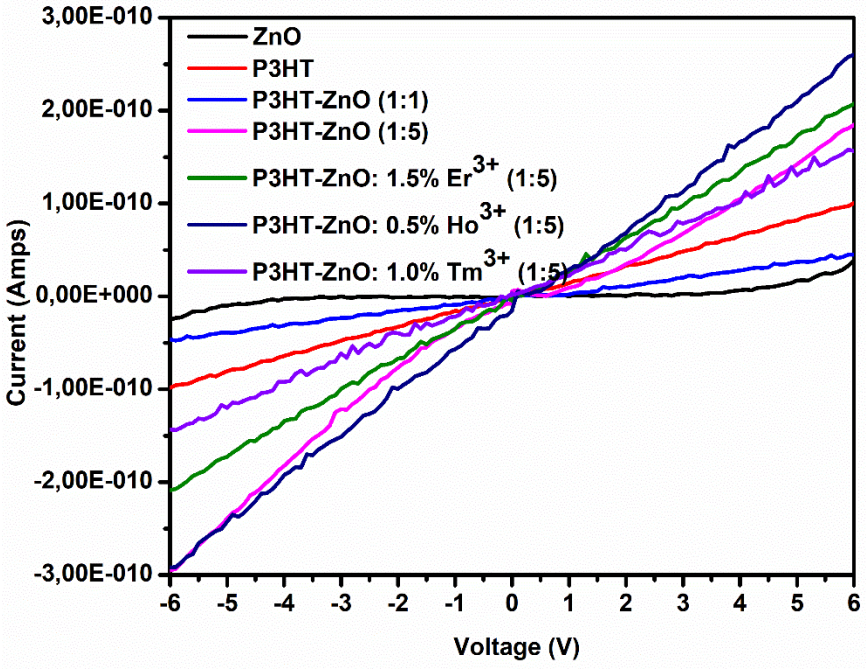

Figure 4. 7: The I-V characteristic spectra of ZnO, P3HT, P3HT-ZnO, P3HT-ZnO:1.5% Er^{3+}, P3HT-ZnO:0.5% Ho^{3+} and P3HT-ZnO:1.0% Tm^{3+}.

4.5 Conclusion

We have successfully synthesized samples prepared using the microwave-assisted sol-gel method. XRD confirmed that no peak other than ZnO was observed. UV/VIS/NIR showed an improved absorption. The incorporation of P3HT samples also showed a strong improvement in absorption, which may lead to an increase in the efficiency of photovoltaic solar cells. P3HT-ZnO: 0.5% Ho^{3+} demonstrated full charge transfer between donor-acceptor material. FE-SEM revealed hexagonal flower-like nanorods, FTIR revealed all functional groups, and electrical characterization revealed that P3HT-ZnO: 0.5% Ho^{3+} has the ability to increased conductivity, which is known to boost solar cell efficiency.

References

[1] V. A. Coleman, C. Jagadish, Properties and Applications 1st ed; Elsivier Science 2006.

[2] Y. S. Park, C. W. Litton, T. C. Collins, D. C. Reynolds, *Phy. Rev.* **43** (1966) 512–519.

[3] V. Kumar, O. M. Ntwaeaborwa, T. Soga, V. Dutta, H. .C Swart, *ACS Photonics*, **4** (2017) 2613–2637.

[4] S. A. M. Lima, M. R. Davolos, C. Legnani, W. G Quirino, M. Cremona, *J. Alloy Compd.* **418** (2006) 35.

[5] E. Rita, E. Alves, U. Wahl, J. G. Correia, A. J. Neves, M. J. Soares, T. Monteiro, *Physica B,* **235** (2006) 340–342.

[6] Y. X. Liu, C. F. Xu, Q. B. Yang, *J. Appl. Phys.* **241** (2009) 084701.

[7] X. H. Zhang, J. Chen, Y. Wu, Z. Xie, J. Kang, L. Zheng, *Physicochem. Eng.Aspects,* **384** (2011) 580–584.

[8] V. Kumar, O. M. Ntwaeaborwa, J. Holsa, D. E. Motaung, H. C. Swart, *Opt. Mater.,* **46** (2015) 510–516.

[9] S. D. Senol, *J Mater Sci: Mater Electron,* **27** (2016) 7767–7775.

[10] K. Fabitha, M. S. Ramachandra Rao, *J.Opt. Soc. Am. B,* **34** (2017) 2485–2492.

[11] H. Çolak, E. Karakose, *J.Rare Earths,* **36** (2018) 1067–1073.

[12] M. Ikrama, R. Murray, A. Hussainc, S. Ali, S. I. Shaha, *Mater, Sci. Eng. B,* **189** (2014) 64–69.

[13] J. J. R. Arias, M. F. V. Marques, *React. Funct. Polym*, **113** (2017) 58–69.

[14] H. Shirakawa, E. J. Louis, A. G. MacDiarmid, C. K. Chiang and A. J. Heeger, *J. Chem. Soc., Chem. Commun.* **16** (1977) 578.

[15] C. W. Tang 1986 *Appl. Phys. Lett.* **48** 183–5.

[16] M. A. Green, K. Emery, Y. Hishikawa, W. Warta, E. D. Dunlop, D. H. Levi and A. W. Y. Ho-Baillie, *Prog. Photovolt., Res. Appl.* **25 (**2017) 3–13.

[17] A. Hubler, B. Trnovec, T. Zillger, M. Ali, N. Wetzold, M. Mingebach, A. Wagenpfahl, C. Deibel and V. Dyakonov, *Adv. Energy Mater.* **1 (**2011) 1018–1022.

[18] F. C. Krebs, M. Hosel, M. Corazza, B. Roth, M. V. Madsen, S. A. Gevorgyan, R. R. Sondergaard, D. Karg and M. Jorgensen, *Energy Technol.* **1 (**2013) 378–81.

[19] B. D. Cullity (1956) Elements of X-ray Diffraction (2nd Ed), Addison Wesley.

[20] Y. Kumari, L. K. Jangir, A. Kumar, M. Kumar, K. Awasthi, *Solid State Communications, 263 (2017) 1 – 5.*

[21] C. F. Zhe, Handbook of Zinc Oxide and Related Materials, CRC Press, Taylor & Francis, Boca Raton, Fla, USA, 2013.

[22] K. Yu, J. Shi, Z. Zhang, Y. Liang, W. Liu, *J. Nanomater*, (2013) 1 – 5.

[23] W. Shen, J. Tang, R. Yang, H. Cong, X. Bao, Y. Wang, X. Wang, Z. Huang, J. Liu, L. Huang, J. Jiao, Q. Xu, W. Chen, L. A. Belfiore, *RSC Adv*, **4** (2014) 4379 – 4386.

[24] T. Huiling, L. Xian, J. Yadong, X. Guangzhong, D. Xiaosong, *Sensors*, **15** (2015) 2086 – 2103.

[25] H. Oh, J. Krantz, I. Litzov, T. Stubhan, L. Pinna, C. J. Brabec, *Sol Energy Mater Sol Cells*., **95** (2011) 2194 – 2199

[26] Y. S. No, T. W. Kim, *J. Ceram. Process. Res.*, **14** (2013) 396.

[27] U. Ozgour, Y. I. Alivov, C. Liu et al., *J. Appl. Phys*, **98** (2005) 103.

[28] D. C. Look, *Mater. Sci. Eng., B*, **80** (2001) 383–387.

[29] T. Parvin, N. Keerthiraj, I. A. Ibrahim, S. Phanichphant, and K. Byrappa, *Int. J. Photoenergy*, **2012** (2012) 8.

[30] W. Shen, J. Tang, R. Yang, H. Cong, X. Bao, Y. Wang, X. Wang, Z. Huang, J. Liu, L. Huang, J. Jiao, Q. Xu, W. Chen, L. A. Belfiore, *RSC Adv*, **4** (2014) 4379–4386.

[31] A. Hastir, N. Kohli, R. C. Singh, *J. Phys. Chem. Sol*, **105** (2017) 23–34.

[32] R. Al-Gaashani, S. Radiman, A. R. Daud, N. Tabet, Y. Al-Douri, *Ceram. Int* **39** (2013)2283–2292.

[33] G. L. Kabongo, P. S. Mbule, G. H. Mhlongo, B. M. Mothudi, K. T. Hillie, M. S. Dhlamini, *Nanoscale Res. Lett.*, **11** (2016) 1–11.

[34] Y. Wang, D. Kurunthu, G. W. Scott, C. J Bardeen, *J Phys Chem C*, **114** (2010) 4153–4159.

[35] Lakowicz JR (1999) Principles of fluorescence spectroscopy, 2nd edn. Springer, Kluwer, New York.

[36] K. Kumari, U. Kumar, S. N. Sharma et al, *J Phys D Appl Phys*, **41** (2008) 1-9.

[37] R. K. Kalaiezhily, G. Saravanan, V. Asvini, N. Vijayan, K. Ravichandran, *Ceram. Int*, **44** (2018) 19560–19569.

[38] A. H. Yuwono, A. Sholehah, S. Harjanto, D. Dhaneswara, F. Maulidiah, *Adv. Mater. Res*, **789** (2013) 132–137.

[39] Bhatia R, Kumar L, *J. Saudi Chem. Soc*, **21** (2017) 366–376.

[40] H. Colak, E. Karakose, *JOM*, **73** (2021) 395–403.

Chapter 5

Microwave-assisted sol-gel synthesis of P3HT-ZnO: Sm^{3+}, Yb^{3+}: Study of structure, morphology, optical and electrical conductivity for possible application in organic solar cells

The chapter discusses microwave-assisted sol-gel synthesis of P3HT-ZnO: Sm^{3+}, Yb^{3+}: Study of structure, morphology, optical and electrical conductivity for possible application in organic solar cells. (Article published in the Materials Chemistry and Physics Journal)

5.1. Introduction

Zinc oxide (ZnO) has piqued the curiosity of many scientists for decades due to its unusual physical and chemical characteristics and significant promise in nano-device development [1 - 2]. Among metal oxides, ZnO is one of the most appealing semiconductor materials due to its wide band gap of 3.27 eV [8] and suitability as a host for the 4f energy levels of rare earth (RE) ions [9]. It may be used in photodetectors [3, 4], sensors [5, 6] and solar cells [7, 8]. In addition, aggregation of chemically generated nanoscale ZnO owing to high surface energy might result in excessive grain size and hence impact stability [10]. By incorporating of capping agents lowers the size of the nanoparticles, which improves their stability [10].

Several studies have investigated the optical characteristics of doped and undoped ZnO. Faraz et al. [12] previously synthesized samarium (Sm) doped ZnO using sol-gel-combustion and studied its optical properties using UV-vis, they reported an enhanced optical absorption, implying that rare earth ion doping is advantageous for effective photocatalysts and/or photovoltaics to convert solar energy into electricity. Kumar and his team [12] used the green solution combustion approach to optimize ZnO: Sm^{3+} (1 - 6 mol%) and the highest PL emission was recorded at a dopant concentration of 3 mol%. The highest PL emission is due to the extremely thin space layer and the excessive diffusion depth of light into host space charge layer, and therefore the recombination of photogenerated e-h pair become less complicated.

Gorokhova et al. [13] fabricated ZnO: Yb^{3+} from commercial reagent grade ZnO and Yb_2O_3 powders by hot pressing in vacuum at the temperature 1180 ℃ and observed a variation in PL intensity. The rise in intensity is attributed to an increase in the concentration of oxide vacancies after high-temperature deformation during uniaxial hot pressing in vacuum [13]. It has been commonly observed that high-pressure exposure can result in a large concentration of vacancies in ZnO [13]. When Yb^{3+} ions are added to ZnO, the intensity decreases due to oxide defects. Their findings are consistent with what was reported by Kabongo et al [14], where they attribute an increase and decrease in PL intensity to possible energy transfer from Yb^{3+} ions to ZnO or defects attributed oxygen reduction. Synthetic approaches, on the other hand, are crucial in examining the structure, morphology, and distinctive optical characteristics of metal oxides. Among many synthesis methods, microwave-assisted synthesis has attracted a lot of interest due to the fact that it is faster, simpler, and more energy efficient [15]. This approach helps to control the shape and size of nanomaterials and it is also simple and affordable to implement. As a result, ZnO nanorods were synthesised in this study using a simple microwave-assisted sol-gel process, and 1-thioglycerol (TG) was added as a capping agent to regulate particle size and prevent agglomeration. Satpathy et al. [16] used a straightforward chemical method to create Gd-doped ZnO nanorods with varying doping concentratios. When they increased the concentration of dopants, they noticed an increase in rod-like shape. An increase in rod-like morphology, according to Satpathy et al. [16], implies an improvement in stronger magnetism. Satpathy et al. [17] used a simple chemical technique to create pure and La-doped ZnO nanorods in another investigation. They discovered that adding La dopant had no influence on the crystal structure of the ZnO nanorods. They also indicated that the produced ZnO nanorods will be beneficial in multifunctional devices such as optoelectronics, spintronics, and biomedical applications. As capping molecules, TG with sulphydryl and carboxyl groups are frequently utilized [18]. The sulphydryl group can coordinate with the nanoparticles, whereas the carboxyl group leads to colloidal nanoparticle electrostatic stability [18]. Poly(3-hexylthiophene) (P3HT) is a well-known polymer that is utilized in electrical devices such as organic solar cells [10]. Conjugated electron donor polymer P3HT is widely employed in solar cells because of its exceptional electro-optical characteristics and ease of processing and device fabrication [20-24].

In this study, ZnO was optimized by varying the TG concentration, and the results shows that ZnO with a TG molar concentration of 0.2 had maximum PL emission and will thus be used as the host material. The main objective was to introduce a dopant (Sm^{3+} and Yb^{3+}) into our

host and then add it into P3HT, and the investigate its crystal structure, morphology, optical and electrical conductivity. Sm^{3+} is commonly known as one of the most active luminescent ions, with a bright red-orange fluorescence in the visible range [25]. Lot of investigations on Yb^{3+} as a sensitizer have been carried out, for example, Er^{3+}/Yb^{3+} co-doped lead phosphate produced by melt quenching process [26] displayed energy transfer from Yb^{3+} to Er^{3+}. As a result, Yb^{3+} ion will be used as a sensitizer in order to boost the Sm^{3+} ion's absorption power. To the best of our knowledge, no comprehensive study has been conducted employing this combination to explicitly boost electron transport and improve electrical conductivity for prospective application in organic solar cells as illustrated in Fig. 5.1. Furthermore, these materials combination exhibits a significant photoluminescence quenching effect, indicating the feasibility of charge separation in the photoactive layer of an organic solar cell devices.

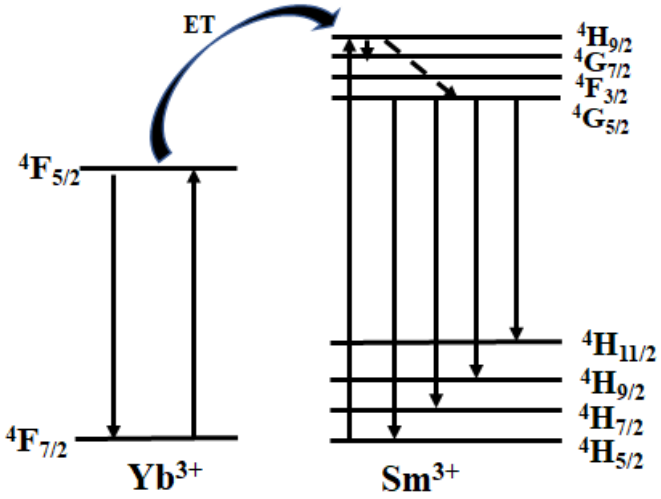

Figure 5. 1: Electronic energy level diagram of Yb^{3+} and Sm^{3+}: a photon excited state absorption process of Sm^{3+} with Yb^{3+} as the sensitizer in Sm/Yb doped ZnO. Full, curved, and dashed arrows indicate radiative and non-radiative energy transfer and multiphonon relaxation processes, respectively [26].

5.2. Experimental section

5.2.1 Materials

Zinc acetate dihydrate ($Zn(CH_3COO)_2{\cdot}2H_2O$; 99.5%), 1-thioglycerol (≥97.0%), sodium hydroxide (NaOH, 97%), samarium (iii) acetate hydrate ($Sm(CH_3CO_2)_3{\cdot}H_2O$, 99.9%), ytterbium (iii) acetate hydrate ($Yb(CH_3CO_2)_3{\cdot}H_2O$, 99.9%), regioregular Poly(3-hexylthiophene-2,5-diyl) ($(C_{10}H_{14}S)n$, M_w = 20000), chlorobenzene (anhydrous, 99.8%), ethanol (anhydrous, 96.0%) and borosilicate glass substrate were all purchased from Sigma-Aldrich (South Africa) and used without any further purification.

5.2.2 Microwave-assisted sol-gel synthesis

The hexagonally shaped ZnO nanorods were prepared by dissolving 2.5 g of zinc acetate dihydrate into 100 ml deionized water, adding 1-thioglycerol (TG) as a capping agent at 0.2, 0.4, 0.6, 0.8, and 1.0 molar concentrations and un-capped ZnO. The solution was stirred for 15 minutes on a magnetic stirrer. The presence of TG in the solution was used to regulate the distribution of particle size and to avoid agglomeration. In contrast, 4 g of sodium hydroxide (NaOH; 97%) was dissolved into 30 ml of deionised water while stirring the solution for 15 minutes. The sodium hydroxide solution was added dropwise into the zinc solution. The resulting white solution was swirled at room temperature for 1 hour with a magnetic stirrer. From our analysis, ZnO capped with 0.2 molar concentration displayed optimum results and will be used as the host material henceforth. The same procedure of doping ZnO with Sm^{3+} and Yb^{3+} followed while keeping Sm^{3+} concentration the same and varying Yb^{3+} concentrations. ZnO:Sm^{3+} (1 – 6 mol%) was optimized by Kumar et at [12] and they observed that 3% concentration was the best sample. The mixture was agitated for 1 hour after 0.11 g of Sm^{3+} (3 mol%) and 0.044, 0.126, 0.210, 0.294, and 0.378 g of $Yb3^{+}$ (1, 3, 5, 7, and 9 mol%) ion doping concentration were added. The solution was then placed in a SynthWave maintained at 140 ^{o}C and 1000 W for 5 minutes. The mixture was then centrifuged for 5 minutes at 4000 rpm and rinsed numerous times with deionized water and ethanol to remove acetates. The finished product was disseminated in ethanol to improve particle separation. The results show that ZnO:3%Sm^{3+},5%Yb^{3+} is the best sample and therefore will be incorporated with P3HT, but first P3HT was optimized with ZnO in various ratios (1:1, 1:2, 1:3, 1:4, and 1:5) and P3HT-ZnO (1:5) is the sample that displayed optimum results. When it comes to preparation of P3HT, 10 mg of what P3HT was dissolved in 1 ml chlorobenzene and agitated for 24 hours on a magnetic stirrer. Following direct mixing of P3HT with undoped and doped ZnO, the samples were sonicated for 30 minutes. In order to fabricate the thin films, a pipette was used to drop-cast the solution onto the ultrasonically cleaned borosilicate glass substrate. The films were then left to dry at ambient temperature for 24 hours. Finally, ZnO, P3HT, P3HT:ZnO (1:5), and P3HT:ZnO:3%Sm^{3+},5%Yb^{3+} (1:5) samples were adjusted and tested with UV/VIS/NIR spectrophotometer for possible applications in organic solar cells.

5.2.3 Characterization techniques

Rigaku SmartLab X-Ray diffractometer was used to evaluate the structure and crystallinity of the prepared materials using Cu-Kα radiation source (λ = 0.154059 nm). PerkinElmer FTIR

spectrometer was used for functional group determination. PerkinElmer Lambda 1050 UV/VIS/NIR Spectrophotometer was used to analyse the absorbance. FE-SEM images were recorded on JEOL JSM-7800F coupled with Thermo Scientific Ultradry EDS detector. Photoluminescence (PL) measurements were recorded using a Horiba Fluorolog-3 Jobin Yvon spectrometer at the excitation wavelength of 370, 400 and 530 nm. X-ray photoelectron spectroscopy (XPS) data was obtained from the Thermo ESCAlab 250 Xi spectrometer using Al Kα (1486.7 eV) monochromatic x-ray radiation source and was internally calibrated by carbon deposit C (1s) binding energy (BE) at 284.8 eV. Current-voltage (I–V) measurements were obtained using the Keithley 6487 picoammeter with a voltage source. The measurements were taken with the thin film placed in the dark and at room temperature (303 K).

5.3. Results and discussion

5.3.1 X-ray diffraction analysis

Fig. 5.2 (a – d) show the XRD patterns of uncapped and TG-capped ZnO as the concentration (TG) varies from 0.2 to 1.0 mol%, ZnO, ZnO: 3% Sm^{3+}, ZnO: 3%Sm^{3+}, x%Yb^{3+}, peak shift, P3HT and P3HT-ZnO at different ratios. The diffraction peaks of all samples reveal the structure of wurtzite ZnO, indicating that all samples have a hexagonal structure, as illustrated in Fig. 5.2. (a). In XRD patterns, hexagonal phase diffraction (ICDD card no. 01-074-9940) peaks are clearly evident, with strong peaks at $2\theta = 31.9^{o}$ (100), 34.6^{o} (002), and 36.5^{o} (101) for uncapped and capped ZnO. As the concentration of capping agent increases, the intensity of the diffraction peak decreases. These findings are thought to be the result of inadequate growth as a result of the shortened maturation time or growth inhibition by the capping agent. The mean lattice constants of uncapped and capped ZnO were determined to be a = b = 3.26 and c = 5.22, respectively. These values were similar to ICDD card #01-074-9940. In our synthesis, no secondary phases such as $Zn(OH)_2$ were identified in the XRD findings, confirming the development of a single phase. When compared to uncapped ZnO, ZnO with a capping agent of 0.2_TG demonstrated the maximum intensity, suggesting a significant shift in particle transformation and therefore will be used as the host material henceforth. Mou et al [27] used an aqueous precipitation approach to create CdS capped with TG. They discovered a phase transition from cubic zinc-blende to hexagonal wurtzite. Their discoveries are relevant to the study being discussed and presented at FE-SEM, in which nanoparticles have evolved from nanoflakes to flower-like nanorods.

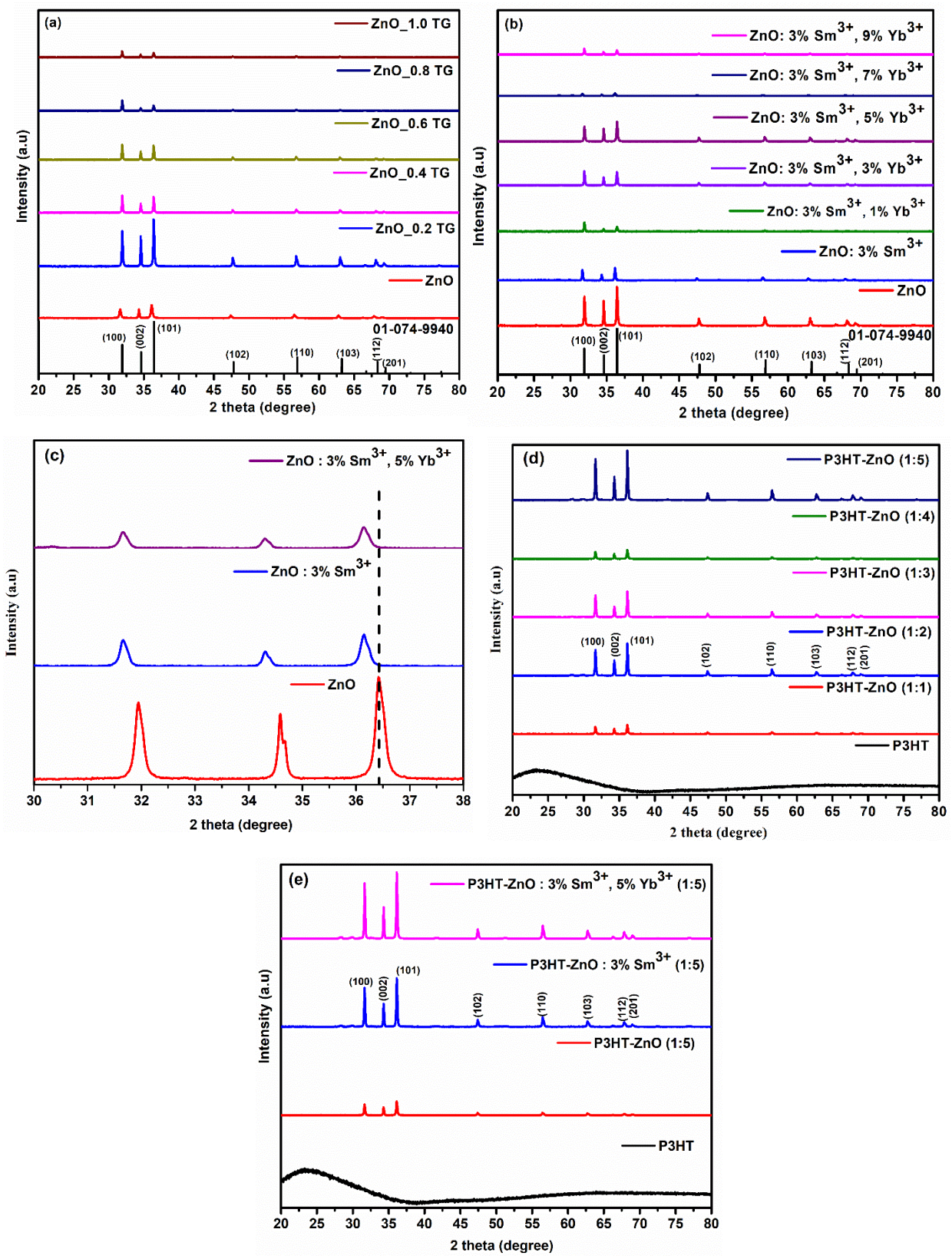

Figure 5. 2: XRD patterns of (a) ZnO and ZnO at different concentrations of TG (b) ZnO, ZnO: 3% Sm^{3+} and ZnO: 3% Sm^{3+}, x% Yb^{3+} (c) peak shift of ZnO, ZnO: 3% Sm^{3+} and ZnO: 3% Sm^{3+}, 5% Yb^{3+}, (d) P3HT, P3HT-ZnO at different ratios, (e) P3HT, P3HT-ZnO (1:5), P3HT-ZnO: 3% Sm^{3+} (1:5) and P3HT-ZnO: 3% Sm^{3+}, 5% Yb^{3+} (1:5).

The diffraction patterns of capped ZnO, ZnO: 3% Sm^{3+}, and ZnO: 3% Sm^{3+}, x% Yb^{3+} (x = 1, 3, 5, 7, and 9%) are shown in Fig. 5.2 (b). Despite the doping, the samples retain a hexagonal wurtzite structure, with a drop in peak intensity. ZnO: 3% Sm^{3+}, 9% Yb^{3+} decreases the strength of the diffraction peak even more. The magnitude of these modifications is determined by the concentration of the dopant atom. According to Aksoy et al. [28], structural deterioration caused by ZnO doping is to be predicted. This is because of impurity substitution at the Zn^{2+} location.

Sm^{3+} doping ZnO and co-doping with Yb^{3+} ions cause the diffraction peaks to shift to lower angles, suggesting successful doping (see Fig. 5.2 (c)). The difference in ionic radii of the cations (Zn^{2+} (0.074 nm), Sm^{3+} (0.096 nm), Yb^{3+} (0.101 nm)) is attributable to the shift, showing that Sm^{3+} and Yb^{3+} replace Zn^{2+} in the host lattice. Carvalho et al. [29] found similar results when they synthesized ZnO: Sm^{3+} using the microwave-assisted hydrothermal technique, and their results revealed that no secondary phase contained Sm^{3+}. The average crystallite size, lattice parameters and cell volume of ZnO, ZnO: Sm^{3+} and ZnO: Sm^{3+}, Yb^{3+} are listed in **Table 5.1.** The average crystallite size of these samples was estimated using the Scherrer equation [30]:

$$D = \frac{k\lambda}{\beta Cos\theta} \tag{5.1}$$

where *D* is the crystallite size (nm), *k* is the Scherrer constant (0.9), λ is the x-ray source's wavelength (0.15406 nm), β (radians) is the full width at half maximum and θ is the peak position in radians. Doping and co-doping, according to this estimation, lower the crystallite size of the samples, resulting in a drop and broadening of the diffraction peak. Tsuji et al. obtained comparable findings with decreasing crystallite size [31] and noticed a reduction in crystallite size after doping with ZnO Sm^{3+} and ascribed it to the development of Zn-O-Sm on the doped material's surface.

Table 5. 1: Crystallite size, lattice constant (a and c), and cell volumes of undoped and doped ZnO.

Sample	Crystallite size (nm)	a (Å)	c (Å)	V (Å^3)
ZnO	35	3.36	5.22	46.899
ZnO: 3% Sm^{3+}	32	3.39	5.27	46.885
ZnO: 3% Sm^{3+}, 5% Yb^{3+}	28	3.30	5.29	46.883

The XRD patterns of doped P3HT-ZnO at different ratios are shown in Fig. 5.2 (e). The results suggest a hexagonal structure with a more crystalline 1:5 intensity. The XRD patterns of P3HT including doped and co-doped ZnO are also shown in Fig. 5.2 (e). The results reveal that the hexagonal structure of wurtzite can still be seen and remains with increasing diffraction peak strength, indicating a well-defined diffraction peak with a high degree of crystallization. These findings are consistent with those of Lee et al. [32], who discovered highly crystalline P3HT/ZnO, indicating efficient charge transfer and better performance of optoelectronic applications.

5.3.2 UV/VIS/NIR-NIR analysis

At room temperature, the absorption spectra of the synthesized samples were examined with a UV/VIS/NIR spectrophotometer in the wavelength ranges of 250-800 nm (for uncapped and capped ZnO at different concentrations of TG, Sm^{3+} doped and Yb^{3+} co-doped ZnO nanorods) and 350-800 nm (for P3HT incorporation into ZnO and doped ZnO nanorods). The normalized absorption spectra of uncapped and capped ZnO at varied TG concentrations (0.2 - 1 mol%) are shown in Fig. 5.3 (a). The spectra indicate an absorption peak at 370 nm for both uncapped and capped ZnO, with the exception of ZnO 0.6 TG, which shows a peak at 375 nm. Band transitions in ZnO are responsible for these absorption peaks. Additional peaks at 500, 564, and 743 nm are detected as the quantity of TG capping agent rises. These extra peaks might be caused by TG absorption, as the higher the concentration, the more difficult it is to eliminate TG from the sample. The absorption spectra for co-doped ZnO are shown in Fig. 5.3 (b). These findings demonstrate an improvement in absorption when the Yb^{3+} concentration varies from 1 to 9 mol% while the Sm^{3+} concentration is held at 3 mol. The greatest absorption intensity of ZnO: 3% Sm^{3+}, 5% Yb^{3+} is centered at 385 nm. Because of the wide particle size distribution in colloidal solution, the exciton transition is less prominent in co-doped samples. Unni et al.

[33] reported peak widening in the UV/VIS/NIR spectra of a mixed Au/CdS system with TG capping, which resulted in a red shift due to the increased permittivity of the surrounding medium. Their findings are congruent with the findings of this investigation. Doping ZnO with rare earth ions has been shown to increase its optical characteristics and conductivity [34], thus improved conductivity is predicted here. Figures 5.3 (c) and (d) show the absorption spectra of P3HT incorporation into ZnO at various ratios, as well as P3HT incorporation into doped and co-doped ZnO. The results demonstrate that P3HT-ZnO (1:5) and P3HT-ZnO: 3% Sm^{3+}, 5% Yb^{3+} (1:5) have the highest intensity absorption spectra. Better absorption leads to improved photovoltaic solar cell efficiency via photon absorption [35]. The spectra demonstrate that the sample possesses the same vibronic modes as the excited-state electron absorption peaks centered at 530, 568, and 615 nm, which are ascribed to the transitions π–π* P3HT [36]. The optical bandgap was calculated using the linear section of the Tauc's plot [37]:

$$\alpha hv = A(hv\text{-}Eg)^{1/2} \qquad (2)$$

Where A is the constant, hv is the photon energy (h=Plank's constant and v is frequency of a photon) and a is the absorption coefficient. Extrapolating from the linear section of Tauc's plot ($(ahv)^2$ vs hv) the predicted bandgap values are shown in Fig. 5.3 (e) and (f). The band gap for uncapped and capped ZnO was around 3.14 eV and approximately 3.07 eV, respectively. The band gap of ZnO, Sm^{3+} doped ZnO, and Yb^{3+} co-doped ZnO spans from 3.07 to 2 eV, with a red shift detected. This discovery might be attributed to the fact that TG and impurities form a new electron level in the ZnO band gap, and the presence of oxygen defects changes the band gap.

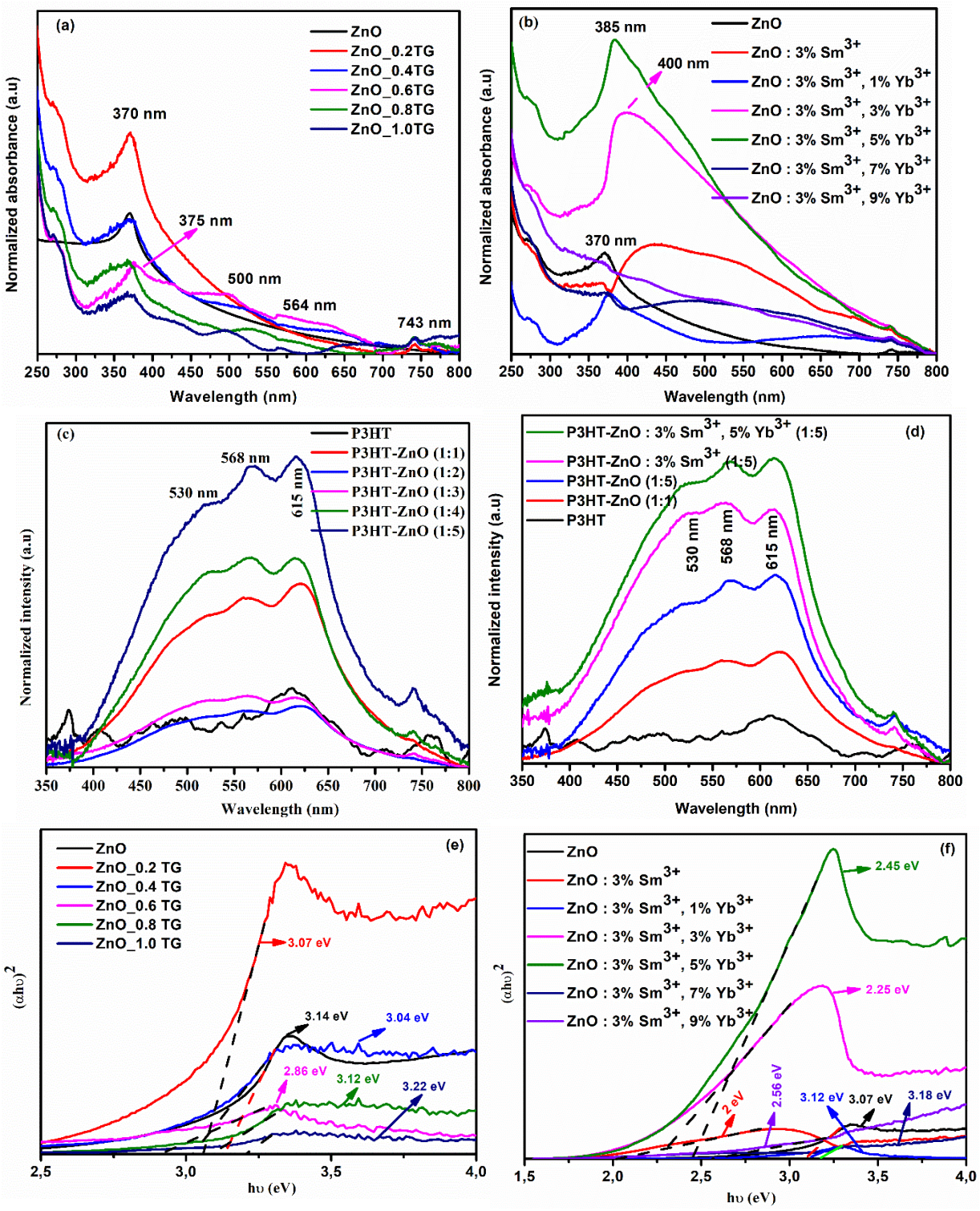

Figure 5. 3: Normalized absorption spectra of (a) uncapped ZnO and capped ZnO at different concentration of TG, (b) Sm^{3+}doped and Yb^{3+}co-doped ZnO nanorods, (c) the incorporation of P3HT into ZnO nanorods (d) the incorporation of P3HT into ZnO nanorods doped with 3% Sm^{3+} and 5% Yb^{3+}, (e) the Tauc's plot of uncapped and capped ZnO at different concentration of TG and (f) Sm^{3+}doped and Yb^{3+}co-doped ZnO nanorods.

5.3.3 PL analysis

Fig. 5.4 (a) shows the photoluminescence spectra of ZnO (inset) and ZnO at various TG concentrations (0.2 - 1 mol%) were recorded at room temperature in the wavelength range 400 - 800 nm with an excitation wavelength of 370 nm. Uncapped ZnO samples displayed two emission peaks at 510 and 624 nm, while capped ZnO samples showed peaks at 494 and 500 nm. These emission peaks have been attributed to oxygen vacancies (Vo) and zinc interstitials (Zni) [38].

The emission spectra of Sm-doped ZnO PL stimulated at 400 nm are shown in Fig. 5.4 (b). The spectra indicate emission peaks at several locations between 400 and 600 nm. The luminescence defect state in ZnO is responsible for all emission peaks [39]. As a result of these flaws, no emission corresponding to transitions inside the f-f Sm^{3+} ions were seen. However, because the quantity of Yb^{3+} changes, the greatest emission of ZnO sample 3% Sm^{3+}, 5% Yb^{3+} was observed. Furthermore, the location of the PL emission peak indicates a decrease in particle size, which is compatible with the anticipated band and size reduction crystallites. Thiols, because of their capacity to behave as hole traps, limit the radiative recombination of excited carriers [34]. At room temperature, the PL measurements in Fig. 5.4 (c) and (d) were taken in the wavelength range 600-1000 nm with an excitation wavelength of 530 nm. The charge transfer between the donor-acceptor pair (P3HT:ZnO) was observed, and the emission spectra were compared to that of P3HT alone. Peaks in P3HT emission were seen at 636 and 690 nm, which corresponded to the electronic transition or pure P3HT [40]. The emission intensity of P3HT-ZnO (1:1) and (1:2) increases. Both ratios have the same P3HT spectrum, which shows no charge transfer from P3HT to ZnO. The best combination was P3HT-ZnO (1:5), which demonstrated considerable PL intensity quenching, suggesting charge transfer between donor-acceptor (P3HT-ZnO) materials. The emission spectra exhibited a minor blue shift, which was attributed to a change in P3HT [41]. P3HT-ZnO: 3% Sm^{3+}, 5% Yb^{3+} (1:5) effectively inhibits P3HT emission, which is known to benefit improved carrier mobility, free carrier dispersion path lengthening, and phonon activity in organic solar cells. A drop in PL intensity suggests charge transfer between donor-acceptor materials and, as a result, a reduction in charge recombination. Furthermore, ZnO has a low exciton binding energy and a lower conduction band than P3HT lowest unoccupied molecular orbitals (LUMO), which enables electron charge transfer from departed P3HT to ZnO nanorods [42].

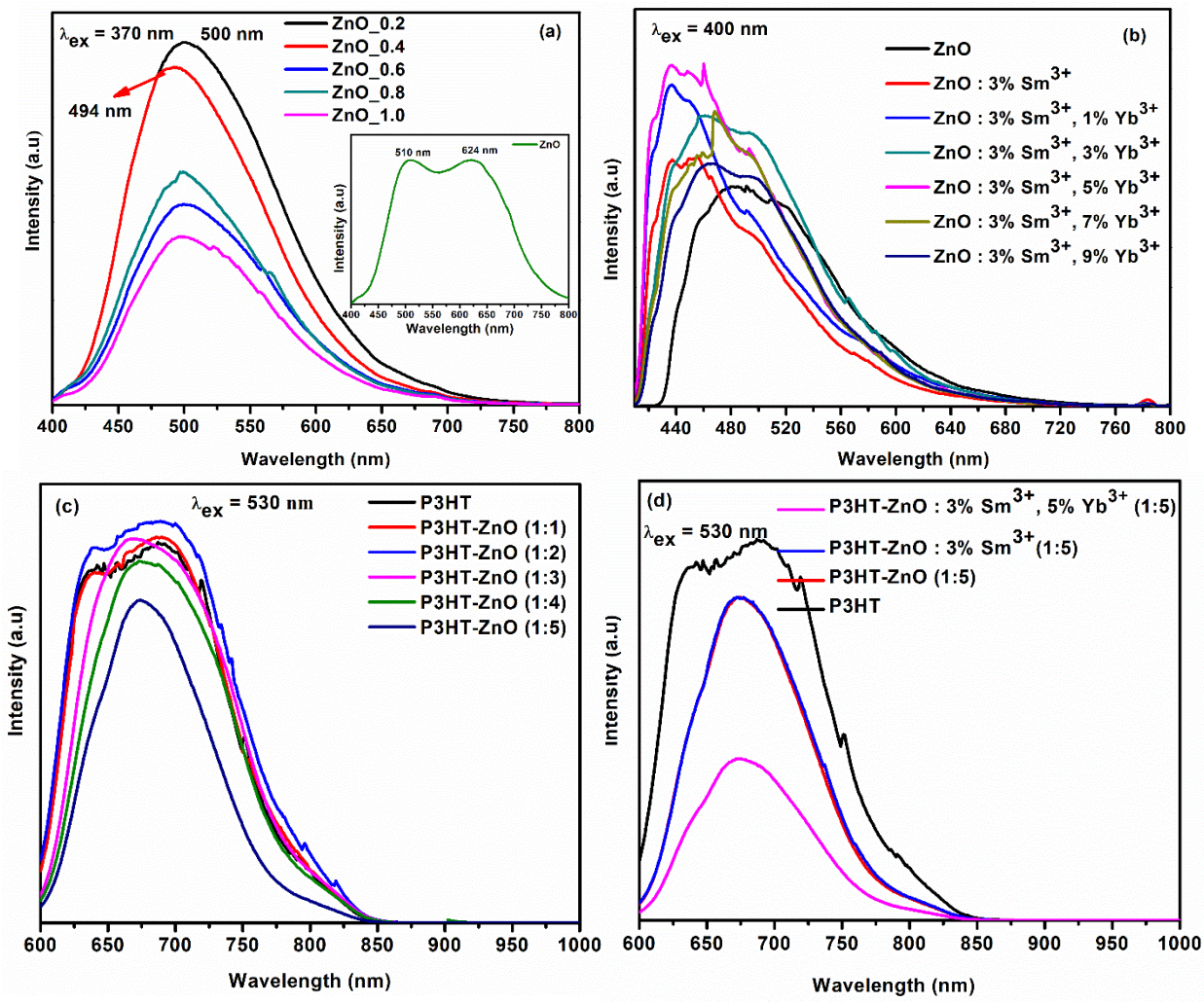

Figure 5. 4: Emission spectra of (a) ZnO at various TG concentrations with an inset of pure ZnO excited at 370 nm, (b) Sm^{3+} and Yb^{3+} doped ZnO excited at 400 nm, (c) P3HT-ZnO different ratios, and (d) P3HT, P3HT-ZnO (1:5), P3HT-ZnO:3% Sm^{3+} (1:5), (1:5).

5.3.4 FE-SEM analysis

Field emission scanning electron microscopy was used to investigate the morphology of the materials in this investigation (FE-SEM). Figure 5.5 (a) depicts a FE-SEM picture of uncapped ZnO with nanoflake development, whereas Figure 5.5 (b) depicts capped ZnO at 0.2 TG with flower-like nanorods (b). Figure 5.5 (c) shows the formation of pencil-like hexagonal nanorods, indicating that we have really synthesized hexagonal nanorods, which fits with the hexagonal structure of the XRD data. Figure 5(d) depicts the shape of organic P3HT. Fig. 5.5 (e) and (f) show FE-SEM images of P3HT-ZnO (1:5) and P3HT-ZnO: 3% Sm^{3+}, 5% Yb^{3+} (1:5). FE-SEM images in Fig. 5.5 (e) showed a well-mixed nanorods structure with P3HT. In Fig. 5.5 (e), FE-SEM images revealed a well-mixed nanorods structure with P3HT. This mixture's homogeneity can aid enhance photon absorption in organic solar cell devices, increasing performance.

Because every capped ZnO has hexagonal nanorods, the involvement of TG in the samples is obvious. When it comes to improving device performance, ZnO nanorods are often preferred over spherical nanoparticles because they leads to quicker electron transfer and/or increased charge carrier mobility [43]. The capacity of nanorods to minimize electron-hole recombination enhances the efficiency of organic solar cells [44,45]. Furthermore, as a transport layer in organic solar cells, ZnO nanorods are the most promising choice [46].

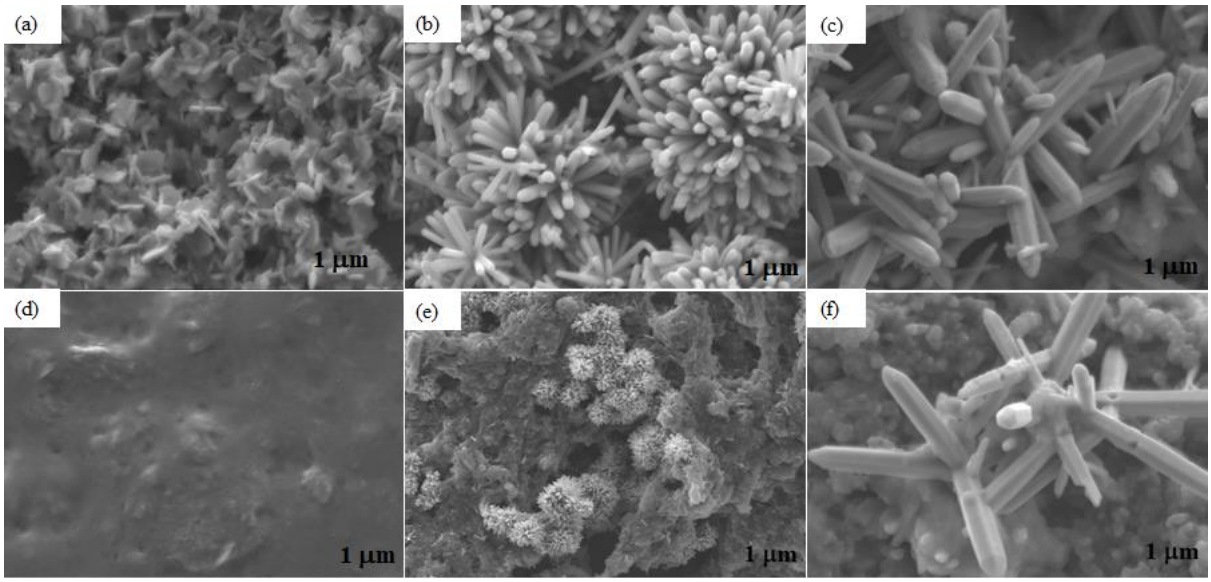

Figure 5. 5: FE-SEM images of (a) ZnO (b) ZnO_0.2TG (c) ZnO:3% Sm^{3+}, 5% Yb^{3+} (d) P3HT (e) P3HT-ZnO (1:5) and (f) P3HT-ZnO:3% Sm^{3+}, 5% Yb^{3+} (1:5).

Fig. 5.6 (a) and (b) show the EDS spectra of ZnO and ZnO-doped Sm^{3+} and Yb^{3+} co-doped with ZnO. (b). Figure 5.5 (a) shows that carbon (C), oxygen (O), zinc (Zn), and nickel are present (Ni). The carbon is owing to the use of conductive carbon tape during sample and pre-measurement preparation, while the Ni is due to system contamination. The presence of impurities (Sm^{3+} and Yb^{3+}) in the EDS spectrum are confirmed by Fig. 5. 6 (b). The integration of P3HT in ZnO doped with Sm^{3+} and Yb^{3+} shows that silicon (Si) comes from the borosilicate glass substrate and sulphur (S) from P3HT. The elemental map in Fig. 5.7 also illustrates the distribution of elements on the surface and confirms the composition of Zn, O, Sm, Yb, Sm, and Yb and S in the synthesized samples.

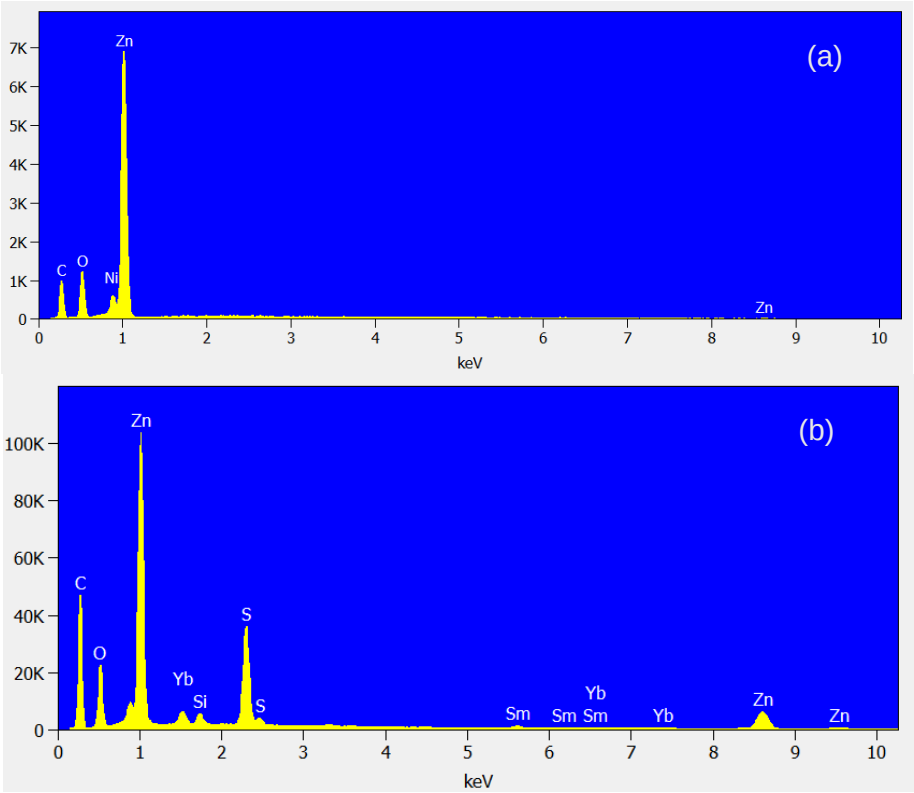

Figure 5. 6: EDS spectra of (a) ZnO (b) P3HT-ZnO:3% Sm^{3+},5% Yb^{3+} (1:5).

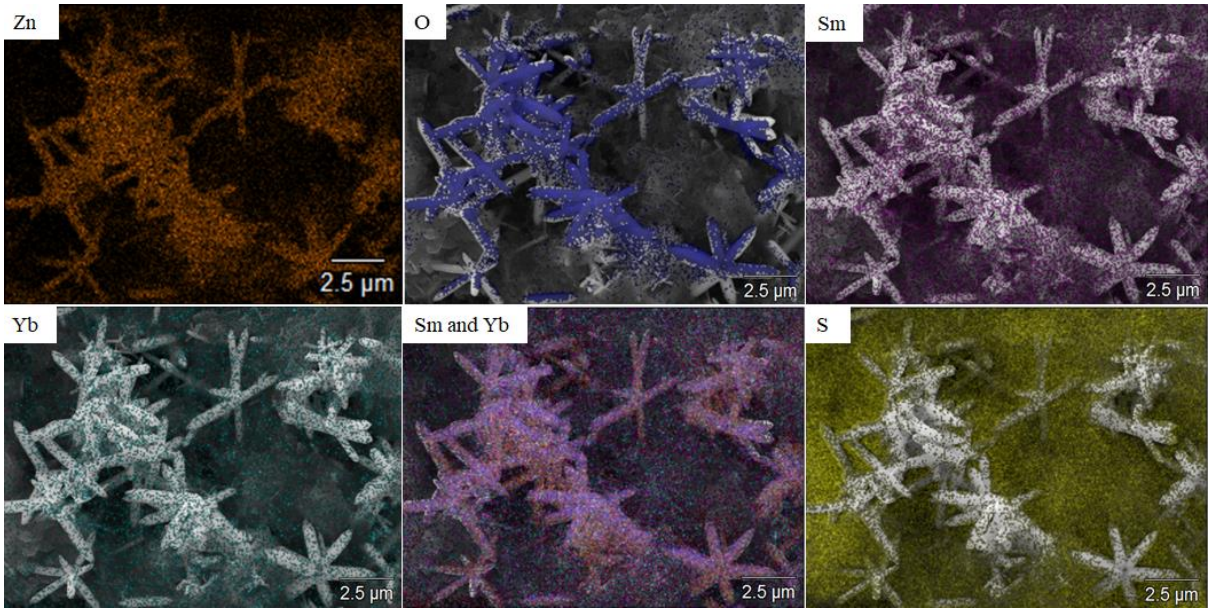

Figure 5. 7: The elemental mapping of P3HT-ZnO:3% Sm^{3+},5% Yb^{3+} (1:5).

5.3.5 X-ray photoelectron spectroscopy analysis

X-ray photoelectron spectroscopy was used to investigate the chemical state and elemental analysis of ZnO, P3HT, P3HT-ZnO (1:5), and P3HT-ZnO: 3% Sm^{3+}, 5% Yb^{3+} (1:5). (XPS). Prior to analysis, the binding energy (BE) was calibrated using the C 1s peak (284.8 eV). The spectral lines of Zn 2p are shown in Fig. 5.8 (a), with binding energies of 1022.94 eV (Zn $2p_{3/2}$) and 1045.96 eV (Zn $2p_{1/2}$) and spin-orbit spacing of 23.02 eV, which accords with the findings for Zn^{2+} in ZnO [38,39,47]. Al-Gaashani et al. [40] demonstrated three distinct nanoparticle morphologies: nanoparticles, nanoflowers, and nanorods. The binding energies of the Zn 2p components of ZnO nanorods are substantially greater than those of nanoparticles and nanoflowers, according to Al-Gaashani et al. [40], which can be related to the interaction of the chemical environment with the surface atoms. Fig. 5.8 (b) depicts pure P3HT, which has a significant peak at 169.875 eV. Huiling et al. [36] discovered that P3HT exhibits a band at 164.346 eV that corresponds to S $2p_{3/2}$ of the thiophene ring. Furthermore, we observe that our results switched to a greater binding energy, which might be related to the presence of absorbed light or atmospheric oxygen. In Fig. 5.8 (c), a band at 164.09 eV is assigned to the interaction of P3HT with ZnO [41], and a band at 165.05 eV is attributed to the S-C bond in P3HT [41]. Because of oxygen impurities in P3HT, Fig. 5.8 (d) displayed a wide band at around 532.73 eV [48].

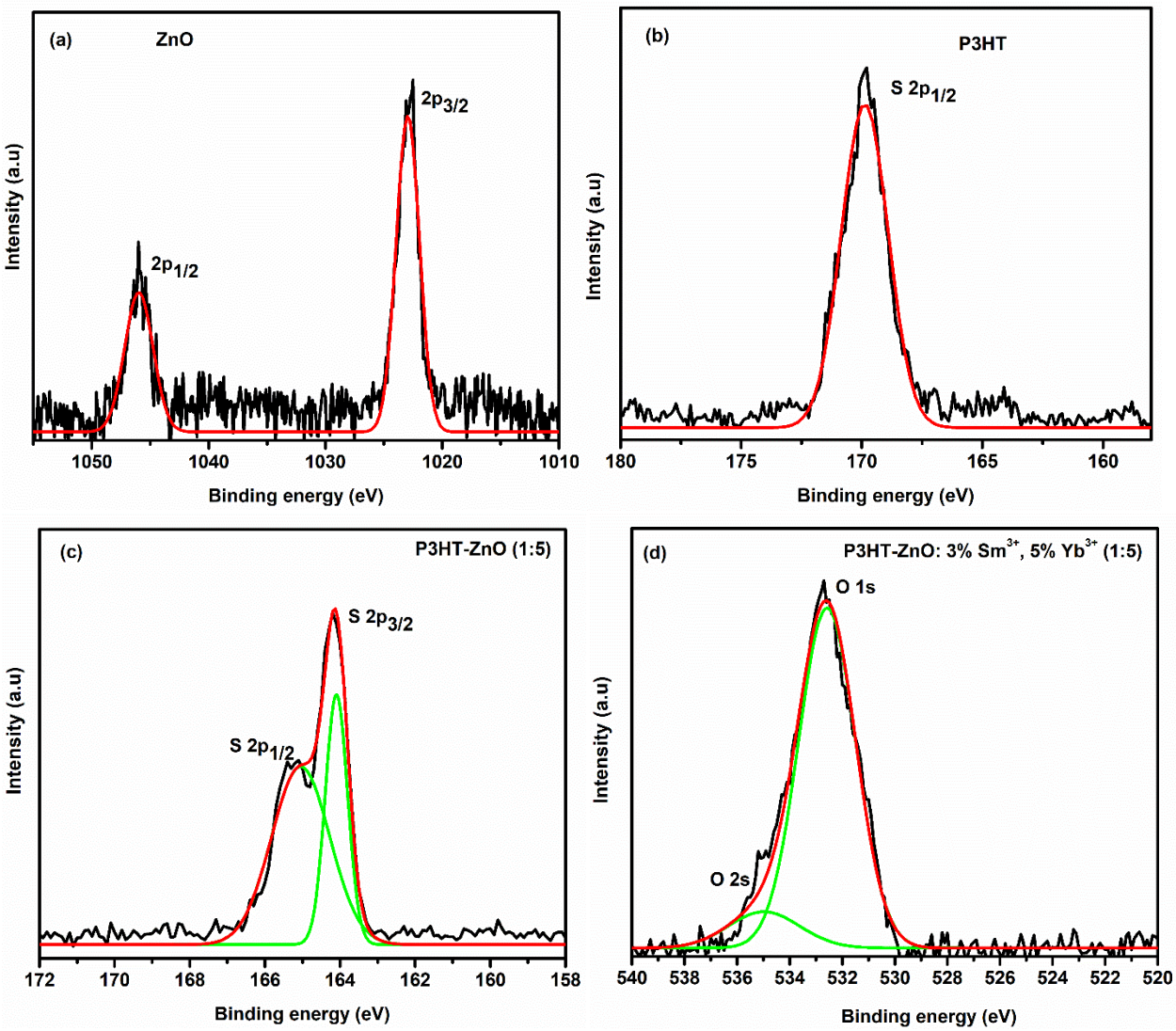

Figure 5. 8: (a) ZnO (b) P3HT (c) P3HT-ZnO (1:5) (d) P3HT-ZnO: 3% Sm^{3+}, 5% Yb^{3+} (1:5) XPS spectra.

5.3.6 FTIR analysis

FTIR spectroscopy experiments were done to better understand the interaction of undoped and doped ZnO with conductive P3HT, as illustrated in Fig. 5.9. The large absorption peak at around 3325 cm^{-1} is caused by O-H vibration, whereas the bands at approximately 2971 and 2889 cm^{-1} are caused by C-H stretching. The band at 1380 cm^{-1} is caused by CO_2 in the atmosphere, whereas the bands at 1084 and 1043 cm^{-1} are caused by the C=O asymmetric and symmetric stretch modes, respectively. Inorganic ZnO is responsible for the bands below 600 cm^{-1}. Furthermore, the absence of an S-H stretch mode at 2500 cm^{-1} shows that the thiol groups of the ligands are attached to the surface atoms of the nanorods via Zn-S interactions [19]. The peaks formed by P3HT, on the other hand, are still evident, and the shift in intensity is due to the - interaction between P3HT and undoped and/or doped ZnO [49]. P3HT with ZnO: 3%

Sm^{3+}, 5% Yb^{3+} exhibits higher absorbance intensity, suggesting a good interaction; findings correspond with UV/VIS/NIR and PL results from the same sample, demonstrating the maximum intensity as determined by FE-SEM, well-distributed particles.

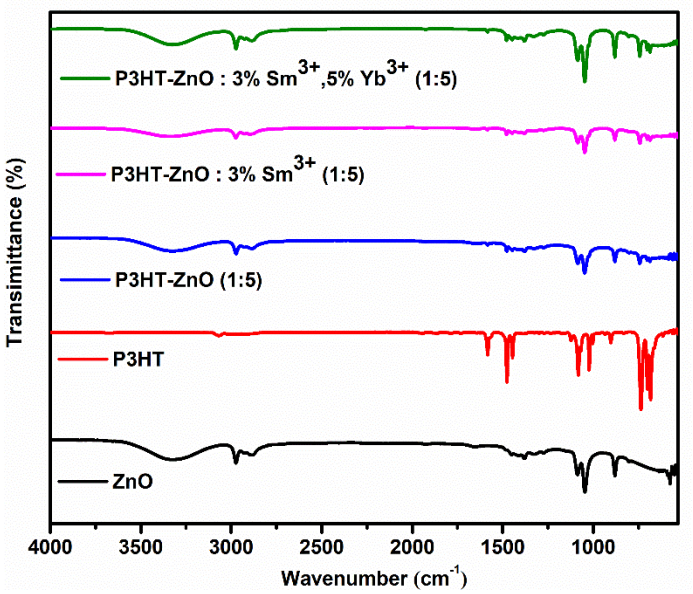

Figure 5. 9: ZnO, P3HT, P3HT-ZnO (1:5), P3HT-ZnO:3% Sm^{3+} (1:5) and P3HT-ZnO:3% Sm^{3+}, 5% Yb^{3+} (1:5) FTIR spectra.

5.3.7 Electrical Characterization

Fig. 5.10 shows the current-voltage (I-V) spectra of P3HT with undoped and doped ZnO. For all samples, the I-V curves exhibit non-linear rectification behaviour, and the trend is consistent and continuous, demonstrating stable contact between samples and probes. The observed current is smaller in the undoped ZnO and P3HT samples, demonstrating that the material functions as an insulator. However, it is obvious that when P3HT is integrated in ZnO at a 1:5 ratio, the rectification behaviour improves. Again, the P3HT-ZnO doped sample with Sm^{3+} and co-doped with Yb^{3+} ions is ohmic, showing the conductive materials well-known behaviour. The measured current increase in P3HT-ZnO: 3% Sm^{3+}, 5% Yb^{3+} (1:5) sample suggests that the conductivity of the sample increases with the introduction of the dopant Sm^{3+} and the co-dopant Yb^{3+}. As a result, we can conclude that doping enhances conductivity even more than P3HT and ZnO alone, these findings indicate probable better electron transport characteristics, which can lead to an increase in photovoltaic efficiency in organic solar devices. An increase in conductivity can be due to higher doping concentration and co-doping. These findings are similar to those of Ahmed et al. [50], who reported improvements in behaviour rectification when ZnO was doped with the Sm^{3+} ion, leading to increased conductivity. Once-again, the I-

V results are similar to the observations reported in our PL studies, where a considerable reduction of PL intensity was observed with P3HT-ZnO: 3% Sm^{3+}, 5% Yb^{3+} (1:5).

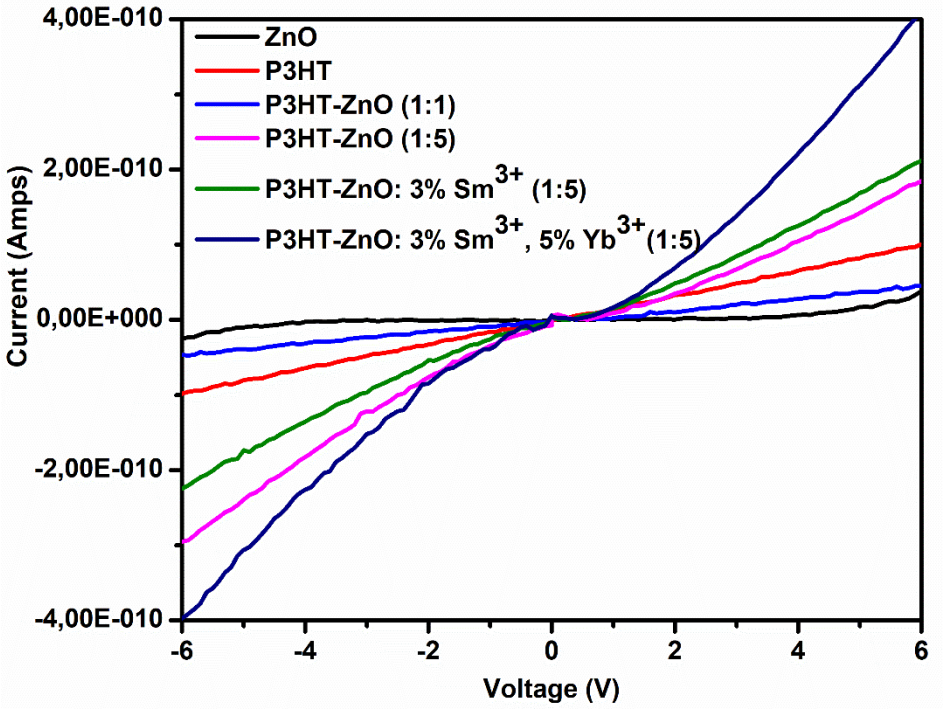

Figure 5. 10: The I-V spectra of ZnO, P3HT, P3HT-ZnO (1:5), P3HT-ZnO:3% Sm^{3+} (1:5) and P3HT-ZnO:3% Sm^{3+}, 5% Yb^{3+} (1:5).

5.4. Conclusion

The produced ZnO nanorods were effectively generated utilizing the microwave-assisted sol-gel technique using TG as a capping agent. Despite being capped or doped, the XRD verified the hexagonal structure and revealed no additional diffraction peaks other than those of ZnO. UV/VIS/NIR absorbance increased in both capped and doped samples. Incorporating the samples with P3HT also resulted in a significant absorption boost, providing a greater chance for increased efficiency in organic solar cells. PL studies revealed that ZnO capped with 0.2 TG had the maximum emission intensity, whereas ZnO:3% Sm^{3+}, 5% Yb^{3+} showed a slightly enhanced PL intensity. P3HT incorporated with ZnO:3% Sm^{3+}, 5% Yb^{3+} showed strong photoluminescence quenching effect, suggesting that it might be employed as an electron acceptor in the active layer of organic solar cell devices. FE-SEM revealed that the capped ZnO results in hexagonally formed flower-like nanorods, EDS corroborated the sample composition, and image mapping revealed the element distribution on the surface. The interaction between P3HT and ZnO was shown by XPS. The FTIR analysis revealed that all of the functional groups, and electrical measurements revealed that the P3HT-ZnO:3% Sm^{3+}, 5%

Yb^{3+} sample improved conductivity, making this material an excellent candidate for greatly accelerating electron transport, decreasing the rate of electron-hole recombination, and increasing the efficiency of organic solar cells.

References

[1] R. Joshi, *Materialia,* **2** (2018) 104 – 110.

[2] S. Jurablu, M. Farahmandijou, T.P. Firoozabadi, *J. Sci, Islamic Republic of Iran.,* **26** (2015) 281 – 285.

[3] L. Zhao, P.L. Lu, Z.Y Yuan, X.T. Guo, Y. Shen, H. Ye, G.F. Yuan, L. Zhang, *J. Appl. Phys*., **108** (2010) 113924.

[4] W.R. Bowen, R.W. Lovitt, C.J. Wright, *Biotechnol. Lett.,* **22** (2000) 893 – 903.

[5] A.L. Briseno, T.W. Holecome, A.I. Boukai, E.C. Garnett, S.W. Shelton, J.J.M. Frechet, P. Yang, *Nano Lett.,* **10** (2010) 334 – 340.

[6] T. Aoki, Y. Hatanaka, *Appl. Phys. Lett.,* **76** (2000) 3257 – 3258.

[7] N. Babayevska, B. Peplinska, M. Jarek, L. Yate, K. Tadyszak, J. Gapinski, I. Iatsinskyi, S. Jurga, *RSC Adv*., **6** (2016) 89305 – 89312.

[8] C. Gumus, O. M. Ozkendir, H. Kavak, Y. Ufuktepe, *J. optoelect. Adv. Mat.* **8** (2006) 299 – 303.

[9] N. Rawal, A.G. Vaishaly, H. Sharma, B.B. Mathew, *EPES.,* **2** (2015) 46 – 52. D

[10] R. Javed, M. Zia, M. Usman, *Appl. Surf. Sci.,* **386** (2016) 319 – 326.

[11] M. Faraz, F. K. Naqui, M. Shakir, N. Khare, *New J. Chem*., **42** (2018) 2295 – 2305.

[12] M.R. Anil Kumar, H.P. Nagaswarupa, C.R. Ravikumara, S.C. Prashantha, H. Nagabhushana, Aarti S. Bhatt, *J. Phys. Chem. Solids.,* **127** (2019) 127–139.

[13] E. Gorokhova, I. Venevtsev, I. Alekseeva, A. Khubetsov, O. Dymshits, L. Basyrova, E. Oreschenko, S. Eron'ko, F. Muktepavela, K. Kundzins, A Zhilin and P Loiko, *Journal of Physics: Conference Series,* **2086** (2021) 012015.

[14] G. L. Kabongo, G. H. Mhlongo, B. M. Mothudi, K. T. Hillie, H. C. Swart, M. S. Dhlamini, *Mater. Lett.* **119** (2014) 71 – 74.

[15] N. Assi, P. A. Azar, M. S. Tehrani, S. W. Husain, *J IRAN CHEM SOC,* **13** (2016) 1593–1602.

[16] S.K. Satpathy, U.K. Panigrahi, S.K. Panda, V. Thiruvengadam, R. Biswal, W. Luyten, P. Mallick, Mater. Today Commun., 28 (2021) 102725.

[17] S.K. Satpathy, U.K. Panigrahi, S.K. Panda, R. Biswal, W. Luyten, P. Mallick, J. Alloys Compd., 865 (2021) 158937.

[18] R. D. Deepika, S. Singh, A. Kumar, *Bull. Mater. Sci.,* **38** (2015) 1247 – 1252.

[19] J. J. R Arias, M. F. V Marques, *React. Funct. Polym.*, **113** (2017) 58 – 69.

[20] J. A. Haucha, P. Schilinskya, S. A. Choulisa, R. Childersb, M. Bielea, C. Brabeca, *J. Sol. Energy Mater. Sol. Cells.*, **92** (2008) 727 – 731.

[21] N.D. Treat, et al., *Adv. Energy Mater*., **1** (2011) 82 – 89.

[22] C. Liu, Z.C. Holman, U.R. Kortshagen, *Nano Lett.,* **9** (2009) 449 – 452.

[23] L.E. Greene, M. Law, B.D. Yuhas, P. Yang, *J. Phys. Chem. C Lett.,* **111** (2007) 18451 – 18459.

[24] D. Chen, A. Nakahara, D. Wei, D. Nordlund, T.P. Russell, *Nano Lett.,* (2011) 561 – 567.

[25] M. Seshadri, M. Radha, D. Rajesh, L.C Barbosa, Cordiero C.M.B, Y.C. Ratnakaram, *Physica B: Condesed Matter.*, **459** (2015) 79 – 87.

[26] Ch. Basavapoornima, T. Maheswari, S. R. Depuru, C.K. Jayasankar, *Optical materials,* **86** (2018) 256-269.

[27] P. Mou, N.R. Mathews, P. Santiago, X. Mathew, *J Nanopart Res.,* **14** (2012) 1 – 13.

[28] S. Aksoy, Y. Caglar, S. Ilican, M. Caglar, *J.Alloys. Comps,* **512** (2012) 171 – 178.

[29] R.G. Carvalho, M.T.S. Tavares, F.K.F. Oliviera, R.M. Nascimento, E. Longo, M.S. Li, C.A. Paskocimas, M.R.D. Bomio, F.V. Motta, *J. Mater Sci: Mater Electron., **28*** (2017) 7943 – 7950.

[30] B.D. Cullity, Elements of X-ray Diffraction (2nd Ed), Addison Wesley, 1956.

[31] T. Tsuji, Y. Terai, M.H.B. Kamarudin, M. Kawabata, Y. Fuji-wara, J. Non-Cryst. Solids. 358 (2012) 2443 – 2445.

[32] Y. Lee, C. Chiang, P. Jen, B. Chou, L. Wang, Y. Yi Cheng, Y. Lee, Y. Chen, C. Hsieh, C. Dai, *ACS Appl. Energy Mater.* 5 (**2018)** 1930-1941.

[33] C. Unni, D. Philip, K.G. Gopchandran, Spectrochimica Acta Part A., 71 (2008) 1402 – 1407.

[34] S. Shukla, D. K. Sharma, *Materials Today: Proceedings,* **34** (2021) 793 – 801.

[35] W. Shen, J. Tang, R. Yang, H. Cong, X. Bao, Y. Wang, X. Wang, Z. Huang, J. Liu, L. Huang, J. Jiao, Q. Xu, W. Chen, L. A. Belfiore, RSC Adv., 4 (2014) 4379 – 4386.

[36] T. Huiling, L. Xian, J. Yadong, X. Guangzhong, D. Xiaosong, *Sensors.* **15** (2015) 2086 – 2103.

[37] H. Oh, J. Krantz, I. Litzov, T. Stubhan, L. Pinna, C.J. Brabec, *Sol Energy Mater Sol Cells,* **95** (2011) 2194 – 2199.

[38] Y.S. No, T.W. Kim., *J. Ceram. Process. Res.* **14** (2013) 396 – 399.

[39] S.K.L. Devi, K. Sudarsanakumar, *J. Lumin.* **130** (2010) 1221 – 1224.

[40] R. Al-Gaashani, S. Radiman, A. R. Daud, N. Tabet, Y. Al-Douri, *Ceram. Int.*, **39** (2013) 2283 – 2292.

[41] G. L. Kabongo, P. S. Mbule, G. H. Mhlongo, B. M. Mothudi, K. T. Hillie, M.S. Dhlamini, *Nanoscale Res. Lett.*, **11** (2016) 418.

[42] A. Bahtiar, S. H. Tusaddiah, L. Safriani, *J. Phys.: Conf. Ser. 1*, **1080** (2018) 012001.

[43] A.H. Yuwono, A. Sholehah, S. Harjanto, D. Dhaneswara, F. Maulidiah, *Adv. Mater. Res.*, **789** (2013) 132 – 137.

[44] Z. Liang, Q. Zhang, L. Jiang, G. Cao, *Energy Environ. Sci.* **8** (2015) 3442–3476.

[45] U. Ozgur, D. Hofstetter, H. Morkoc, *Proc. IEEE,* **98** (2010) 1255–1268.

[46] B.S. Mwankemwa, T.D. Malevu, M.G. Sahini, S.A. Vuai, *Results in Materials*, **14** (2022) 100271.

[47] J.F. Moulder, W.F. Strickle, P. E. Sobol, K.D. Bomben, Handbook of X-ray photoelectron spectroscopy, Perkin-Elmer Corporation, Eden-Prairie MN,1992.

[48] H.O. Seo, M.G. Jeong, K.D. Kim, *Surf. Interface Anal*, **46** (2014) 544 – 549.

[49] R. Bhatia, L. Kumar, *J. Saudi Chem. Soc.* **21** (2017) 366 – 376.

[50] M.A.M. Ahmed, B.S. Mwankwemwa, E. Carleschi, B.P. Doyle, W.E. Meyer, J.M. Nel, *Mat. Sci. Semicon. Proc.*, **79** (2018) 53–60.

Chapter 6

Synthesis and Characterization of P3HT-ZnO-FWCNT nanocomposite for organic solar cell applications

This chapter presents microwave-assisted sol-gel synthesis of P3HT-ZnO: FWCNT for application in organic solar cells. (Article published in Physica B: Condensed Matter).

6.1. Introduction

Organic solar cells (OSC) have developed as a new challenger to conventional solar cells in recent decades, garnering considerable attention in business and research as flexible solar modules [1] due to their advantages, low cost [2], light weight [3], ease of manufacture [4] and large-scale production for the photovoltaic industry OSC consist of a thin layer of organic photovoltaic active layer placed between a transparent electrode and a metal electrode [3]. OSC consist of an electron acceptor-donor material, i.e., photons from solar radiation are absorbed by the electron donor (p-type), which then transfers their energy to an electron acceptor (n-type). In the last decade, researchers have researched OSC, which consists of zinc oxide (ZnO) nanorods and a semiconducting polymer such as poly(3-hexylthiophene) (P3HT) in the active layer [6]. In this case, P3HT functions as an electron donor in this instance by infiltrating in between the ZnO nanorods [6]. P3HT is one of the most widely used materials in photovoltaics due to its fascinating electrical properties, easy solubility in organic solvents, and capacity for self-assembly.[7].

ZnO is an n-type semiconductor with a wide range of 3.27 eV at room temperature and a binding energy of 60 meV [8]. Moreover, ZnO has a broad visible light transparency area and adequate light trapping abilities [9]. According to Zhu et al. [10], the combination of ZnO and carbon nanotubes (CNT) recently drew the attention of researchers and boosted the device performance [10]. ZnO optical and chemical characteristics can be enhanced further by integrating ZnO into CNT [8]. Due to their excellent conductivity, large surface area, low bulk density and mobility, CNT are used in various optoelectronic devices such as electrodes, semiconductors, transparent electrodes and gas sensors, among others [11, 12]. Furthermore,

CNT help to slow down electron-hole recombination [13]. Most metal oxides, including TiO2 [14], ZnO [15], and CuO [16], have been combined with CNT to create superior nanocomposite materials with adjustable nanostructural characteristics in recent years. Under visible light illumination, ZnO/CNT nanocomposites show increased photocatalytic activity and superior optical characteristics [8]. As illustrated in Fig. 6.1, CNT and P3HT band offset can increase excitons dissociation at the interface, allowing charge carriers (electrons and holes) to migrate from the polymer to the CNT [17]. Fig. 6.1 illustrates that P3HT light absorption is the first step in the formation of bound excitons. To transform light energy into an electrical signal, excitons must be split at the interface into free charge carriers (electrons and holes) [18]. The electrical process at the interface following light absorption by the polymer is also depicted in Fig. 6.1: (1) exciton production and diffusion to the donor-acceptor interface, (2) charge separation, (3) geminate recombination, and (4) complete dissociation leading to free carriers [19]. Actually, electrons and hole are separated at the acceptors lowest unoccupied molecular orbital (LUMO) and donors highest occupied molecular orbital (HOMO) levels, respectively [20]. Among other types of CNT, few-walled carbon nanotubes (FWCNT) are highly conductive, their field emission is stronger, and they are also known for their excellent electronics [21,22].

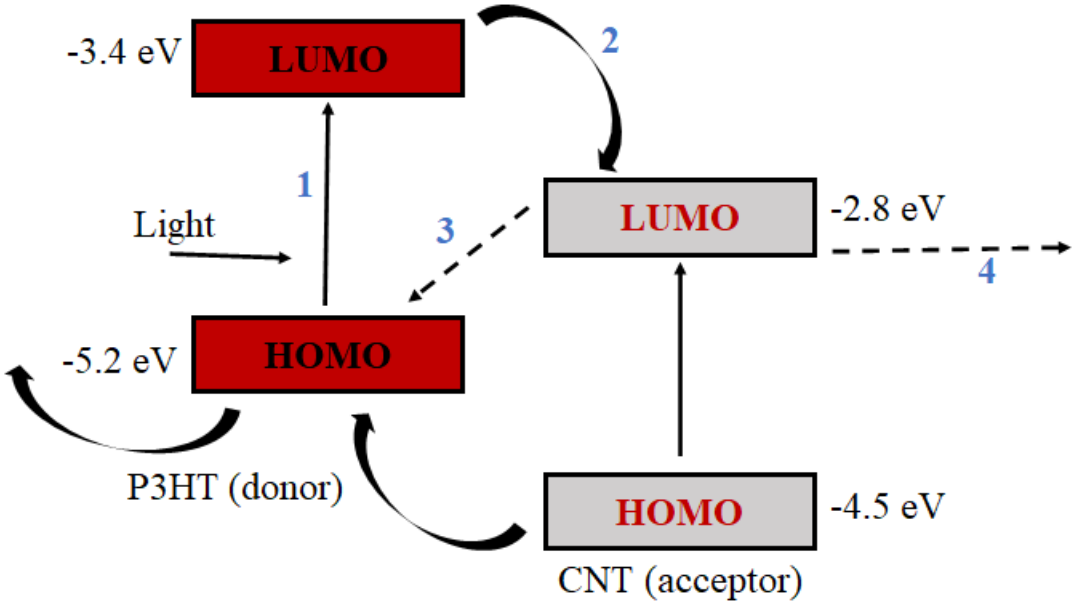

Figure 6.1: Schematic energy level diagram of P3HT-CNT at the interface [17-20].

In this chapter, microwave-assisted wet chemical sol-gel is employed to create ZnO nanorods, and thioglycerol (TG) is used as a capping agent. As a consequence, we adjusted ZnO: FWCNT by adjusting the concentration of FWCNT, and the optimum sample was ZnO: 3% FWCNT.

The inclusion of ZnO:3% FWCNT with P3HT was studied for structure, morphology, optical and electrical conductivity characteristics. Furthermore, P3HT-ZnO: 3% FWCNT is tested in different ratios to improve the absorption and conductivity of P3HT for inorganic solar cell applications.

6.2. Experimental Procedure

Zinc acetate dihydrate ($Zn(CH_3COO)_2 \cdot 2H_2O$; 99.5%), 1-thioglycerol (≥97.0%), sodium hydroxide (NaOH, 97%), Few-walled carbon nanotube (FWCNT) and pure Poly(3-hexylthiophene-2,5-diyl) $(C_{10}H_{14}S)n$, M_w = 20 000), chlorobenzene (anhydrous, 99.8%), ethanol (anhydrous, 96.0%) and borosilicate glass substrate were all acquired from Sigma-Aldrich (South Africa) and utilized without additional purification.

6.2.2 Microwave-assisted sol-gel synthesis of ZnO and preparation of ZnO-P3HT: FWCNT

The hexagonally shaped ZnO nanorods were made by dissolving 2.5g of zinc acetate dihydrate in 100 ml deionized water, adding 1-thioglycerol (TG) as a capping agent, and stirring the solution for 15 minutes on a magnetic stirrer. The presence of TG in the solution was employed to manage particle size distribution and avoid agglomeration. On the other hand, 4 g sodium hydroxide (NaOH; 97%) was dissolved in 30 ml of deionised water for 15 minutes while stirring the liquid. The sodium hydroxide solution was then dropped into the zinc solution one at a time. At room temperature, a white solution was swirled for 1 hour with a magnetic stirrer. Without further purification, Sigma Aldrich provided few-walled carbon nanotubes (FWCNT) and poly(3 - hexylthiophene) (P3HT). FWCNT were dissolved in chlorobenzene for 30 minutes in an ultrasonic bath and stirred on a magnetic stirrer for 24 hours. P3HT was also dissolved in chlorobenzene and whirled for 24 hours on the magnetic stirrer to integrate with undoped and doped ZnO. The materials were sonicated for 30 minutes and whirled on a magnetic stirrer for 3 hours after direct mixing of P3HT with undoped and doped ZnO. To create the thin films, a pipette was used to drop-cast the solution onto the ultrasonically cleaned borosilicate glass substrate. The films were then allowed to cure at ambient temperature. Furthermore, ZnO: FWCNT were adjusted, and P3HT-ZnO (1:1) and P3HT-ZnO: FWCNT were studied for use in organic solar cells.

6.2.3 Characterization techniques

As discussed in chapter 3 the structure and crystallinity of the produced materials were evaluated using a Rigaku SmartLab X-Ray diffractometer with a Cu-K radiation source (λ = 0.154059 nm). A PerkinElmer FTIR spectrometer was used to determine functional groups. The absorbance was measured using a PerkinElmer Lambda 1050 UV/VIS/NIR Spectrophotometer. FE-SEM pictures were captured using a JEOL JSM-7800F and a Thermo Scientific Ultradry EDS detector. PL measurements were taken with a Horiba Fluorolog-3 Jobin Yvon spectrometer at excitation wavelengths of 265 and 530 nm. Keithley 6487 picoammeter with a voltage source was used to measure current-voltage (I-V). The measurements were done in the dark and at room temperature using the thin film (303 K).

6.3. Results and discussion

6.3.1 X-ray diffraction Analysis

The crystal structure of ZnO nanorods, ZnO: FWCNT and P3HT-ZnO:FWCNT nanocomposites was studied by XRD. Fig. 6.2 shows XRD patterns of P3HT, ZnO, ZnO: 1% FWCNT, ZnO: 2% FWCNT, ZnO: 3% FWCNT, and P3HT-ZnO: 3% FWCNT nanorods. The results show that ZnO has a hexagonal wurtzite structure, according to ICDD card no. 01-074-9940. FWCNT has a carbon (C) structure corresponding to ICDD card number 01-082-8810. The results show that all samples prepared have both a carbon structure and a hexagonal structure, with C peaks marked with an asterisk (*). The more the doping percentage of FWCNTs increases the more we observe the carbon peaks. Arsalani et. al. [23] synthesized ZnO/CNT nanocomposites by two-step ball milling-hydrothermal synthesis and observed no CNT peaks in the ZnO/CNT nanocomposites due to low CNT percentage. However, when the CNT percentage is 20, they started to slightly observe the CNT peak at 25.7^{o} suggesting that increasing the CNT percentage rate increases the CNT peaks in ZnO/CNT nanocomposites. Incorporation of P3HT into ZnO:3% FWCNT nanocomposites further intensifies the C peaks due to high conductivity in FWCNT and therefore improved UV, PL, and I-V properties are expected based on this observation. Due to their unique electronic characteristics, when FWCNT are integrated into a material, they can increase UV absorption capacity and, if properly separated, they can limit radiative recombination which might increase PL intensity by functioning as efficient charge carriers [18, 20]. Furthermore, when FWCNT are introduced

into a conductive material or composite, they can improve the electrical conductivity of the composite [20].

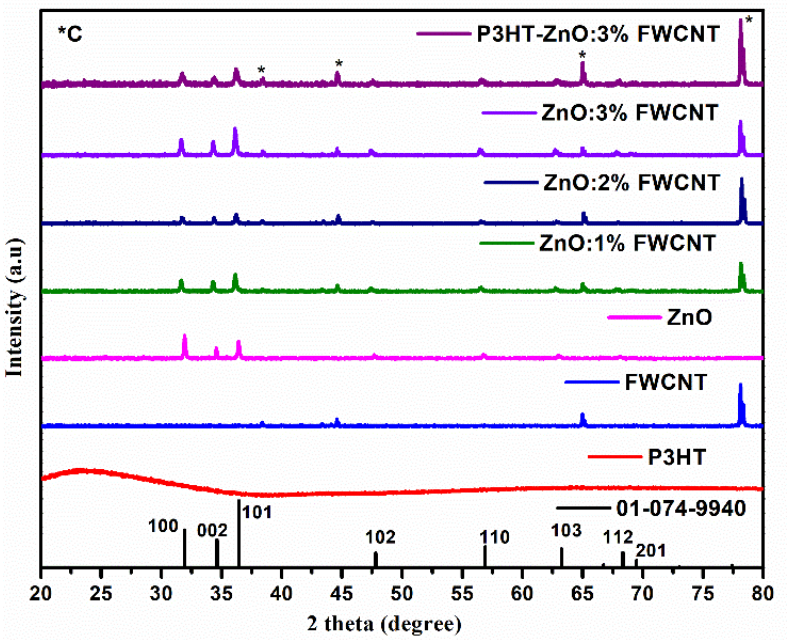

Figure 6. 2: XRD patterns of P3HT, FWCNT, ZnO, ZnO doped with 1, 2 and 3% of FWCNT, P3HT-ZnO:3% FWCNT.

6.3.2 UV/VIS/NIR-NIR Analysis

The UV/VIS/NIR absorption spectra of ZnO as-prepared, ZnO:1% FWCNT, ZnO:2% FWCNT, and ZnO:3% FWCNT are shown in Fig. 6.3 (a). The normalized absorption spectra show peaks at ~265 nm for the ZnO: FWCNT nanocomposite and ~370 nm for ZnO. As shown in the spectra, there is a blue shift in the absorption peak of undoped ZnO and nanocomposites. The blue-shift absorption spectra of undoped and doped samples show an increase in band gap, probably due to the quantum size effect [24]. ZnO: FWCNT nanocomposites have the maximum absorption peak compared to undoped ZnO, which is attributed to the presence of black FWCNT [25]. The absorption peaks of nanocomposites increase with increasing FWCNT content. Similar results were reported by Ibrahim et. al. [26] where they observed absorption peaks at ~251 nm for ZnO-CNT nanocomposite and at ~370 nm for the ZnO nanomaterial.

Normalized absorption spectra for P3HT, P3HT-ZnO (1:1 volume ratio), and P3HT-ZnO:3% FWCNT are shown in Fig. 6.3 (b). The results reveal enhanced spectra, with the greatest absorption intensity being P3HT-ZnO:3% FWCNT. The increased absorption shows that the

efficiency of organic solar cells might be increased by photon absorption [27]. The spectra demonstrate that the sample exhibits the same vibrational modes as the excited electronic state absorption peaks, which are located at 520, 560, and 618 nm and are ascribed to P3HT π-π* transformations [28].

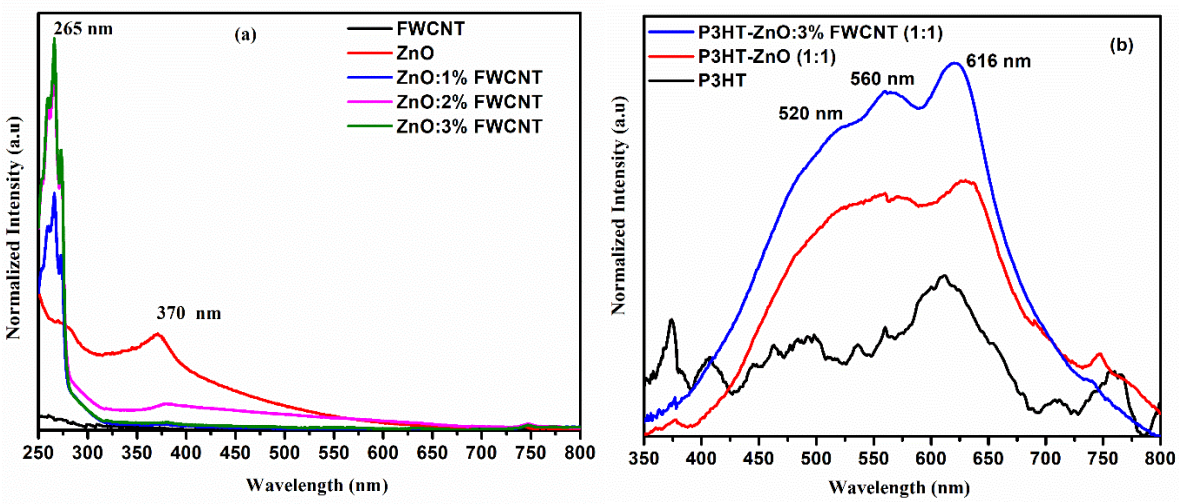

Figure 6. 3: Normalized absorption spectra of (a) FWCNT, ZnO, ZnO/FWCNT with 1, 2 and 3% of FWCNT (b) P3HT, P3HT-ZnO (1:1) and P3HT-ZnO:3% FWCNT (1:1).

Fig. 6.4 (a) shows the optical bandgap for ZnO and ZnO:3% FWCNT, (b) shows the optical bandgap for P3HT and P3HT-ZnO:3% FWCNT (1:1). The optical bandgap was extrapolated from the linear portion of the Tau's plot [29]:

$$\alpha h\nu = A(h\nu\text{-}Eg)^{1/2} \quad (1)$$

Where A is the constant, $h\nu$ is the photon energy (h=Plank's constant and ν is frequency of a photon) and α is the absorption coefficient. Extrapolating from the linear part of Tauc's plot ($(\alpha h\nu)^2$ vs $h\nu$) the predicted bandgaps are shown in Fig. 6.4 (a and b) and the bandgap were found to be ~3.09, 3.00, 3.07 and ~3.00 eV for ZnO, ZnO:1% FWCNT, ZnO:2% FWCNT and ZnO:3% FWCNT, respectively, suggesting a blue-shift. The estimated bandgap for P3HT, P3HT-ZnO (1:1) and P3HT-ZnO:3% FWCNT (1:1) which were extrapolated from the linear section of the Tauc's plot were predicted to be 1.80, 2.40 and 1.90 eV as shown in Fig. 6.4 (b).

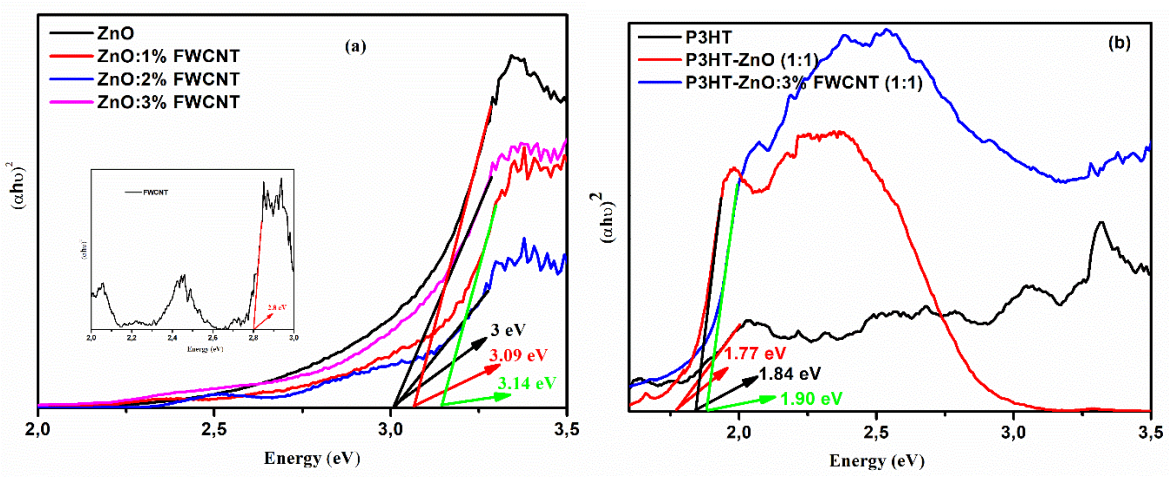

Figure 6. 4: Tauc's plot of (a) ZnO and ZnO:3% FWCNT (b) P3HT and P3HT-ZnO:3% FWCNT (1:1).

6.3.3 PL Analysis

Photoluminescence (PL) spectra of ZnO and ZnO doped with different concentrations of FWCNT were recorded at room temperature and excited with a 265 nm xenon lamp, as shown in Fig. 6.5 (a). The emission peaks show a red shift from about 443 nm ZnO to about 495 nm doped ZnO. The shift is caused by the defect level emission and the band gap reduction [30]. According to Mahato et al. [31] the emission peak of the PL spectrum for the ZnO-CNT nanocomposite is usually observed at ~375 nm, therefore the peak at ~495 is due to ZnO and FWCNT behaving as luminescent centers [32]. According to Look et al. [33] ZnO is an n-type semiconductor due to the zinc interstitial and oxygen vacancies, and FWCNT are p-type semiconductors, an n-p depletion layer form at the ZnO: FWCNT interface. This can create a narrow bandgap and is the origin cause of applications in optoelectronics [32]. The PL intensity in the spectra increases with increasing sp2 Content in the disordered carbon systems [34].

The PL measurements in Fig. 6.5 (b) were performed to examine the charge transfer between the donor-acceptor pair (P3HT: ZnO), and the emission spectrum was compared with that of P3HT. The P3HT emission shows peaks at ~636 and ~690 nm, corresponding to a pure electronic transition in pure P3HT [35]. P3HT-ZnO (1:1) exhibits higher emission intensity and has the same spectrum as P3HT, the spectrum shows no charge transfer from P3HT to ZnO. P3HT-ZnO:3% FWCNT (1:1) significantly suppressed the emission of P3HT and this phenomenon is known to be beneficial for increasing the mobility of charge carrier, prolonging the diffusion path free-carriers and increased phonon activity in organic solar cells. A drop in PL intensity indicates charge transfer between donor-acceptor materials and, as a result, a

decrease in charge recombination rate. Furthermore, ZnO has a low exciton binding energy, and its conduction band is lower than the lowest unoccupied molecular orbitals (LUMO) of P3HT, which allows charge transfer from the departed electrons in P3HT to ZnO nanorods. [36].

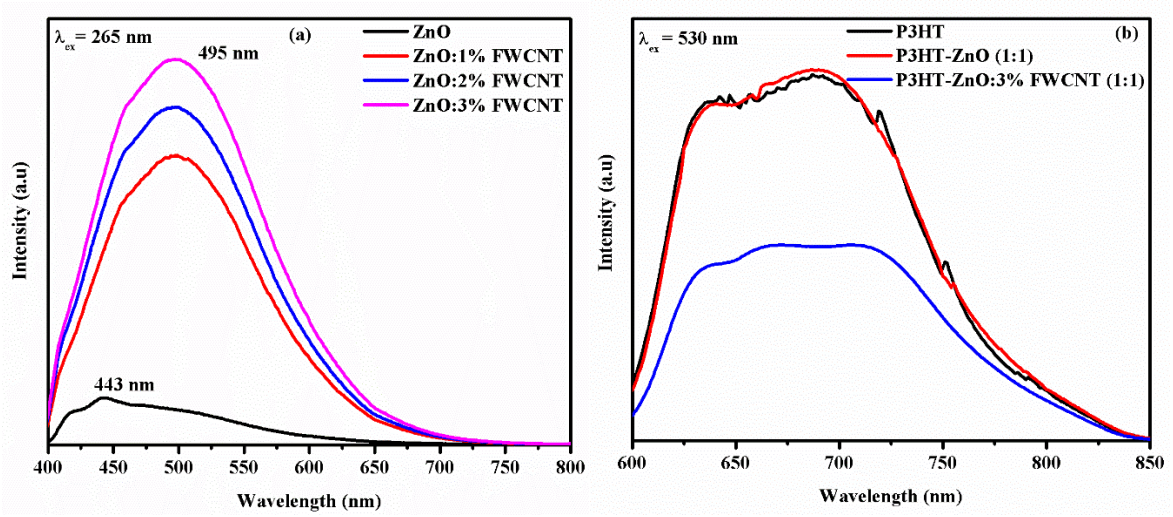

Figure 6. 5: Emission spectra of (a) ZnO, ZnO doped with 1, 2 and 3% of FWCNT excited at 265 nm (b) P3HT, P3HT-ZnO (1:1) and P3HT-ZnO:3% FWCNT (1:1) excited at 530 nm.

6.3.4 FE-SEM analysis

Field emission scanning electron microscopy was used to investigate the sample morphology (FE-SEM). The SEM picture of ZnO in Fig. 6.6 (a) reveals the development of flower-like nanorods. ZnO nanorods and FWCNTs are shown in Fig. 6.6 (b). The shape of organic P3HT is seen in Fig. 6.6 (c). Fig. 6.6 (d) and (e) show SEM images of P3HT-ZnO (1:1) and P3HT-ZnO:3% FWCNT (1:1), respectively. These findings demonstrated a well-mixed nanorod and P3HT structure. This mixture's homogeneity can aid increase photon absorption in organic solar cell devices, enhancing efficiency. ZnO nanorods are often chosen over spherical nanoparticles for increasing device performance because they have a ballistic effect that leads to quicker electron transfer and/or greater charge carrier mobility. Furthermore, the objective is to find a nanocomposite with the greatest PL quenching effect, suggesting the greatest charge separation potential in the photoactive layer, therefore P3HT-ZnO: 3% FWCNT (1:1) is predicted to increase the electrical conductivity of P3HT.

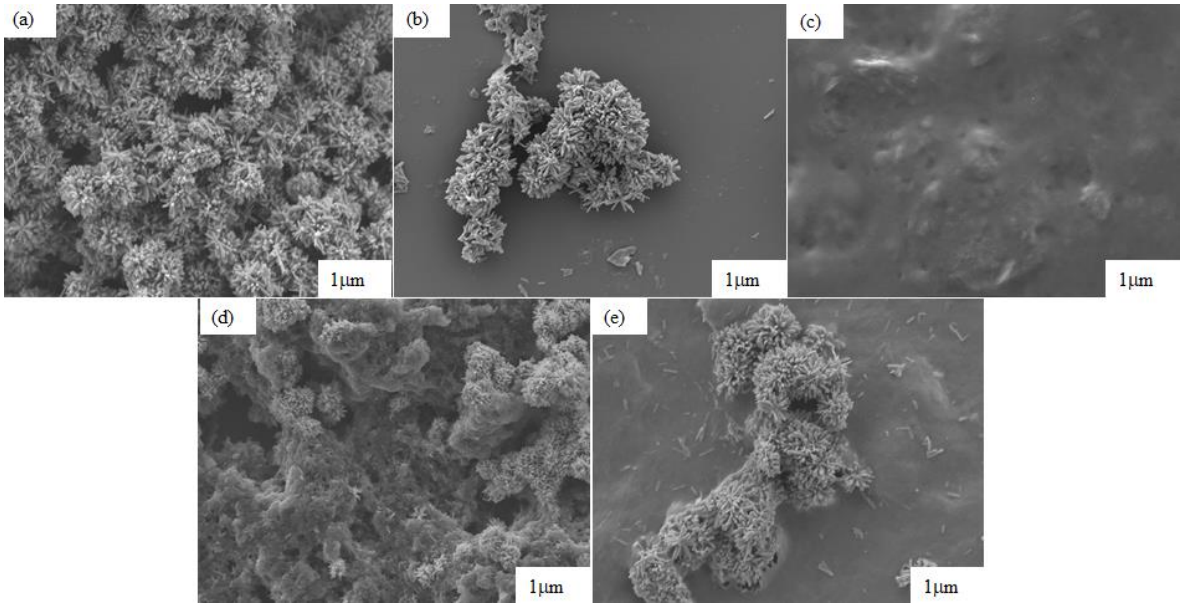

Figure 6. 6: FE-SEM images of (a) ZnO (b) ZnO:3% FWCNT (c) P3HT (d) P3HT-ZnO (1:1) and (e) P3HT-ZnO:3% FWCNT (1:1).

6.3.5 Electrical conductivity Analysis

Figure 6.7 depicts current-voltage (I-V) graphs of FWCNT, ZnO, P3HT, P3HT-ZnO (1:1) and P3HT:ZnO-FWCNT (1:1) respectively. All samples exhibit nonlinear rectification behaviour, and the trend is constant and continuous, demonstrating stable contact between samples and probes. The observed current is smaller in the undoped ZnO and P3HT samples, demonstrating that the material functions as an insulator. However, the spectra clearly reveal that when P3HT is combined with ZnO:3% FWCNT in a 1:1 ratio, the rectification behaviour improves. As a result, we can confidently state that ZnO: FWCNT enhances conductivity when compared to simply P3HT and ZnO, and this fact shows that superior electron transport characteristics may be responsible for improved photovoltaic performance in organic solar cells. The rise in conductivity is due to an increase in dopant concentration. These I-V results are consistent with our PL findings, which showed that the P3HT-ZnO sample had considerable PL intensity quenching: 3% FWCNT (1:1).

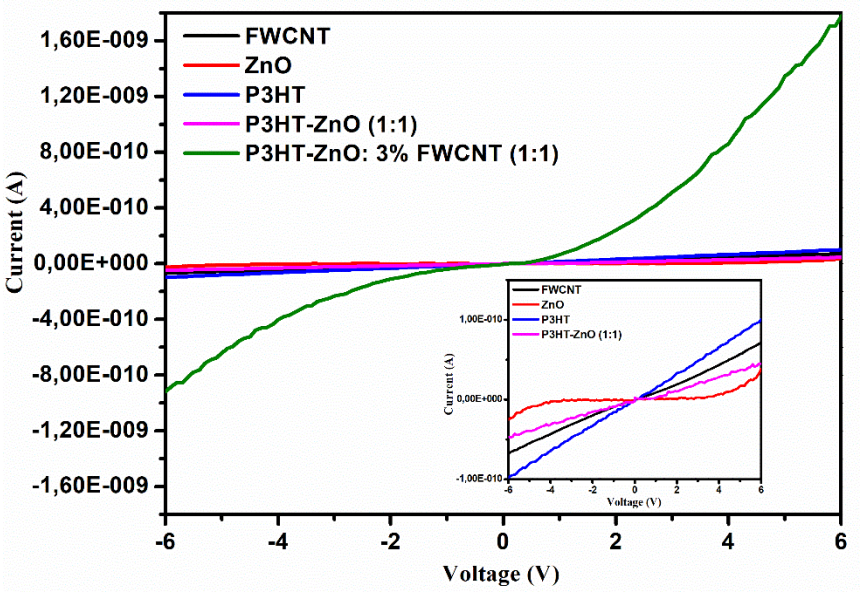

Figure 6. 7: The I-V characteristic spectra of ZnO, P3HT, P3HT-ZnO (1:1), P3HT-ZnO:3% FWCNT (1:1).

6.4. Conclusion

We have successfully synthesized samples prepared using the microwave-assisted sol-gel method. XRD analysis confirmed the hexagonal structure and that the nanocomposites exhibit both hexagonal wurtzite and carbon (C) structures. UV Visibility and PL showed that ZnO:3% FWCNT has the greatest absorption efficiency and emission intensity, respectively. The addition of P3HT to ZnO nanocomposite samples resulted in a significant increase in absorption, offering a greater potential to improve the efficiency of organic solar cells. P3HT incorporation with ZnO:3% FWCNT demonstrated a strong photoluminescence quenching effect, suggesting its potential usage as an electron acceptor in the active layer of organic solar cells. FE-SEM showed that ZnO has flower-like nanorods, and electrical measurements showed that the P3HT-ZnO: 3% FWCNT (1:1) sample exhibited improved conductivity, making this material an excellent candidate for greatly accelerating electron transport, reducing the electron-hole recombination rate, and increasing the efficiency of organic solar power cells.

References

[1] K. Kalyanasundaram, M. Gratzel, *J. Mater. Chem*. **22 (**2012) 24190 – 24194.

[2] J. Nozik, J. Miller, *Chem. Rev*. **110** (2010) 6443 – 6445.

[3] R. Luna-Rubio, M. Trejo-Peria, D. Vargas-Vázquez, G. Ríos-Moreno. *J, Sol. Energy,* **86** (2012) 1077 – 1088.

[4] G. Muller-Furstenberger, M. Wagner, *Ecol. Econ*. **62** (2007**)** 648 – 660.

[5] M. R. Simmons, In The Coming Saudi Oil Shock and the World Economy; John Wiley & Sons: Hoboken, NJ, USA, 2005.

[6] H. Qiu, J. H. Shim, J. Cho, J. M. Mativetsky, ASC Appl. Energy Mater. **1** (2018) 6172-6180.

[7] A. M. Diez-Pascual, J. A. L. Sanchez, R. P. Capilla, P. G. Diaz, *Polymers*, **10** (2018) 1 – 22.

[8] W. D. Zhang, *Nanotechnology*, **17** (2006) 1036.

[9] S. Aseena, N. Abraham, V. S. Babu, (2019*) International Conference on Vision Towards Emerging Trends in Communication and Networking (ViTECoN).*

[10] H. Zhu, J. Wei, K. Wang, D. Wu, *Sol. Energy Mater. Sol. Cell*. **93** (2009) 1461–1470.

[11] V. Skakalova, U. Dettlaff-Weglikowska and S. Roth, *Synth Met* **152 (**2005) 349.

[12] B. J. Landi, R. P. Raffaelle, S. L. Castro and S. G. Bailey, *Progress in Photovoltaics,* **13** (2005) 165– 172.

[13] Y. Feng, H. Zhang, Y. Hou, T. P. McNicholas, D. Yuan, S. Yang, L. Ding, W. Feng, J. Liu, *ASC Nano,* **2** (2008) 1634–1638.

[14] S. Da Dalt, A. K. Alves, C. P. Bergmann, *Materials Research*, **19** (2016) 1372–1375.

[15] S. Qu, M. Wang, M. Y. Chen, Q. Yao, L. Chen, *RSC. Adv.* **8** (2018) 33855–33863.

[16] J. Zheng, Q. Zhang, X. He, M. Gao, X. Ma, and G. Li, *Procedia Engineering*, **36** (2012) 235–245.

[17] S. Cataldo, P. Salice, E. Menna, B. Pignataro, *Energy Environ Sci*, **5** (2012) 5919–5940.

[18] Anass Bakour, Omar Bajjou, Mimouna Baitoul, Florian Massuyeau, Jany Wéry, Malik Maaza, Eric Faulques, *Materials Today: Proceedings,* **36** (2021) 549 – 552.

[19] Lefrançois, A., Luszczynska, B., Pepin-Donat, B. *et al.*, *Sci Rep* **5** (2015) 7768.

[20] Edigar Muchuweni, Edwin T. Mombeshora, Bice S. Martincigh and Vincent O. Nyamori, *Front. Chem.* **9** (2022) 733552.

[21] Y. Feng, H. Zhang, Y. Hou, T. P. McNicholas, D. Yuan, S. Yang, L. Ding, W. Feng, J. Liu, *ASC Nano*, **2** (2008) 1634–1638

[22] M. Ma, Z. Miao, D. Zhang, X. Du, Y Zhang, Zhang C, Lin J, Chen Q, *Biosensors and Bioelectronics*, **64** (2015) 477–484.

[23] N. Arsalani, S. Bazazi, M. Abuali, S. Jodeyri, *Journal of Photochemistry & Photobiology A: Chemistry*, **389** (2020) 112207.

[24] M. A. M Khan, S. Kumar, M. N. Khan, M. Ahamed, A. S Al Dwayyan, *J. Lumin* **155** (2014) 275 – 281.

[25] K. Danish, A. Zahid, A. Danyal, K. P. Manoj, K. Idris, *Ain Shams Eng. J*, **12** (2021) 897 – 900.

[26] A. A., A. Umar, R. Ahmad, R. Kumar, S. Baskoutas, *Nanoscience and Nanotechnology Letters*, **8** (2016) 853 – 858.

[27] W. Shen, J. Tang, R. Yang, H. Cong, X. Bao, Y. Wang, X. Wang, Z. Huang, J. Liu, L. Huang, J. Jiao, Q. Xu, W. Chen, L. A. Belfiore, RSC Adv. 4 (2014) 4379 – 4386.

[28] T. Huiling, L. Xian, J. Yadong, X. Guangzhong, D. Xiaosong, *Sensors.* **15** (2015) 2086 – 2103.

[29] H. Oh, J. Krantz, I. Litzov, T. Stubhan, L. Pinna, C. J. Brabec, *Sol Energy Mater Sol Cells*, **95** (2011) 2194 – 2199.

[30] N. Abrahams, A. Rufus, C. Unni, D. Philip, *Spectrochimia Acta Part A: Molecular and Biomolecular Spectroscopy*, **200** (2018) 116 – 126.

[31] T. H. Mahato, G. K. Prasad, B. Singh, J. Acharya, A. R. Srivastava, R. Vijayaragjavan, *J Hazard Mater*, **165** (2009) 928–932.

[32] A. Ayeshamariam, D. Saravanakkumar, M. Kashif, S. Sivaranjani, B. Ravikumar, *Mechanics of Advanced Materials and Modern Processes* **2** (2016) 1 – 8.

[33] D. C. Look, J. W. Hemsky, J. R. Sizelove, *Phys Rev Lett*, **82** (1999) 2552.

[34] G. Eda, Y. Lin, C. Mattevi, H. Yamaguchi, H. Chen, I. Chen, *Adv Mater* **22** (2010) 505–509.

[35] R. Al-Gaashani, S. Radiman, A. R. Daud, N. Tabet, Y. Al-Douri, *Ceram. Int.* **39** (2013) 2283 – 2292.

[36] A. Bahtiar, S. H. Tusaddiah, L. Safriani, *J. Phys.: Conf. Ser. 1*, **1080** (2018) 012001.

Chapter 7

Characterization of P3HT-FWCNT thin film for photovoltaic solar cell applications.

The chapter discusses the characterization of P3HT-FWCNT thin films for photovoltaic solar cell applications. (SAIP2021 proceedings article)

7.1. Introduction

The global contribution of photovoltaic (PV) technology to energy production is still marginal today and is expected to remain so for a long time, especially in poor developing countries [1]. Evidence that the global impact of solar power is shown by the increasing share of fossil fuels in the electricity generation market [2]. Carbon nanotubes (CNT) have emerged as one of the key additives to improve the thermoelectric properties of organic materials due to their unique structure and excellent electron transport properties [3]. CNT are the most commonly used and effective filling material. They can provide conductive pathways when incorporated into a polymer matrix as CNT exhibit excellent electrical conductivity and high charge mobility [3]. These CNT can be classified into three (3) types: single-walled carbon nanotubes (SWCNT), few-walled carbon nanotubes (FWCNT), and multi-walled carbon nanotubes (MWCNT) [4]. The high conductivity of CNT is based on the availability of free electrons by sp^2 hybridized carbon atoms in the hexagonal plane of graphite [5]. The electrical behaviour of SWCNT can be determined by their chirality, metallic or semiconducting [6], however, MWCNTs are metallic if at least one layer exhibits metallic chirality [7]. Compared to other CNT, FWCNT are known for their remarkable electronic properties [8], conductivity and field emission are stronger [9]. Jung et al. [10] incorporated FWCNT with various conducting polymers, including poly(3-hexylthiophene) (P3HT) for thermoelectric properties. They also reported the highest thermal conductivity when FWCNT was incorporated into P3HT compared to other conducting polymers. Khan et al. [11] prepared MWCNT mixed with P3HT as a photoactive layer for organic solar cells. In their results, they reported a photoelectric conversion efficiency (PCE) of 2.35%.

Organic electronics based on conducting polymers have recently been the subject of intense research due to their interesting band gap and can also be easily used to fabricate thin films [11]. These conductive polymers have been used in organic light-emitting diodes (OLEDs), organic gas sensors (OGS) and organic solar cells (OSCs), among others [12-16]. Poly(3-hexylthiophene) P3HT is a conjugated electron donor polymer that is widely used in solar cells due to its good electro-optical properties, ease of processing and synthesis [18-22] and is considered a pillar in the development of future nanostructured polymer solar cells [23]. P3HT was most commonly used in organic solar cells due to its narrow band gap (1.93-1.95 eV), whereby a broad energy spectrum can be absorbed [17]. This chapter examines P3HT-FWCNT in different ratios to improve the absorption and conductivity of P3HT for organic solar cell applications.

7.2. Experimental Procedure

Few-walled carbon nanotubes (FWCNT) and poly(3 – hexylthiophene) (P3HT) in this study were purchased from Sigma Aldrich used without further purification. FWCNT was dissolved in chlorobenzene using the ultrasonic bath for 30 minutes and P3HT was also dissolved in chlorobenzene and stirred on the magnetic stirrer for 24 hours. P3HT was incorporated in FWCNT at different ratios, the composites were stirred on the magnetic stirrer for 3 hours. The thin films were prepared by using a pipette to drop-cast the solution onto the ultrasonically cleaned borosilicate glass substrate and thereafter the film was then allowed to dry at room temperature. The thin films were then characterized using X-ray diffraction (XRD), ultraviolet to visible (UV/VIS/NIR) spectrophotometer and photoluminescence (PL) spectroscopy, field emission scanning electron microscopy (FE-SEM) and current-voltage (I-V) characterization.

7.3.1 X-ray diffraction Analysis

Fig. 7.1 shows XRD results of thin films made by drop casting. The results show a clear FWCNT cubic structure according to ICDD no. 01-082-8810 for all samples. Furthermore, it clearly shows that as the P3HT-FWCNT ratio increases, the intensity of the (302) peak decreases while (102) and (112) increases. The decrease in intensity (302) clearly shows that P3HT covers the surface of the FWCNT. The increase in (102) and (112) intensity is due to the interaction of P3HT-FWCNT which can result in increased crystallinity due to the alignment or stretching of P3HT chains along the surface of the nanotube. The results show that the 1:1 ratio is more crystalline than the other samples, so the composite in this ratio is further examined with other techniques like UV/VIS/NIR, SEM and others. The average crystallite

size was found to be approximately 19, 18, 16, 15, and 10 nm for FWCNT and P3HT-FWCNT, respectively, at different ratios. The average crystallite sizes were calculated using the Scherrer equation [25]:

$$D = \frac{k\lambda}{\beta Cos\theta} \qquad (7.1)$$

Where D is the crystallite size (nm), k is the Scherrer constant (0.9), λ is the x-ray source's wavelength (0.15406 nm), β (radians) is the full width at half maximum and θ is the peak position in radians. It is clear that as the diffraction peaks broaden the crystallite size decreases.

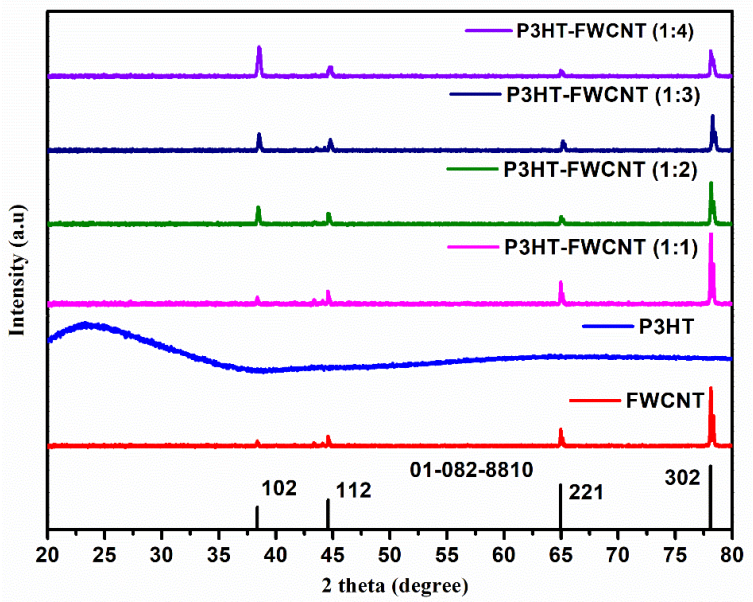

Figure 7. 1: XRD patterns of FWCNT, P3HT, P3HT-FWCNT at different ratios.

7.3.2 UV/VIS/NIR-NIR Analysis

The absorption spectra of the prepared samples were examined at room temperature using a UV/VIS/NIR spectrophotometer in the wavelength range from 250 to 800 nm. Fig. 7.2 (a) shows normalized absorption spectra of P3HT and P3HT-FWCNT at different ratios. P3HT-FWCNT shows better absorption performance at different ratios. The results shows that P3HT-FWCNT (1:1) has the highest absorption compared to other composites. This should improve the electrical conductivity and could lead to a higher efficiency of the photovoltaic solar cell. The spectra show that the samples have peaks at different positions (~530 and ~636 nm) and these positions are assigned to the π-π*transitions of P3HT [26]. The optical bandgap was extrapolated from the linear portion of the Tauc's plot [27]:

$$\alpha hv = A(hv\text{-}Eg)1/2 \qquad (1)$$

Where A is the constant, hv is the photon energy (h=Plank's constant and v is frequency of a photon) and a is the absorption coefficient. The estimated optical bandgap was obtained by extrapolating from the linear portion of the Tauc's plot as shown in Fig. 7.2 (b) with P3HT having 1.8 eV. The estimated bandgap for P3HT-FWCNT at different ratios (1:1 to 1:4) was found to be ~2.7 eV and ~1.8-1.9 eV for

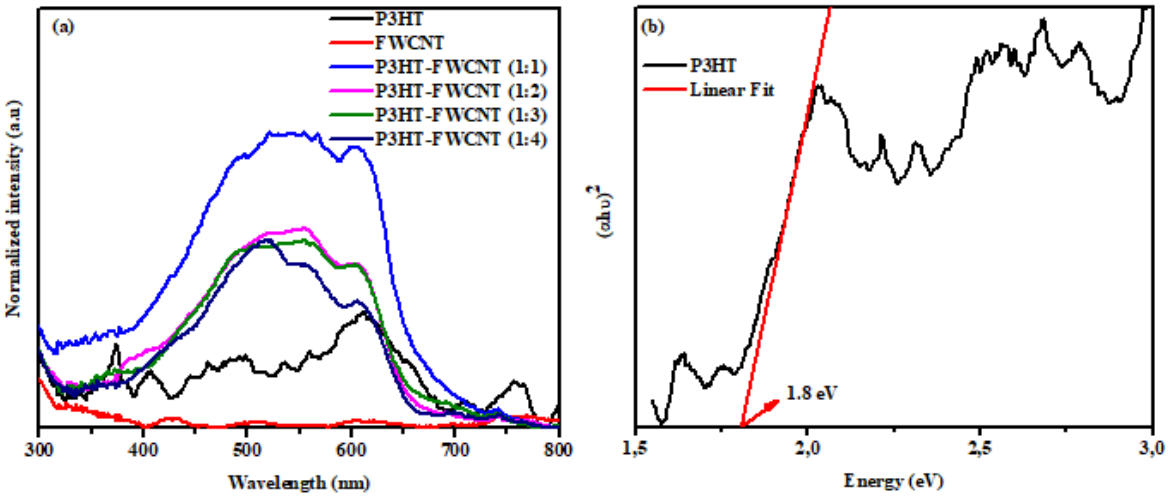

Figure 7. 2: Normalized absorption spectra of (a) FWCNT, P3HT and P3HT-FWCNT at different ratios (b) P3HT Tauc's plot.

7.3.3 Photoluminescence Analysis

The PL measurements shown in Fig. 7.3 were performed to observe the charge transfer between the donor-acceptor pair. The emission spectra were compared to P3HT. The PL results clearly show the PL quenching of the emission spectra, which can be attributed to the presence of FWCNT. This confirms that the charge transfer between P3HT and FWCNT was successful. This quenching is attributed to the position of the P3HT LUMO and FWCNT work functions which are close to each other [28]. Again, this phenomenon can be explained by the strong π-π interaction between the P3HT and FWCNT chains, which photoinduced electrons are efficiently separated and transferred, avoiding exitonic combinations [29,30]. This makes it energetically favourable for the transfer of electrons from P3HT LUMO to FWCNT, suggesting a strong electronic interaction between the P3HT chains and FWCNT. These results correspond to the UV/VIS/NIR results obtained. The peaks at ~636 and ~690 nm are attributed to a purely electronic transition in regioregular P3HT [31]. The results show that P3HT-FWCNT (1:1) further quenches the intensity of PL by showing charge transfer between donor-acceptor materials, thereby reducing electron-hole recombination. This P3HT-FWCNT (1:1) has a strong PL quenching effect resulting in high charge separation in the photoactive layer.

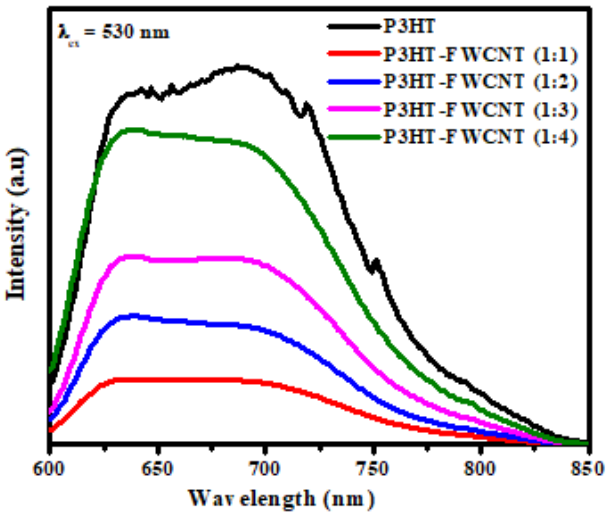

Figure 7. 3: Emission spectra of pristine P3HT, and P3HT-FWCNT at different ratios.

7.3.4 FE-SEM analysis

The FE-SEM pictures in Fig. 7.4 (a) exhibited a smooth surface with no discernible morphology, but the morphology of FWCNT in Fig. 7.4 (b) revealed that the nanotubes were not aligned and were randomly entangled. The nanotubes were extensively intertwined with each other in several regions, and aggregation was observed. This behaviour was explained by the fact that CNT prefer to remain together as bundles due to strong intrinsic van der Waals forces, resulting in limited solubility in many solvents and hence poor dispersion when combined with diverse polymers [32]. Figure 7.4 (c) showed entangled nanotubes with P3HT looping around FWCNT walls. The overall performance of FWCNT is still not as impressive as expected due to some issues like nanotube entanglement, non-alignment, and metallic impurities [33]. According to Danish et al. [33] these problems can lead to a reduction in hole mobility and an increase in recombination pathways. However, this study aims to find a composite that exhibits the strongest PL quenching effect, indicating the largest charge separation potential in the photoactive layer. Before selecting the appropriate composition of the composite used for the photoactive layer, we also studied the properties of PL P3HT and composite film, and therefore, 1:1 should improve the electrical conductivity of P3HT.

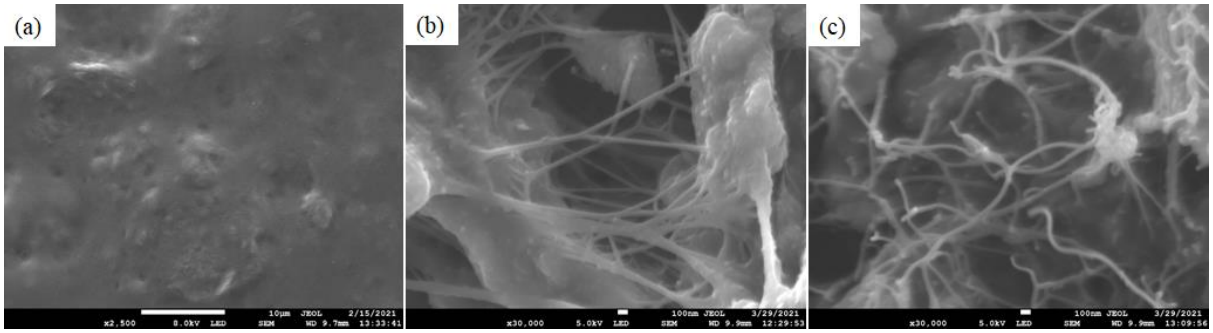

Figure 7. 4: (a) P3HT (b) FWCNT (c) P3HT-FWCNT (1:1).

7.3.5 EDS analysis

The EDS in Fig. 7.5 confirms the presence of carbon (C) from FWCNT. The presence of C, oxygen (O) and sulphur (S) from P3HT and P3HT-FWCNT (1:1). The absence of other peaks corresponding to any impurity confirms the fact that the composite has a single structure and phase as confirmed by the XRD. The homogeneity of this mixture may promote the photon absorption improvement in the organic solar cell devices thereby enhancing the efficiency.

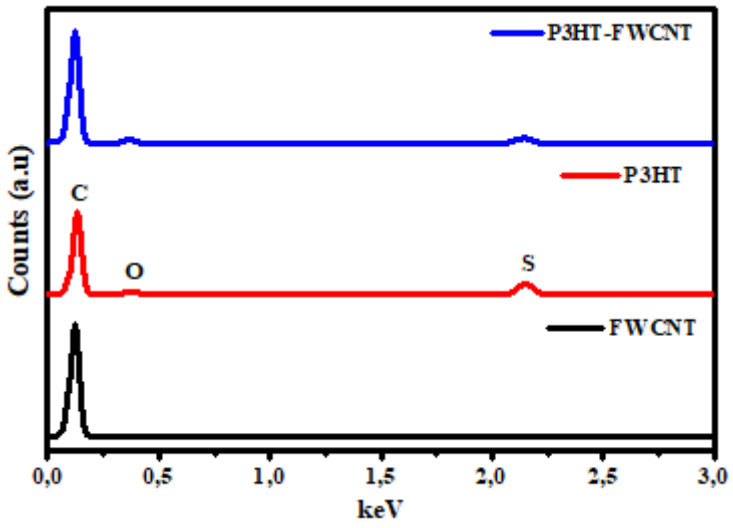

Figure 7. 5: EDS spectra of pristine P3HT, and P3HT-FWCNT at different ratios

7.3.6 Fourier-transform Infrared analysis

To understand the interaction of FWCNT and P3HT, FTIR spectroscopic measurements were performed. The strong absorption band between 2750 and 3300 cm^{-1} was assigned to vibronic C-H stretching as shown in Fig. 7.6. The band at 1380 cm^{-1} is due to the presence of CO_2 in the atmosphere, the bands at 1084 and 1043 cm^{-1} correspond to the asymmetric and symmetric C=O stretching modes. However, the P3HT peaks remain visible and are attributed to the π-π interaction between P3HT-FWCNT. These results correlate with XRD results, where all

samples have a cubic structure with no observed impurities, and PL, where all samples suppress P3HT intensity.

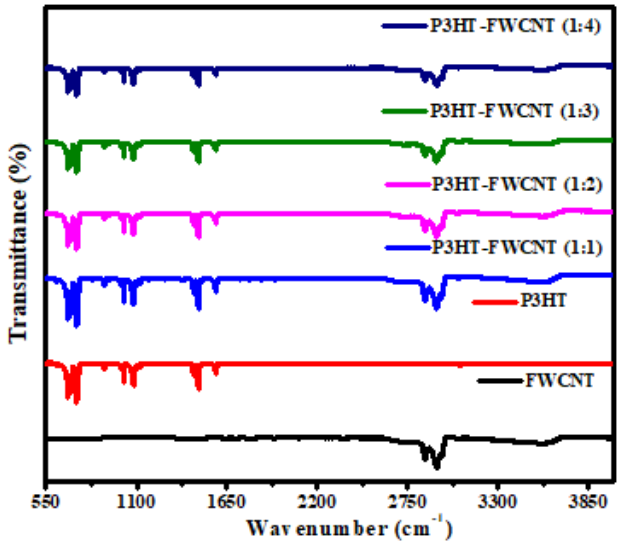

Figure 7. 6: FTIR spectra pristine P3HT, and P3HT-FWCNT at different ratios

7.3.7 Electrical Characterization

The I-V curve in Fig. 7.7 shows the non-linear rectification behaviour for all samples. The rectification is improving when P3HT is incorporated with FWCNT. When the ratio is 1:1 the curve shows that it has the highest conductivity than others due to P3HT wrapping over the FWCNT walls. This is due to the good interaction between the donor-acceptor pair. These results are consistent with UV/VIS/NIR and PL where the 1:1 ratio has the maximum absorbance and in PL further quenches the intensity of PL. These results also show that the production of donor-acceptor pairs is higher in the nanocomposite film than in P3HT. This means that P3HT/FWCNT films are favourable for use in organic solar cells. The conductivity diminishes as the P3HT-FWCNT ratio increases. This is because FWCNT may form insulating barriers inside the composite, preventing charge transfer and lowering electrical conductivity.

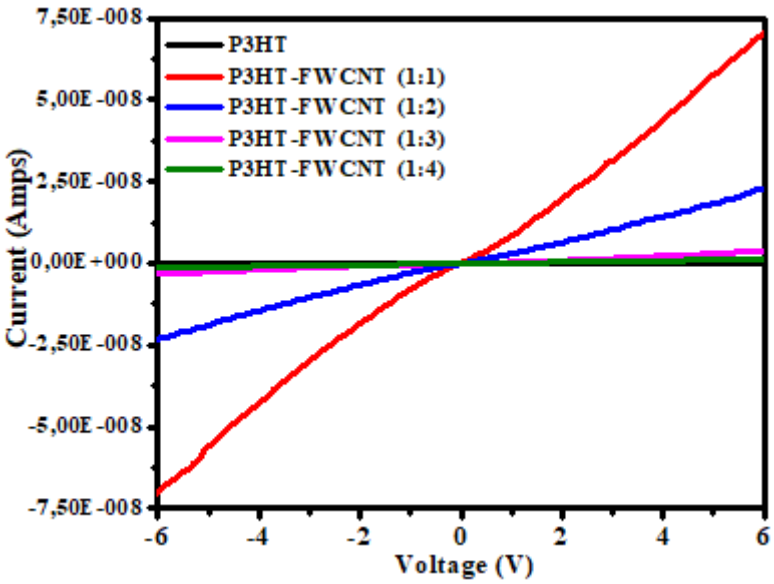

Figure 7. 7: The I-V characteristic spectra pristine P3HT, and P3HT-FWCNT at different ratios.

7.4. Conclusion

In summary, the interactions between FWCNT and P3HT were examined. XRD confirmed the cubic structure and no diffraction peaks other than the FWCNT peaks. UV/VIS/NIR-NIR showed better absorption and provided a better opportunity for higher efficiency of organic solar cells. The PL results showed that all samples quenched the P3HT intensity, offering great opportunities for charge separation in the photoactive layer. FESEM showed disordered FWCNTs, EDS confirmed the composition of the samples. FTIR identified all functional groups and electrical measurements showed that P3HT-FWCNT (1:1) improves conductivity, making this material a prime candidate for significantly accelerating electron transport and reducing electron hole recombination rate and increase efficiency of organic solar cells.

References

[1] E. R. Rwenyagila, *Int. J. Photoenergy*, (2017) 1–12.

[2] N. Grossiord, M. J. R. Kroon, P. W. N. Andriessen, *Blom,* **13** (2012) 432–456.

[3] S. Qu, M. Wang, Chen M. Y, Yao Q, Chen L, *RSC. Adv.* **8** (2018) 33855–33863.

[4] P. L. McEuen, M. S. Fuhrer, H. Park, *IEEE Trans. Nanotechnol*, **1** (2002) 78–85.

[5] Inmuddin, N. Shakeel, M. I. Ahamed, S. Kanchi, H. A. Kashmery, *Nature research,* **10** (2020) 5052.

[6] C. Dekker, *Phys Today,* **52** (1999) 22 – 28.

[7] L. Stavarache, A. Lepadatu, V. S. Teodorescu, M. L. Ciurea, V. Lancu, M. Dragoman, G. Kostantinidis, R. Buiculescu, *Nanoscale Research Letters*, **6** (2011) 88

[8] Y. Feng, H. Zhang, Y. Hou, T. P. McNicholas, D. Yuan, S. Yang, L. Ding, W. Feng, J. Liu, *ASC Nano*, **2** (2008) 1634–1638

[9] M. Ma, Z. Miao, D. Zhang, X. Du, Y Zhang, Zhang C, Lin J, Chen Q, *Biosensors and Bioelectronics*, **64** (2015) 477–484.

[10] J. Jung, E. H. Suh, Y. J. Jeong, H. S. Yang, T. Lee, J. Jang, *ASC Applied Materials & Interface,* (2019) S1–S14.

[11] T. S. T. Khanh, N. P. H. Nam, N. N. Dinh, *J. Mater. Sci: Chem. Eng*, **8** (2020) 1-10)

[12] M. Zhang, S. Hofle, J. Czolk, Mertens A, Colsmann A, *Nanoscale*, **7** (2015) 20009 – 20014.

[13] D. Luo, Q. B. Chen, B. Liu, Y. Qui, *Polymers,* **11** (2019) 384.

[14] G. Li, R. Zhu, Y. Yang, *Nature Photonics,* **6** (2012) 153 – 161.

[15] Y. Y. Gao, Z. Wang, G. T. Yue, X. Yu, X. S. Liu, G. Yang, F. R. Tan, Z. X. Wei, W. F. Zhang, *Solar RRL,* **3** (2019) 1900012.

[16] Z. J. Zhang, J. H. Miao, Z. C. Ding, B. Kan, B. J. Lin, X. J Wan, W. Ma, Y. S. Chen, X. J. Long, C. D. Dou, J. D. Zhang, J. Liu, L. X. Wang, *Nat. Commun.***10** (2019) 3271.

[17] S. Ren, L.Y. Chang, S. K. Lim, J. Zhao, M. Smith, N. Zhao, V. Bulovic, M. Bawendi, S. Gradecak, *Nano Letters*, **11** (2011) 3998–4002.

[18] J. A. Haucha, P. Schilinskya, S. A. Choulisa, R. Childersb, M. Bielea, C. J. Brabec, *Sol. Energy Mater. Sol. Cells,* **92** (2008) 727 – 731

[19] N. D Treat. et al., *Adv. Energy Mater.* **1** (2011) 82 – 89.

[20] C. Liu, Z. C. Holman, U. R. Kortshagen, *Nano Lett.* (2009) 3 – 6.

[21] L. E. Greene, M. Law, B. D. Yuhas, P. Yang, *J. Phys. Chem. C Lett.* (2007) 18.

[22] D. Chen, A. Nakahara, D. Wei, D. Nordlund, T. P. Russell, *Nano Lett.* (2011) 561 – 567.

[23] D. Dennler, M. C. Scharber, C. J. Brabec, *Adv mater,* **21** (2009) 1323 – 1338.

[24] M. Ahmad, M. Foroughi, M. R. Monish, *WJNSE.* **2** (2012) 154 – 160.

[25] B.D. Cullity, Elements of X-ray Diffraction (2nd Ed), Addison Wesley, 1956.

[26] T. Huiling, L. Xian, J. Yadong, X. Guangzhong, D. Xiaosong, *Sensors.* **15** (2015) 2086 – 2103.

[27] H. Oh, J. Krantz, I. Litzov, T. Stubhan, L. Pinna, C. J. Brabec, *Sol Energy Mater Sol Cells,* **95** (2011) 2194 – 2199.

[28] J. M. Lee, J. S. Park, S. H. Lee, H. Kim, S. Yoo, S. O. Kim, *Advanced Materials*, **23** (2011) 629 – 633.

[29] F. Y. Cheng, P. Imin, C. Maunders, G. Botton, A. Adronov, *Macromolecules,* **41** (2008) 2304 – 2308.

[30] H. D. Jin, F. Zheng, W. L. Xu, W. H. Yuan, M. Q. Zhu, X. T. Hao, *J.Phys. D: Appl. Phys* (2014) 505502.

[31] R. Al-Gaashani, S. Radiman, A. R. Daud, N. Tabet, Y. Al-Douri, *Ceram. Int.,* **39** (2013) 2283 – 2292.

[32] N. M. Nurazzi, N. Abdullah, S. Z. N. Demon, N. A. Halim, I. S. Mohamad. *Polymers (Basel).* **12** (2021) 1916.

[33] K. Danish, A. Zahid, A. Danyal, K. P. Manoj, K. Idris, *Ain Shams Eng. J,* **12** (2021) 897 – 900.

Chapter 8

Summary, conclusion and future work.

This chapter provides an overview of the study, its conclusion, and recommendations for further research.

8.1. Summary

This study shows how to manufacture rare earth ions doped ZnO and FWCNTs utilizing a microwave-assisted sol-gel technique. The goal is to increase P3HT absorption and electrical conductivity for application in organic solar cells. The prepared samples were characterized using different techniques such as X-ray diffraction (XRD), field scanning electron microscopy (FE-SEM) combined with energy dispersive (EDS) spectroscopy, UV/VIS/NIR-NIR absorption spectrometer and photoluminescence (PL) spectroscopy, X-ray photoelectron spectroscopy (XPS), Fourier transform infrared spectroscopy (FTIR) and current-voltage.

ZnO nanorods doped with Sm^{3+} and Yb^{3+} were successfully synthesized by microwave-assisted sol-gel using 1-thioglycerol as a capping agent to control particles and inhibit their agglomeration. Nanorods have been successfully integrated into P3HT. Charge transfer between the donor and acceptor material was observed from the PL spectra. PL peaks were observed at ~636 and ~690 nm, corresponding to pure electronic transition to pure P3HT.

The optical properties of FWCNT-doped ZnO were observed by UV/VIS/NIR-NIR. A blue shift was observed with increasing FWCNT concentration. The estimated band gap of FWCNT-doped ZnO extrapolated from the linear part of the Tau'c plot showed a blue shift. The incorporation of P3HT into the ZnO-enhanced P3HT spectra indicates a possible improvement of inorganic solar cells. The observed absorption peaks correspond to the P3HT peaks.

An interaction between FWCNT and P3HT was observed. I-V spectra showed improved nonlinear rectification when P3HT was integrated with FWCNT. The spectra showed a good interaction between the donor-acceptor pair. These results were also confirmed by PL, where

P3HT: FWCNT (1:1) quenches the PL intensity, this process is known to reduce charge recombination and increases the efficiency of organic solar cells.

8.2. Future work

Organic solar cells have been studied for the past decades and have shown a strong potential as the next generation of solar cells technology with the efficiency of more than 18%. OSCs have shown a lot of progress in material design and device fabrication with the aim of reducing the energy loss caused by charge recombination. The most challenge in OSCs is the energy loss. Nanorods are known to reduce the charge recombination. This gives us research opportunity for the future work to synthesize nanorods using other synthesis methods. To dope ZnO with different lanthanides ions for up-converting NIR light to visible light by using Yb^{3+} as the sensitizer and to incorporate the low band gap conjugated polymers to improve the efficiency of the OSCs. ZnO is known to be one of potential materials in solar cells due its relatively high conductivity amongst others and improving the OSCs absorption efficiency.

As far as the current study is concern and for prospects, it is recommended that the following aspects are investigated:

- Aligned ZnO nanorods by hydrothermal method.
- Co-dope Er^{3+}, Ho^{3+}, and Tm^{3+} with Yb^{3+}
- Incorporate P3HT
- Fabrication of the OPV device.

List of publications

1. **AS Tebele**, SV Motloung and FB Dejene, Luminescence properties of violet-orange-red emitting $SrCO_3$:1% $Eu^{2+,}$ x% Cr^{3+} phosphors prepared by sol-gel technique, ***proceedings of the South African Institute of Physics 2013***.

2. **AS Tebele**, SV Motloung and FB Dejene, Effects of catalyst:Ba molar ratio on the structure and luminescence properties of $BaCO_3$:1% Eu^{3+}, 2% Dy^{3+} phosphors synthesized using sol-gel process, ***proceedings of the South African Institute of Physics 2014, ISBN: 978-0-620-65391-6.***

3. Luyanda L. Noto, Sefako J. Mofokeng, Fokotsa V. Molefe, Hendrik C. Swart, **Angelina S. Tebele**, Mokhotjwa S. Dhlamini. **Book:** Spectroscopy of Lanthanide-doped oxide materials, **Chapter**: Luminescent dynamics of rare earth doped CaTiO3 phosphors, ***Woodhead publishing. DOI:10.1016/B978-0-08-102935-0.00003-4***.

4. **Qotso A.S**, Mbule P.S, Mothudi B.M, Characterization of P3HT-CNT thin film for photovoltaic solar cell applications, ***proceedings of the South African Institute of Physics Conference 2021, pp 31 – 36, ISBN: 978-0-620-97693-0.***

5. **Seithati Qotso**, Pontsho Mbule, Bakang Mothudi, Microwave-assisted sol-gel synthesis of P3HT-ZnO: Sm^{3+}, Yb^{3+}: Study of structure, morphology, optical and electrical conductivity for organic solar cells application, ***Mater. Chem. Phys., 294 (2023) 127023.***

6. **Seithati Qotso**, Pontsho Mbule, Bakang Mothudi, Effect of ZnO nanorods singly doped with Er^{3+}, Ho^{3+}, and Tm^{3+} on P3HT for organic solar cell application. ***Due for submission.***

7. **Seithati Qotso**, Pontsho Mbule, Bakang Mothudi, Synthesis and characterization of P3HT-ZnO-FWCNT for possible application in organic solar cells. ***Physica B: Condensed Matter, 671 (2023) 415407.***

Research presentations

1. 58th annual conference of the South African Institute of Physics (SAIP), 08 – 12 July 2013, University of Zululand, Richards Bay, South Africa.

   Luminescence properties of violet-orange-red emitting $SrCO_3$:1% Eu^{2+}, x% Cr^{3+} phosphors prepared by sol-gel technique
   AS Tebele, SV Motloung and FB Dejene

2. 59th annual conference of the South African Institute of Physics (SAIP), 7 – 11 July 2014, University of Johannesburg, Johannesburg, South Africa.

   Effects of catalyst:Ba molar ratio on the structure and luminescence properties of $BaCO_3$:1% Eu^{3+}, 2% Dy^{3+} phosphors synthesized using sol-gel process.
   A. S. Tebele, S. V. Motloung and F. B. Dejene

3. 2018 International Conference on Surfaces, Coatings and Nanostructured Materials, 19 – 23 November 2018.

   Structural and optical properties of ZnO thin films synthesized by sol gel spin coater method.
   Seithati Tebele, Pontsho Mbule and Bakang Mothudi

4. 8th South African conference on photonic materials, 6 – 10 May 2019, Kariega Game Reserve, South Africa.

   Characterization of P3HT-ZnO:RE ions synthesized by microwave method.
   Seithati Qotso, Pontsho Mbule and Bakang Mothudi

5. 65th annual conference of the South African Institute of Physics (SAIP) (virtual conference), 22 – 30 July 2021, North-West University, South Africa.

Characterization of P3HT-CNT thin film for photovoltaic solar cell applications
Seithati Qotso, Pontsho Mbule and Bakang Mothudi.

6. 9th South African conference on photonic materials, 8 – 12 May 2023, Kruger National Park, South Africa.

   Synthesis and characterization of P3HT:ZnO-FWCNTs for possible application in organic solar cells.
   Seithati Qotso, **Pontsho Mbule** and Bakang Mothudi.